Osaka University

Doctoral Thesis

The monomer-dimer models in two and three dimensions: Tensor renormalization group study

Author:
Takahiro Otsuka

Supervisor:
Professor Makoto Kikuchi

Interdisciplinary Computational Physics Group
Department of Physics

February 21, 2022

Abstract

The monomer-dimer models in two and three dimensions: Tensor renormalization group study

by Takahiro Otsuka

The dimer problem is a problem of counting the number of ways to arrange diatomic molecules (dimers) on a plane, when overlapping dimers is prohibited. The dimer problem can be defined on the lattice as a pure dimer model (PDM), and analytical solutions are known for the two-dimensional model. PDM is one of the simplest model and is therefore widely studied because it is associated with a variety of physics. For example, PDM shows critical phenomena on bipartite lattices such as square and honeycomb lattices, and there is a one-to-one correspondence between the PDM and the Ising model. PDM can be extended to the monomer-dimer model (MDM), which contains not only diatomic molecules but also monoatomic molecule (monomers). Unlike PDM, there is no analytical solution in MDM even if it is two-dimensional. Therefore, it is efficient to perform numerical calculations to analyze the properties of MDM or high-dimensional PDM or MDM.

In this thesis, we study the critical behavior of MDM on 2D and 3D lattices using DMRG and Higher Order Tensor Renormalization Group (HOTRG), which is one of the tensor network calculations based on the singular value decomposition. Criticality is reflected in physical quantities such as entropy and monomer density as a deviation from the power. By analyzing this behavior, we clarify the criticality of MDM and classify MDM by determining the critical exponent. Simultaneously through the applying HOTRG to a several systems, we optimize the algorithm for high-dimensional systems and study the spectrum of HOTRG.

First, we study the critical behavior of 2D MDM using DMRG and HOTRG. Although there may be a correspondence between MDM and the Ising model with magnetic field, it has not been discussed in terms of the universality class. Therefore, by determining the critical behavior appearing in the monomer density and its critical exponent, we show that the universality class of MDM and Ising model are different.

Next, we investigate the critical behavior of 3D MDM. We analyze two main models: the finite layer model and the infinite system. For finite layer bipartite models with a small number of layers, DMRG is used to show that the two-layer model is non-critical and the three-layer model is critical. For the 3D infinite system, we first optimize the 3D HOTRG to reduce the memory cost by changing the order of tensor contractions and introducing an algorithm to assign the tensor components to different cores (we call parallel computation method). Using these algorithms of HOTRG, we calculate the residual entropy of PDM and analyze the critical behavior of MDM. The accuracy of the residual entropy values is higher than previous TN calculations, but our calculation is not accurate enough to determine the critical exponents.

Finally, we analyze the asymptotic behavior of the spectrum (singular values) of HOTRG based on the Baxter's CTM picture. Comparing the asymptotic behavior of spectrum of HOTRG and that of DMRG, we derived the relation that holds for the integrable models.

Acknowledgements

First of all, I would like to express my sincere gratitude to my supervisor, Professor Makoto Kikuchi, for his generous support of my Ph.D. course and his insightful advice on my research. I am deeply grateful to Professor Yasuhiro Akutsu for his enthusiastic guidance in both my research and life throughout my Ph.D. course.

The members in Cybermedia center in Osaka University have been supported my researching throughout my Ph.D. course. I would like to thank Professor Hajime Yoshino for fruitful discussions. I also thank all my colleagues in Cybermedia center in Osaka University for their friendships and fruitful communications.

Finally, I would like to express my deep gratitude to my family for their continuous support during my whole life. Without their encouragement, I could not have completed my Ph.D. course.

This work is supported by "Joint Usage/Research Center for Interdisciplinary Large-scale Information Infrastructures" in Japan (Project ID: EX21703) and was achieved through the use of OCTOPUS and SQUID at the Cybermedia Center, Osaka University.

Contents

Chapter 1

Introduction

1.1 Critical phenomena in Statistical physics

The physical phenomena around us are physics on a large scale, appearing as a group of microscopic freedoms at the atomic level. Statistical physics is the study of physics on such a large scale. Phase transition and critical phenomena have been studied as a main topic of statistical physics for a long time. The study of critical phenomena allows us not only to analyze the properties of matter, but also to classify physical phenomena on a large scale by the concept of "universality". Universality means that physics on a large scale does not depend on the details of matter. This property of universality allows us to understand the nature of critical phenomena in matter by constructing a simple model. The monomer-dimer system that we focus on in our thesis is one of the simplest models, and this simplicity expands the range of applications through the concept of universality. Due to the universality, the critical phenomena can be quantitatively characterized by critical exponents. Therefore, the critical group to which a model belongs is classified by the value of the critical exponent, and calculating the critical exponent of a material or model is an important goal of statistical physics. For this purpose, various computational methods such as exact solutions, effective theory, Monte Carlo simulations, and tensor renormalization groups have been developed to calculate the critical exponents. In this section, we will review the basic concepts of critical phenomena and statistical physics[1].

We introduce the Ising model, which is the simplest model that describes magnetic materials. Hamiltonian of the Ising model is given as

$$H = -J \sum_{\langle i,j \rangle} S_i S_j - h \sum_{i=1}^{N} S_i, \tag{1.1}$$

where S_i represents a spin at lattice site i and takes ± 1 depending on the spin direction. J is the interaction between adjacent spins, and h is the position-independent magnetic field. The Ising models represent the ferromagnetism at $J > 0$ and antiferromagnetism at $J < 0$. Here, we assume $J > 0$.

In magnetic materials, the system is characterized by the magnetization defined as

$$m = \frac{1}{N} \sum_{i=1}^{N} \langle S_i \rangle \,, \tag{1.2}$$

which represents how well the spins are aligned. The magnetization is a conjugate thermodynamic quantity of the magnetic field h:

$$m = -\frac{\partial f}{\partial h}, \tag{1.3}$$

where f is the free energy of the system. The magnetic susceptibility is defined as

$$\chi = \frac{\partial m}{\partial h} = -\frac{\partial^2 f}{\partial h^2}. \tag{1.4}$$

Materials, including the magnetic materials introduced above, take various states depending on the surrounding environment. A phase is defined as a state in which the macroscopic properties of a material are uniform. In the case of magnetic materials, depending on the temperature T and magnetic field h, there is a paramagnetic phase where $m = 0$ and a ferromagnetic phase where m is a finite value. The discontinuous of m from zero to a finite value is called a phase transition, and the condition where the phase transition occurs is called a transition point. The phase transition appears as a singularity in the free energy and are classified according to the type of specificity. If the first-order derivative is discontinuous at the transition point, this phase transition is called a first-order phase transition. On the other hand, if the second-order derivative or higher is discontinuous at the transition point, this phase transition is called a continuous phase transition. The point where the continuous transition occurs is called a critical point.

The state of the system and the position of the phase transition are represented as a phase diagram in the parameter space of temperature and magnetic field. The phase diagram of the Ising model in (T, h) space is shown in Fig.1.1. We also show the behavior of the magnetization when he parameters are moved along two different lines on the phase diagram. For $T < T_c$, when h is changed from negative to positive, the

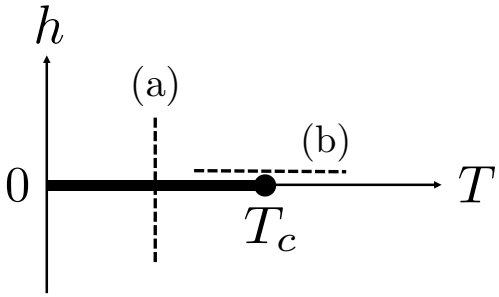

FIGURE 1.1: Phase diagram of the Ising model. The bold line represents the first-order phase transition line and the round symbol represents the critical point.

sign of m changes discontinuously, which is the first-order phase transition (Fig.1.2 (a)). The remaining finite magnetization in the limit of $|h| \to 0$ is called spontaneous magnetization. On the other hand, when T is reduced to T_c with h fixed near 0, a continuous transition appears in which m changes continuously from 0 to positive values (Fig.1.2 (b)).

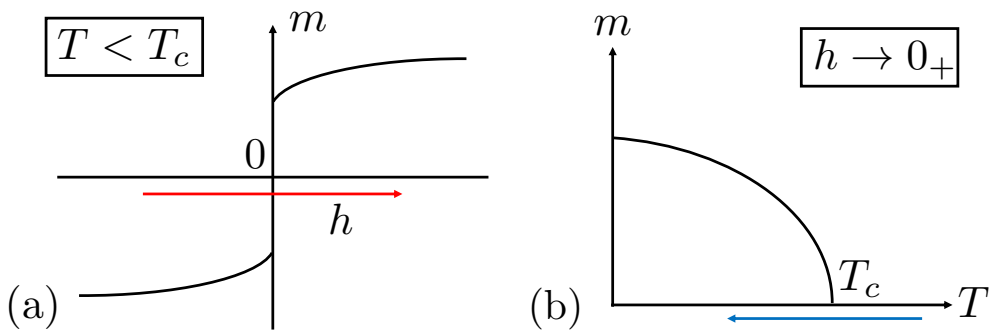

FIGURE 1.2: (a) First-order transition of the magnetization to magnetic field at $T < T_c$. (b) Continuous transition of magnetization versus temperature in the vicinity of $h = 0$.

Finally, we describe the critical behavior, which is the main theme of this thesis. With approaching the critical point, some physical quantities diverge. Phase transitions are characterized by this critical behavior, and the critical behavior is quantitatively characterized by the critical exponent, which expresses the degree of divergence. We define the critical exponents in the case of magnetic materials below.

- Magnetic susceptibility

$$\chi \propto |t|^{-\gamma} \ (T \neq T_c) \text{ where } t = \frac{T - T_c}{T}, \tag{1.5}$$

- Specific heat

$$C \propto |t|^{-\alpha} \ (T \neq T_c), \tag{1.6}$$

- Magnetization

$$m \propto |t|^{-\beta} \ (T < T_c), \tag{1.7}$$
$$m \propto |h|^{\frac{1}{\delta}} \ (T = T_c), \tag{1.8}$$

- Correlation function of the spin : $G(r) = \langle S_i S_{i+r} \rangle_c$

$$G(r) \propto r^{-\tau} e^{-\frac{r}{\xi}} \ (T \neq T_c), \tag{1.9}$$
$$\xi \propto |t|^{-\nu} \ (T \neq T_c), \tag{1.10}$$
$$G(r) \propto r^{-d+2-\eta} \ (T = T_c). \tag{1.11}$$

The power behavior of the correlation function at the critical point (1.11) is due to the divergence of the correlation length.

For example of the 2D Ising model, the critical exponents are determined by using exact solution derived by Onsager[2] (Tab.1.1).

TABLE 1.1: Critical exponents of two-dimensional ising model.

Critical exponents	values
α	0
β	$\frac{1}{8}$
γ	$\frac{7}{4}$
δ	15
ν	1
η	$\frac{1}{4}$

1.2 Monomer-dimer problem

The dimer problem is a problem of counting the number of ways to arrange diatomic molecules (dimers) on a plane, when overlapping dimers is prohibited. The dimer problem can be defined on a lattice as a pure dimer model (PDM). In the PDM (Fig.1.3 (a)), the diatomic molecule occupies a pair of adjacent lattice sites. The history of PDM goes back at least to Robert's experimental consideration of it in 1935[3]. Robert's experiment considers the adsorption of an oxygen molecule onto a tungsten surface and estimates how the molecule finds and adsorbs an unoccupied tungsten atom. To tackle dimer problem, Robert uses Monte-Carlo methods[3–5] and Bethe approximation[6]. After such an efforts, the analytical solution for PDM on a square lattice was derived by Kasteleyn, Temperley and Fisher by the Pfaffian method (this is discussed in Sec.2.2)[7–9]. PDM solutions correspond to the graph-theoretic concept of "matching," and analytical solutions to PDM are also important in the field of mathematics.

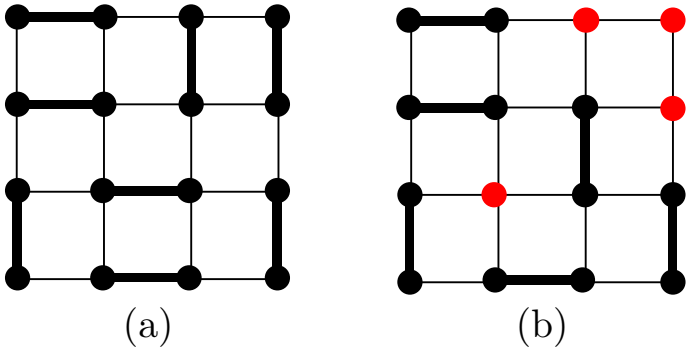

FIGURE 1.3: (a) Pure dimer model. (b) Monomer-dimer model.

The dimer model can be extended to a monomer-dimer problem which contains not only diatomic molecules but also monoatomic molecule (monomers). This problem is defined as a monomer-dimer model (MDM) on the lattice as shown in Fig.1.3 (b). MDM is introduced by Fowler and Rushbrooke in 1947[10]. However, an analytical solution of MDM in general case has not been discovered except for the limited circumstances where a single monomer was included[11, 12]. Therefore, to study the properties of MDM generally, we should use the approximation methods or the numerical calculations. At the time this model was introduced, MDM was studied by various approximation method, such as Bethe approximation[13–16] and the transfer matrix method[17] as PDM.

As discussed above, the dimer model (containing MDM) has a long history. Although the history of the dimer model is old, it is still being studied today from various aspects because of its simplicity. For example, in the context of liquid crystals (LCs), the dimer model is important. LC is an intermediate phase of the material between an isotropic liquid and a crystalline solid, where the molecules have an orientation order but no perfect positional order. One candidate for the shape of a molecule with LC phase is a rod-shaped molecule (Fig.1.4).

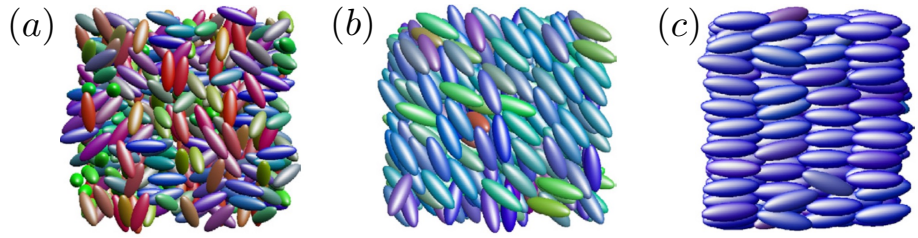

FIGURE 1.4: LC phase of the rod-shaped molecules[18]. (a) Isotropic phase. (b) Nematic LC phase. It is characterized by a long-range orientation order but no long-range translational order. (c) Smetic LC phase. It has both long range translational order and long range orientational order.

The lattice model, in which rod-shaped molecules of arbitrary length k are arranged without allowing overlap, was introduced as the rod model[19] as shown in Fig.1.5. Even the model of hard-core interaction has been shown to have an LC phase when the rod length is longer than a certain length[20, 21]. Dimer model is an example of rod models, corresponding to $k = 2$. As for the dimer model, it can be LC by including an interaction that aligns the orientation[22].

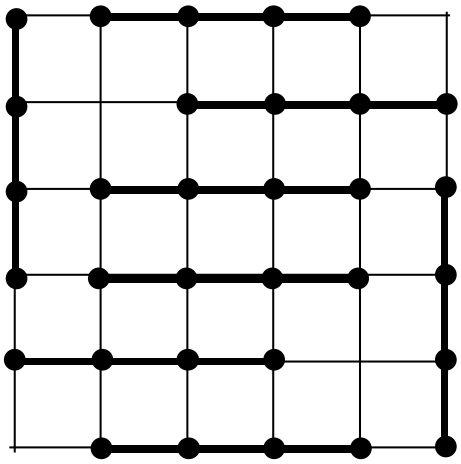

FIGURE 1.5: Example of a rod model with a finite density of vacancies ($k = 4$).

While the study of LC is progressing, there are still some unanswered questions about fundamental aspects of the dimer model. We indicate some important topics of the dimer model as follows.

Residual entropy

Residual entropy is defined as a finite entropy at $T = 0$. According to the third law of thermodynamics advocated by Nernst, the entropy at $T = 0$ is zero. However,

there are also systems that have residual entropy due to a macroscopically degenerate ground state and violate the third law. An famous example of the system with residual entropy is the frustrated one such as anti-ferromagnetic model on the triangular lattice shown as Fig.1.6. In this frustrated system, the orientation of the third spin must be down to minimize the energy with the first spin, but up to minimize the energy with the second spin[23]. According to the definition of frustrated systems, the state that minimizes the energy of the entire system is not uniquely determined. Therefore, frustrated systems are in a macroscopically degenerate ground state and consequently have residual entropy.

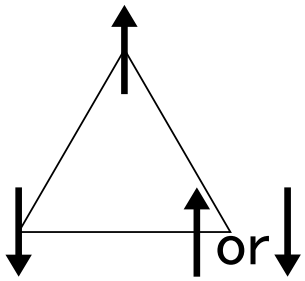

FIGURE 1.6: Anti-ferromagnetic model on the triangular lattice as example of frustrated system. If we determine the orientation of the spins at the two vertices of the triangle at first, the orientation of the remaining spin can not be determined uniquely.

In the pure dimer model, temperature is not defined, but it has a degenerate ground state, and in the ground state it has a finite entropy. Therefore, we can say that the PDM has a so-called residual entropy. In the two-dimensional PDM, residual entropy is calculated by using the analytical solution. However, since no analytical solution is known for high-dimensional systems, it is important to calculate the residual entropy of such systems by numerical simulations.

Criticality

For some lattices, such as square and honeycomb lattices, PDM is critical[24, 25]. PDM is a special case of MDM, and its no-monomer point corresponds to a critical point in terms of the monomer-dimer framework. On the other hand, there are non-critical model, such as triangular and kagome lattices, where the correlators decay exponentially[26–29]. Only in the two-dimensional case, the criticality of the PDM on a given lattice has been determined analytically or numerically. In higher dimensions, it is difficult to investigate critical properties by such a direct approach, and research to clarify critical properties is needed.

Correspondence with Ising model

The PDM and MDM can be related to various models. The most important example is Ising model with zero magnetic field, which has a one-to-one correspondence with the PDM[24, 26, 30]. This correspondence can be explained by mapping the diagram of high temperature expansion in Ising model onto the dimer configuration on the deformed lattice. In 1971, Heilmann and Lieb suggest that this method can be extended to Isimg model with non-zero magnetic fields and has a one-to-one correspondence with MDM[31]. However, it has not been discussed whether the Ising model with magnetic field and MDM belong to the same universality class.

Central charge of conformal field theory

The scaling limit of the critical system is described by a conformal field theory (CFT). The universality class is characterized by the value of the central charge c defined by CFT. Dimer model has also been studied in terms of CFT, but there has been confusions whether the dimer model has the value of $c = 1$ or $c = -2$. This confusion can be attributed to the fact that the distinction between PDM and MDM is not clearly separated[32].

The central charge is related to the finite-size corrections to the critical free energy. The detailed study of the finite-size corrections was started with Ref.[33] for PDM, and subsequent studies have been done for various geometries and boundary conditions[34–39]. These studies suggest that PDM has $c = -2$. Additionally, the Abelian sandpie model that is equivalent to PDM is classified as $c = -2$[40–44]. On the other hand, the central charge of MDM is determined as $c = 1$ by calculating the correlation function of monomers on the boundary[45]. According to the above result, the central charge is considered to be $c = -2$ for PDM and $c = 1$ for MDM. However, the equivalent Gaussian field theory to PDM or MDM is $c = 1$[46], and there is still a question as to which framework Gaussian field theory should be classified as, PDM or MDM.

1.3 Tensor renormalization group

Tensor Networks (TNs) is a framework for representing partition functions as contractions of tensors corresponding to local weights. TN has been applied not only to statistical mechanics, but also to various other physics such as quantum information and quantum gravity. So, TNs are being studied vigorously and developed rapidly, both in terms of theory and practical computation. Tensor renormalization group (TRG), which we mainly study and use in this thesis, are also included in the category of TNs simulations. Precise analysis of high-dimensional systems, such as 3D classical systems and 2D quantum systems, has long been a major goal in the field of statistics. However, DMRG, one of the prototypes of TNs, was not effective for high-dimensional systems, but TNs simulation and TRG are considered to be effective computational tools for high-dimensional systems. In order to establish this method, it is necessary to study the practical application of TN and TRG and their fundamental aspects.

The essence of TNs is to extract the essential effective degrees of freedom from the huge number of degrees of freedom in a many-body system. A powerful tool for extracting important degrees of freedom is a technique called singular value decomposition (SVD), which is used to extract the important basis of a state. In 1992, White developed the density matrix renormalization group (DMRG) as an algorithm that combines SVD and real space RG.[47, 48]. The origin of the term RG lies in the restriction of degrees of freedom, but DMRG differs from RG strictly in that it does not redefine the length scale in the iterative process. DMRG corresponds to the variational method for MPS (Matrix Product State)[49], where MPS is a one-dimensional TN that gives an accurate approximation of the state. Therefore, DMRG is a strong method for 1D quantum systems and 2D classical systems, but is difficult to extend to higher dimensional systems. After DMRG, projected entangled pair state (PEPS) was established as a higher dimensional analysis[50–53]. PEPS is a variational method based on the tensor product state (TPS), where TPS is a high-dimensional extension of MPS. Recently, several optimization algorithms in PEPS have been widely used for the analysis of 2D quantum and 3D classical systems. On the other hand, the RG based algorithm has been developed, such as multi-scale renormalization ansatz[54,

55] and tensor renormalization group (TRG)[56]. In addition, a TRG-based method combined with higher-order SVD (HOSVD), called HOTRG, was developed[57]. It is not easy to generalize conventional TRG to higher dimensions because the shape of lattice is changed under the renormalization process. However, since HOSVD does not change the shape of the lattice during the renormalization process, it can be applied to higher dimensions, and HOTRG has attracted a great deal of interest in the field of lattice gauge theory[58, 59]. The accuracy of HOTRG has been improved over traditional RG-based methods. Actually, the transition temperature of 3D Ising model calculated by HOTRG is comparable with recent Monte Carlo simulations[60].

HOTRG is expected to be established as a next generation method applicable to higher dimensions because of its simple algorithm and the absence of sign problems that appear in quantum Monte Carlo simulations. Since HOTRG is a relatively new method and there are few examples of its application, the range of systems to which it can be applied is not known. In addition, HOTRG has a large memory cost, which makes it difficult to use for high-precision calculations. Therefore, we show the analysis of dimer problem as a practical application examples and develop the new algorithm to lower the memory cost in this thesis.

1.4 Purpose of this Thesis and Outline of this thesis

In Sec.1.2 and 1.3, we showed the issues of the monomer-dimer problem and TRG from various aspects. In this section, after referring to previous studies using the Monte Carlo calculations (MC), we will mention what kind of problem we will deal with and how we will approach it in this thesis.

In the society of the MC calculation, various correlation function based studies have been conducted. For models with only hard-core interactions, correlation functions have been calculated for PDM and MDM in 2D[28] and PDM in 3D[61] to determine whether their behavior is exponential decay or power law. On the other hand, models with an interaction aligning the orientation have also been vigorously studied for 2D[62], two-layer models[63], and 3D[64–66]. In contrast to the many studies of finite temperature phase diagrams, there are few studies based on the calculation of entropy at finite monomer density. This is probably because it is difficult (not impossible) to set up hard-core conditions and entropy calculations are not strong point in MC calculations. Therefore, we will apply DMRG and HOTRG, which can directly calculate the entropy at infinite system size, to the dimer model and pursue the following properties.

- Critical behavior of two-dimensional MDM
  MDM has a critical point at the no-monomer point depending on the lattice geometry. However, there are few studies that discuss how the criticality is reflected in the thermal quantity at the vicinity of the no-monomer point. Therefore, we carry out numerical calculations in the region of finite monomers, where no analytical solution exists, to analyze the critical behavior of entropy and monomer density, and to determine the critical exponent of monomer density.

- Correspondence between MDM and the Ising model with a magnetic field
  Heilmann and Lieb suggest that the Ising model with non-zero magnetic fields has a one-to-one correspondence with MDM in two-dimensions[31]. But they do not mention the relationship of criticality property between them. Based on the results of our analysis of the critical behavior of the MDM, we show that the MDM belongs to a different universality class from the Ising model.

- Comparing the accuracy of HOTRG with that of DMRG in 2D calculation
  We analyze the critical behavior of two-dimensional MDM by using both HOTRG and DMRG, keeping the extension of HOTRG to three-dimensions in mind. By comparing HOTRG with DMRG, a well-established two-dimensional analysis method, the critical behavior of MDM and its applicability to high-dimensional analysis will be pursued.

- Development of an optimal algorithm to lower the memory cost of HOTRG
  HOTRG is an algorithm that can be easily extended to higher dimensions, but it incurs a large memory cost for high-precision calculations. To avoid the upper limit of computer memory, we developed the HOTRG algorithm to reduce the memory cost by focusing on the order of tensor contraction and the parallelization of tensor components.

- Residual entropy of 3D PDM
  As well as 2D PDM, 3D PDM has a macroscopically degenerate ground state. However, 3D PDM has no analytical solution. Therefore, we calculate the residual entropy of PDM on a cubic lattice and compare it with the value calculated by PEPS and asymptotic expansion.

- Comprehensive understanding of the higher dimensional MDM
  The criticality of 3D MDM is known for several lattice geometries. However, the critical behavior of 3D MDM has not clarified. We study three-dimensional properties by two approaches. First, we analyze a finite number of layer models, such as two or three layers, that DMRG can use. Finite layer models are classified as 3D systems, but they exhibit critical behaviors that are unique to finite layer systems. Second, we analyze the cubic lattice model by HOTRG. As a result, we compare the layer lattice model with the cubic lattice model to obtain a comprehensive understanding of the three-dimensional system. In particular, we recognize the cubic lattice as a layer model with infinite layers, and discuss the connection from the critical properties of finite layers to the critical properties of infinite systems.

- Asymptotic behavior of the spectrum of HOTRG
  In renormalization process of HOTRG calculation, the finite number of basis is retained depending on the importance of eigenvalues (singular values) in HOSVD. Therefore, to understand the applicable of HOTRG, it is important to know the behavior of the eigenvalues of HOTRG. Ref.[67] show that the structure of the spectrum of HOTRG can be described by the picture based on the corner transfer matrix. Using this picture, we study the asymptotic behavior of the spectrum of HOTRG. In particular, we derive an asymptotic spectral relation between the HOTRG and DMRG that is valid only for integrable models.

This Thesis is organized as follows. Chapter 2 outlines the important properties of PDM and MDM, such as the existence of analytical solutions, correspondence with the Ising model, and criticality.

In Chapter 3, after reviewing the DMRG and HOTRG algorithms used in this study, we introduce a new algorithm for HOTRG that can reduce the memory cost.

In Chapter 4, we propose the critical behavior of the monomer density as our conjecture, and we verify the conjecture numerically by using DMRG and HOTRG. Furthermore, the relationship between the Ising model and MDM will be discussed from the perspective of critical behavior.

In Chapter 5, we analyze the critical behavior of MDM on finite layer lattices such as two- or three layer model by DMRG. The two layer model and the three layer model show different criticalities. For the two-layer model, calculations are also performed by varying the dimer activity on the edge perpendicular to the layer surface. From this analysis, we show that there is a transition point where criticality seems to change.

In Chapter 6, we calculate the residual entropy and analyze critical behavior of the 3D MDM by using HOTRG. In this HOTRG calculation, we use our parallel computation method which is introduced in Sec.3.2. We will see to what extent HOTRG can determine the critical behavior of 3D MDM.

In Chapter 7, we analyze the asymptotic behavior of the spectrum of HOTRG. First, we theoretically determine the asymptotic form of the integrable model. In particular, we compare the distributions of the asymptotic spectra of HOTRG and DMRG and clarify the relationship between them. Next, we show numerically that this relationship holds for integrable models and does not hold for non-integrable models.

Chapter 2

General introduction to the monomer-dimer model

In this chapter, we introduce the pure dimer model (PDM) and the monomer-dimer model (MDM) and show several basic properties of each model. Throughout this thesis we discuss only classical rigid models, which have no interaction other than hard core infinite repulsive forces. PDM and MDM are able to be extended to include more physical circumstances such as interactions, thermal effects and quantum effects. PDM and MDM means classical rigid models except where we mention it.

2.1 Definition of the monomer-dimer model

2.1.1 Pure dimer model

PDM is a model defined on a fully packed lattice with only dimers occupying adjacent pairs of lattice sites (Fig.2.1).

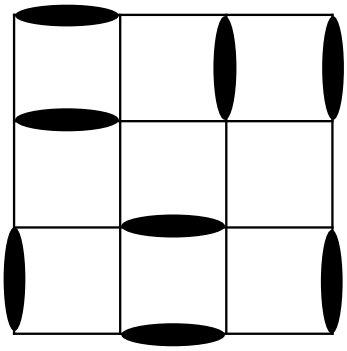

FIGURE 2.1: Graphical representation of the pure dimer model defined on a square lattice.

Given a model with no interactions between dimers, the thermodynamic properties of this system can be determined from the number of ways in which the dimers are arranged. If we indicate the number of ways to arrange N_2 horizontal dimers and N_2' dimers on $m \times n$ square lattice by $g_{mn}(N_2, N_2')$, the grand partition function is given as

$$Z_{mn}(x, y) = \sum_{\{N_2, N_2'\}} g_{mn}(N_2, N_2') x^{N_2} y^{N_2'}, \tag{2.1}$$

where the sum runs over all configurations where N_2, N_2' satisfies $2(N_2 + N_2') = mn$, and x, y denote the activity of dimer in horizontal and vertical directions, respectively.

The entropy in the thermodynamic limit is

$$f(x,y) = \lim_{n,m\to\infty} \frac{1}{mn} \log Z_{mn}(x,y). \tag{2.2}$$

For the symmetric activity of dimer, i.e. $x = y = 1$, (2.1) reduces to

$$Z_{mn} := Z_{mn}(1,1) = \sum_{\{N_2, N_2'\}} g_{mn}(N_2, N_2'), \tag{2.3}$$

and this is the case we will consider in this thesis.

2.1.2 Monomer-dimer model

MDM is a more general model, with not only dimers, but also monomers (vacant lattice sites) are present(Fig.2.2).

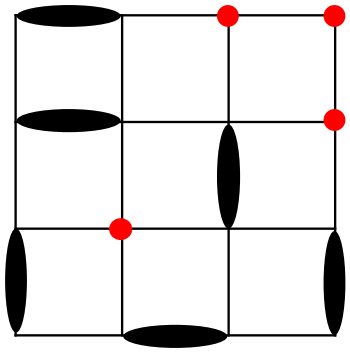

FIGURE 2.2: Graphical representation of the monomer-dimer model defined on a square lattice. Black bars occupying two sites represent dimers, and red circles represent monomers.

In MDM the lattice is not completely filled by dimers, which complicates the problem, and properties such as the solution of the free energy and phase transitions are very different from those in PDM. The grand partition function of MDM is defined as follows same as PDM:

$$\Xi_{mn}(z) = \sum_{s=0}^{mn} w_{mn}(s) z^s, \tag{2.4}$$

where z is a monomer activity and $w_{mn}(s)$ is the number of ways to arrange $(mn-2s)$ dimers on $m \times n$ lattice sites (we assume that mn is even). The entropy in the thermodynamic limit is given as follows:

$$\psi(z) = \lim_{m,n\to\infty} \frac{1}{mn} \log \Xi_{mn}(z). \tag{2.5}$$

In the limit of $z \to 0$, that is, in the absence monomer, MDM is reduced to PDM:

$$\lim_{z\to 0} \Xi_{mn}(z) = w_{mn}(0) = Z_{mn}. \tag{2.6}$$

Since our study contains the criticality of monomer density, we introduce the monomer density depending on z here:

$$\rho_{mn}(z) = \frac{1}{\Xi_{mn}} \sum_{s=1}^{N} \frac{s}{mn} \cdot w_{mn}(s) z^s. \tag{2.7}$$

(2.7) can be written as the differentiation of the entropy about z:

$$\rho_{mn}(z) = z \frac{d\psi_{mn}(z)}{dz}. \tag{2.8}$$

We notate the monomer density in the thermodynamic limit as $\rho(z)$:

$$\rho(z) = \lim_{m,n\to\infty} \rho_{mn}(z). \tag{2.9}$$

2.2 Analytical solution for the pure dimer model

The partition function of the $2d$ PDM on the square lattice can be solved analytically by the Pfaffian method[7–9]. Analytical representations of partition functions on various lattices such as honeycomb[68], triangular[69], and kagome[70], as well as square lattices, have been discovered. On the other hand, in general $2d$ MDM, there is no analytical solution, but a limited situation where the monomer is doped at a specific position[11, 12]. In this section, we review the analytic solution on the $2d$ square lattice following Ref.[7].

We will give an analytic representation of (2.1) and (2.2) when $|y| \leq |x|$ and m is even. The proposition to be shown is as follows.

$$f(x,y) := \lim_{m,n\to\infty} \frac{1}{mn} \log Z_{mn}(x,y) = \frac{1}{2}\log x + \frac{1}{\pi}\Lambda_2\left(\frac{y}{x}\right), \tag{2.10}$$

$$\Lambda_2(u) = \frac{1}{2i}\left[L_2(iu) - L_2(-iu)\right], \tag{2.11}$$

$$L_2(v) = -\int_0^v ds \frac{1}{s}\log(1-s). \tag{2.12}$$

We divide the process of the proof into several steps.

First, let us represent the partition function (2.1) in a Pfaffian form, which is an algebraic quantity of matrices defined for PDM. Assign $p_1, p_2, \cdots, p_{mn}$ to each site, and denote the dimer occupying sites p_i, p_j as $|p_i; p_j|$. To make the relationship between the configuration and the index unique, the following definitions and conditions are given:

$$p = (j-1)m + i \text{ for the coordinate } (i,j), \tag{2.13}$$

$$p_1 < p_2; p_3 < p_4; \cdots; p_{mn-1} < p_{mn}, \tag{2.14}$$

$$p_1 < p_3 < p_5 < \cdots < p_{mn-1}. \tag{2.15}$$

The conditions (2.14) and (2.15) are included in the definition of a Pfaffian. The Pfaffian is defined for a triangular array of components $a(k;k')$ of $N \times N$ matrix

$(k = 1, \cdots, N; k' = 1, \cdots, N; k < k',\ N$: even):

$$\mathrm{Pf}\{a(k;k')\} = \sum_{P}{}' \delta_P a(k_1;k_2)a(k_3;k_4)\cdots a(k_{N-1};k_N), \tag{2.16}$$

$$k_1 < k_2; k_3 < k_4; \cdots; k_{N-1} < k_N,\ k_1 < k_3 < k_5 < \cdots < k_{N-1}, \tag{2.17}$$

where Σ'_P is summation through the all permutation obeying (2.17) and δ_P is sign for the permutation. By analogy between the definition of the Pfaffian and the conditions of configurations, we can find the matrix $D(p;p')$ that satisfies

$$Z_{mn}(z,z') = \mathrm{Pf}\{D(p;p')\}. \tag{2.18}$$

Since the partition function of PDM is the number of ways to arrange the dimers, we should determine the D where $\delta_P D(p_1;p_2)D(p_3;p_4)\cdots D(p_{mn-1};p_{mn})$ takes the value $+1(>0)$ for a given configuration. To satisfy this condition, we give the matrix D the following properties.

- $D(p;p') = 0$ if there is no dimer between sites p and p'.
- $D(p;p') = -D(p';p) = \begin{cases} |x| & \text{(horizontal dimer exist between } p \text{ and } p'), \\ |y| & \text{(vertical dimer exist between } p \text{ and } p'). \end{cases}$
- Determine the sign of $D(p;p')$ by arrows along the edges of the lattice (the rules for placing the arrows are described below):
  $\begin{cases} D(p;p') > 0 & \text{(if an arrow points from } p \text{ to } p'), \\ D(p;p') < 0 & \text{(if an arrow points from } p' \text{ to } p). \end{cases}$

To describe the rule of arrangement of arrows, we introduce the *standard configuration* shown as Fig.2.3:

$$C_0 = |(1,1);(2,1)|(3,1);(4,1)|\cdots|(m-1,n);(m,n)|. \tag{2.19}$$

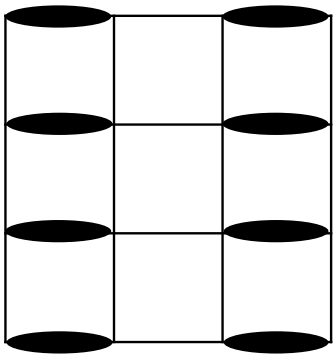

FIGURE 2.3: Standard configuration.

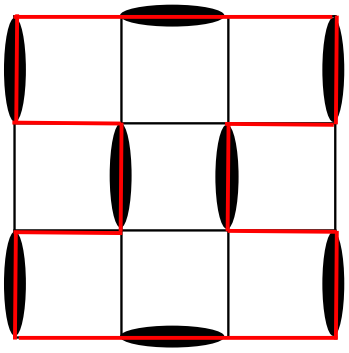

FIGURE 2.4: Polygon constructed from the standard configuration.

An arbitrary configuration of the dimer can be represented as an assembly of *polygons*, and a polygon is constructed from a standard configuration by shifting all dimers clockwise or counter-clockwise one step(see Fig.2.3 and Fig.2.3). Since the number of permutations to construct the polygon from the standard configuration

is odd (the proof is given in Ref.[7]), $D(p_1;p_2)D(p_3;p_4)\cdots D(p_{mn-1};p_{mn})$ must be negative for $\delta_P D(p_1;p_2)D(p_3;p_4)\cdots D(p_{mn-1};p_{mn})$ to be positive. To achieve such a condition, the parity of the number of edges facing either direction (we call orientation parity) should be odd for all cycles of even length. The choice of the directions of arrows is shown in Fig.2.5, so the matrix element of D is determined as follows:

$$D(i,j;i+1,j) = x \ (1 \le i \le m-1, 1 \le j \le n), \tag{2.20}$$
$$D(i,j;i,j+1) = y \ (1 \le i \le m, 1 \le j \le n-1), \tag{2.21}$$
$$D(i,j;i',j') = 0 \ (\text{otherwise}). \tag{2.22}$$

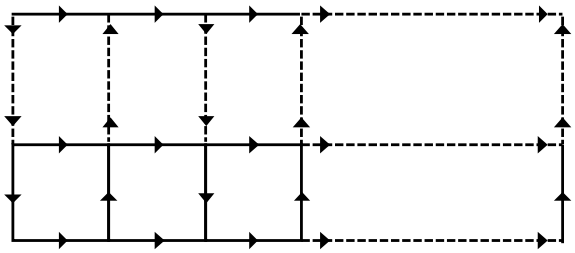

FIGURE 2.5: Orientation parity.

From the above discussion, we get the matrix D which satisfies $Z_{mn}(z,z') = \mathrm{Pf}\{D(p;p')\}$.

As a next step, we show the calculation of the Pfaffian of matrix D. Since D is skew-symmetric matrix,

$$Z^2_{mn}(x,y) = \{\mathrm{Pf}D\}^2 = \det D. \tag{2.23}$$

D can be transformed to $\tilde{D}$ by unitary transformation:

$$\tilde{D}(k,l;k',l') = 2ix\delta_{k,k'}\delta_{l,l'}\cos\left(\frac{k\pi}{m+1}\right) - 2iy\delta_{k+k',m+1}\delta_{l,l'}\cos\left(\frac{l\pi}{n+1}\right). \tag{2.24}$$

Thus the determinant of D is calculated as

$$\begin{aligned}\det D = \det\tilde{D} &= \prod_{k=1}^{\frac{1}{2}m}\prod_{l=1}^{n}\begin{vmatrix} 2ix\cos\left(\frac{k\pi}{m+1}\right) & -2iy\cos\left(\frac{l\pi}{n+1}\right) \\ -2iy\cos\left(\frac{l\pi}{n+1}\right) & -2ix\cos\left(\frac{k\pi}{m+1}\right)\end{vmatrix} \\ &= \begin{cases} 2^{\frac{1}{2}mn}\prod_{k=1}^{\frac{1}{2}m}\prod_{l=1}^{\frac{1}{2}n}\left[x^2\cos^2\left(\frac{k\pi}{m+1}\right)+y^2\cos^2\left(\frac{l\pi}{n+1}\right)\right], & (n:\text{even}) \\ 2^{\frac{1}{2}m(n-1)}x^{\frac{1}{2}m}\prod_{k=1}^{\frac{1}{2}m}\prod_{l=1}^{\frac{1}{2}(n-1)}\left[x^2\cos^2\left(\frac{k\pi}{m+1}\right)+y^2\cos^2\left(\frac{l\pi}{n+1}\right)\right]. & (n:\text{odd}) \end{cases}\end{aligned} \tag{2.25}$$

Using the identity which holds only for even m

$$\prod_{k=1}^{\frac{1}{2}m} 4\left[u^2+\cos^2\left(\frac{k\pi}{m+1}\right)\right] = \frac{[u+(1+u^2)^{\frac{1}{2}}]^{m+1}-[u-(1+u^2)^{\frac{1}{2}}]^{m+1}}{2(1+u^2)^{\frac{1}{2}}}, \tag{2.26}$$

(2.25) becomes

$$Z_{mn}(x,y) = \prod_{l=1}^{[\frac{1}{2}n]} 2^{-\frac{1}{2}} \left(1+\xi^2\cos^2\left(\frac{l\pi}{n+1}\right)\right)^{-\frac{1}{2}} \times \left\{ \left[\xi\cos\left(\frac{l\pi}{n+1}\right) + \left(1+\xi^2\cos^2\left(\frac{l\pi}{n+1}\right)\right)^{\frac{1}{2}}\right]^{m+1} - \left[\xi\cos\left(\frac{l\pi}{n+1}\right) - \left(1+\xi^2\cos^2\left(\frac{l\pi}{n+1}\right)\right)^{\frac{1}{2}}\right]^{m+1} \right\}, \tag{2.27}$$

where $\xi = y/x$ and $[n/2] = n/2$ or $(n-1)/2$ for n is even or odd. In the limit $m \to \infty$,

$$Z_n(x,y) = \lim_{m\to\infty}\{Z_{mn}(x,y)\}^{1/m} = z^{\frac{1}{2}n}\left[\xi\cos\left(\frac{l\pi}{n+1}\right) + \left(1+\xi^2\cos^2\left(\frac{l\pi}{n+1}\right)\right)^{\frac{1}{2}}\right]. \tag{2.28}$$

In the limit $n, m \to \infty$, Z_{mn} can be expressed in an integral form as follows:

$$\begin{aligned} Z(x,y) &= \exp\left[\log\left(\lim_{n\to\infty} Z_n(x,y)\right)\right] \\ &= z^{\frac{1}{2}} \exp\left\{\lim_{n\to\infty}\sum_{l=1}^{n/2}\frac{1}{n}\log\left[\xi\cos\left(\frac{l\pi}{n+1}\right) + \left(1+\xi^2\cos^2\left(\frac{l\pi}{n+1}\right)\right)^{\frac{1}{2}}\right]\right\} \\ &= z^{\frac{1}{2}} \exp\left\{\frac{1}{\pi}\int_0^{\frac{\pi}{2}} d\omega \log\left[\xi\cos\omega + (1+\xi^2\cos^2\omega)^{\frac{1}{2}}\right]\right\}. \end{aligned} \tag{2.29}$$

When $|x| \geq |y|$, the integrand can be expand in terms of ξ, and $Z(x,y)$ is expressed as a simple form:

$$\begin{aligned} \log Z(x,y) &= \frac{1}{2}\log x + \frac{1}{\pi}\sum_{j=0}^{\infty}(-1)^j \frac{1}{(2j+1)^2}\xi^{2j+1} \\ &=: \frac{1}{2}\log x + \frac{1}{\pi}\Lambda_2(\xi). \end{aligned} \tag{2.30}$$

In special case of $x = y = 1$ ($\xi = 1$),

$$f(1,1) = \log Z(1,1) = \frac{1}{\pi}\Lambda_2(1) = 0.291560904030818\cdots, \tag{2.31}$$

where $G = \Lambda_2(1)$ is called a Catalan's constant.

The exact solutions of the zero-point entropy on various two-dimensional lattices are summarized as Table2.1.

TABLE 2.1: Analytical solution of the zero-point entropy per-site on various two-dimensional lattices. These values are based on Ref.[7–9, 29, 68–70].

Geometry	entropy at $z = 0$: $\psi(0)$
square	0.291560904030818...
honeycomb	0.161532973609725...
triangular	0.428594537464958...
kagome	0.231049060...
triangular-kagome	0.231049060...

2.3 Correspondence between the dimer model and Ising model

In 1963, Kasteleyn showed that the Ising model on a square lattice is equivalent to PDM on a cluster lattice, which is a non-planar lattice[24]. It was then generally shown that the Ising model can be mapped to a PDM on a deformed planar lattice[26]. In this section, we review the correspondence relation between the Ising model and PDM on the cluster lattice.

In the high temperature expansion, the Ising model is expressed as a bond graph, where the edges represent the interactions between nearest neighbor sites. In the bond graph, the only terms that contribute to the partition function are loop diagrams where every vertex has 0, 2 or 4 bonds (Fig.2.6).

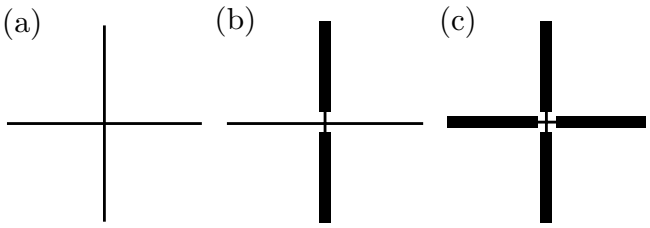

FIGURE 2.6: Three types of vertices that contribute to Ising partition function in the high temperature expansion.

The edge of the high temperature expansion in the Ising model appears to correspond to the dimer in PDM. However, overlapping of dimers at the same site is prohibited in PDM, and the bond of the Ising model does not directly correspond to a dimer. Then, by transforming the vertices into a cluster lattice as shown in Fig.2.7, we can project the Ising model on the square lattice (Q) to the PDM defined on the cluster lattice (Q').

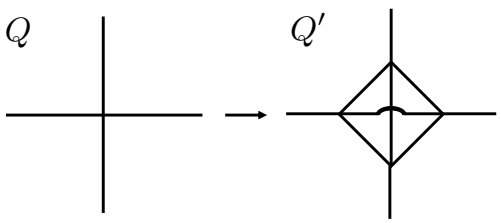

FIGURE 2.7: The construction of the cluster lattice.

After the projection of the Ising model to the dimer model on the cluster lattice, the partition function of the Ising model can be evaluated using the Pfaffian method. However, in the process of placing the arrows on the edges, it must be noted that the projections of the vertices to the cluster lattice do not have a one-to-one correspondence. As shown in Fig.2.8, a vertex with two or four bonds has only one counterpart, while a vertex with no bonds has three counterparts.

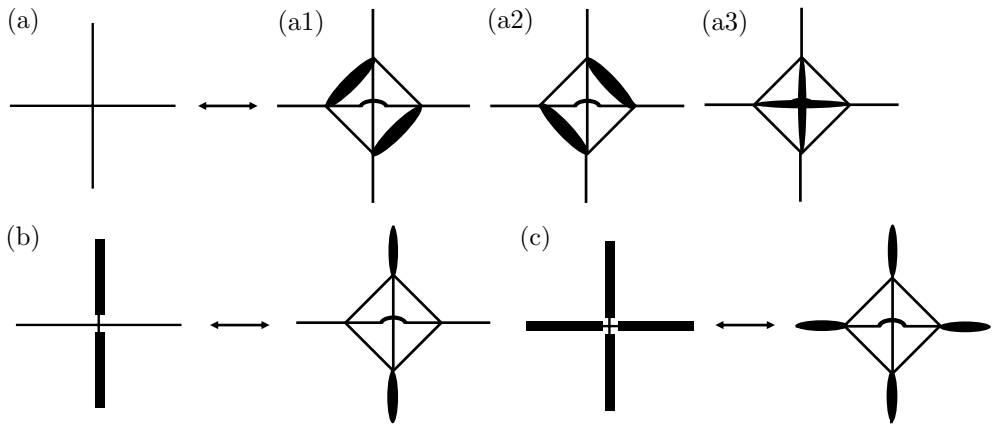

FIGURE 2.8: The construction of the cluster lattice.

However, this one-to-three correspondence does not affect the counting of diagrams in the high temperature expansion of the Ising model. We can arrange the arrows on the lattice Q' so that the orientation parity of all even cycles that do not self-intersect is odd (Fig.2.9). Therefore, a vertex (a) or (b) is contributed to the counting of

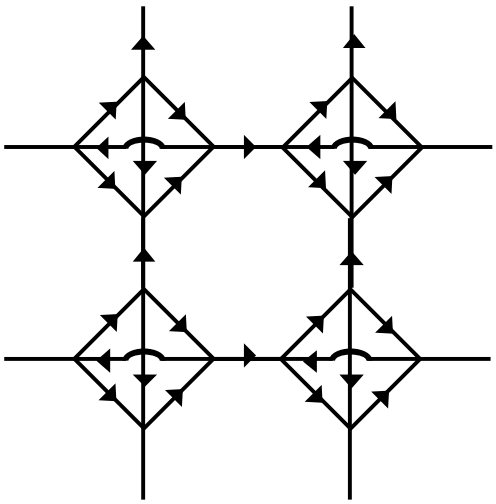

FIGURE 2.9: The construction of the cluster lattice.

configurations as before. For (a), (a1) and (a2) is counted as $+1$, while (a3) is counted as (-1), since the translation from (a1) or (a2) to (a3) needs odd permutations of sites and even shifts of arrows. As a result, the contribution in (a) is $(+1)+(+1)-(+1) = +1$, and the perturbation function of the Ising model can be evaluated by applying the conventional orientation rule to the PDM on the cluster lattice Q'.

The correspondence between PDM and the Ising model at high temperature expansion can be extended to correspondence between MDM and the Ising model with magnetic fields[31].

2.4 Criticality of monomer-dimer model

Depending on the geometry of a lattice, MDM exhibits the critical phenomena. For example, in MDM on a square lattice, when monomer activity z is taken as a parameter, there is a critical point (CP) at the no-monomer point $z = 0$ (Fig.2.10)[24, 31].

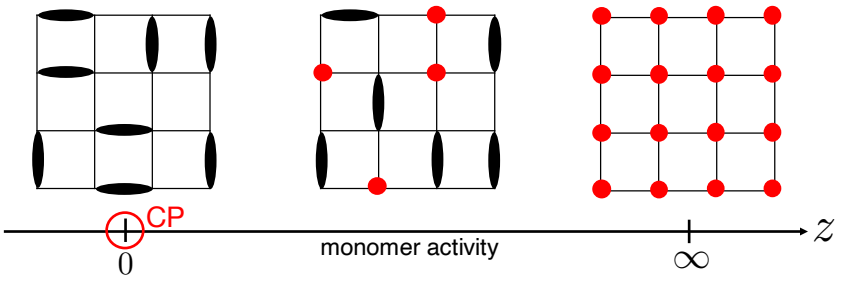

FIGURE 2.10: Critical point at the no-monomer point.

The criticality of PDM is defined as the appearance of power-law of the monomer-monomer correlator or the dimer-dimer correlator. The definitions of these correlation functions will be presented, as well as an explanation of the key concept of criticality: the confinement of monomer pairs.
We introduce the configuration expectation:

$$\langle A \rangle = \frac{\text{number of configurations under the constraint of } A}{\Xi(z=0)}, \tag{2.32}$$

$$A = \text{composite operator of } d_i(\boldsymbol{r}) \text{ or } m(\boldsymbol{r}), \tag{2.33}$$

where $d_i(\boldsymbol{r})$ represents the creation of dimer on the edge between site $\boldsymbol{r}$ and $\boldsymbol{r} + \boldsymbol{e}_i$ and $m(\boldsymbol{r})$ represents the creation of monomer at site $\boldsymbol{r}$. By using the configuration expectation (2.32), the correlation functions are defined as follows:
· dimer-dimer correlation function

$$C_{ij}(\boldsymbol{r}_1, \boldsymbol{r}_2) := \langle d_i(\boldsymbol{r}_1) d_j(\boldsymbol{r}_2) \rangle_c = \langle d_i(\boldsymbol{r}_1) d_j(\boldsymbol{r}_2) \rangle - \langle d_i(\boldsymbol{r}_1) \rangle \langle d_j(\boldsymbol{r}_2) \rangle , \tag{2.34}$$

· monomer-monomer correlation function

$$M(\boldsymbol{r}_1, \boldsymbol{r}_2) := \langle M(\boldsymbol{r}_1) M(\boldsymbol{r}_2) \rangle_c . \tag{2.35}$$

For example, in PDM on the square lattice[25, 71],

$$C_{ij}(r) \sim r^{-2}, \quad M(r) \sim r^{-\frac{1}{2}}. \tag{2.36}$$

Next, we define a confinement of monomers. Confinement is a concept that describes whether or not two inserted monomers can be infinitely separated from each other. The free energy of two inserted monomers separated at the distance $r := |\boldsymbol{r}_1 - \boldsymbol{r}_2|$ is defined as

$$F(r) = -\log \Xi^{(2)}(\boldsymbol{r}_1, \boldsymbol{r}_2), \tag{2.37}$$

where $\Xi^{(2)}(\boldsymbol{r}_1, \boldsymbol{r}_2)$ is the partition function of dimer system with two monomers at $\boldsymbol{r}_1$ and $\boldsymbol{r}_2$. Using (2.37), we defined a phase in which $F(r)$ increases with separation

as "confined" and one in which it does not as "deconfined". The criticality and confinement depend on the geometry of the lattice, and these properties are shown in Table2.2 for several examples of PDM on 2d and 3d lattices.

TABLE 2.2: Criticality and confinement for various lattice. These all take into account the case where the monomer activity is isotropic.

Geometry	criticality	confinement
two dimensions[29]		
square	critical	confined
honeycomb	critical	confined
triangular	non-critical	deconfined
kagome	non-critical	deconfined
triangular-kagome	non-critical	deconfined
three dimensions[61]		
cubic	critical	deconfined
fcc	non-critical	deconfined
3d Fisher	non-critical	confined and deconfined

2.5 Mapping to a bosonic field theory

The monomer-dimer systems defined on the bipartite lattice can be mapped to a bosonic field theory using height representations[72]. This framework allows us to access the properties of MDM, such as criticality and confinement, as a bosonic field theory. In this framework, PDM is mapped to the free Gaussian theory, and MDM is mapped to the Gaussian theory with a dual field. In this section, we refer to the review section of the height representation of dimers in Ref.[73].

2.5.1 Height representation of the pure dimer model

First, we map the dimers on the bipartite lattice to the "magnetic field". A bipartite lattice is defined as the lattice in which sites are divided into two sets, such that one site and its neighbors always belong to different groups (Fig.2.11). A non-bipartite lattice is defined as any lattice other then a bipartite lattice. By definition of a

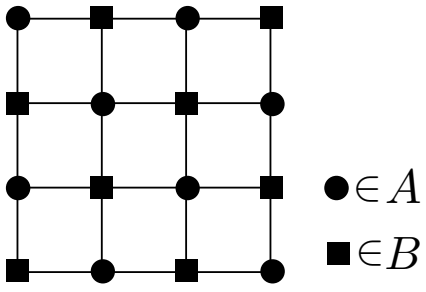

FIGURE 2.11: Graphic representation of bipartite lattice. The site represented by the round symbol and its neighboring site represented by the square symbol always belong to different groups A and B, respectively.

bipartite lattice, each dimer touches one site on each sublattice. Using a sign factor

$\epsilon_{\boldsymbol{r}}$, the field variables are defined from the dimer variables $n_i(\boldsymbol{r})$:

$$B_i(\boldsymbol{r}) = \epsilon_{\boldsymbol{r}} \left(n_i(\boldsymbol{r}) - \frac{1}{q} \right), \tag{2.38}$$

where q is coordination number that is the number of edges of one site, and $n_i(\boldsymbol{r})$ satisfies following relation:

$$n_i(\boldsymbol{r}) = \begin{cases} 1 & \text{(the edge between } \boldsymbol{r} \text{ and } \boldsymbol{r} + \boldsymbol{e}_i \text{ is occupied by a dimer);} \\ 0 & \text{(otherwise).} \end{cases} \tag{2.39}$$

In case of PDM, the close-packed hard core condition

$$\sum_i (n_i(\boldsymbol{r}) + n_i(\boldsymbol{r} - \boldsymbol{e}_i)) = 1 \quad \text{for all site } \boldsymbol{r} \tag{2.40}$$

is satisfied at each site. (2.40) means that the number of dimers touching one site must be one. From (2.40), $B_i(\boldsymbol{r})$ satisfies the lattice divergence-free condition:

$$\sum_i (B_i(\boldsymbol{r}) + B_i(\boldsymbol{r} - \boldsymbol{e}_i)) = 0 \quad \text{for all site } \boldsymbol{r}. \tag{2.41}$$

According to (2.38) and (2.41), PDM on a bipartite lattice can be mapped to a divergence-free magnetic field theory. Above discussion can always be applied to the bipartite lattice, regardless of the dimension.

In two-dimensions, (2.41) is solved by introducing the scalar height function h defined on the dual lattice[74]:

$$B_i(\boldsymbol{r}) = \epsilon_{ij} \Delta_j h, \tag{2.42}$$

where ϵ_{ij} is Levi-Civita symbol and Δ_j represents lattice derivative. According to (2.42), the height function can be constructed by following rules[75].
(1) Chose one dual lattice site a and set the height function at this site to zero : $h_a = 0$.
(2) Moving anticlockwise around the sites, we change the height function by

$$\begin{cases} \pm \left(1 - \frac{1}{q}\right) & \text{when an edge occupied by a dimer is crossed;} \\ \mp \frac{1}{q} & \text{when an empty edge is crossed,} \end{cases} \tag{2.43}$$

where the sign corresponds to the type of the sublattice. An example of the height representation for a square lattice is shown in Fig.2.12. To study the long-wavelength properties, we construct the continuum field theory by replacing the magnetic field and the height function on the lattice by coarse-grained field $\boldsymbol{B}(\boldsymbol{r})$ and $h(\boldsymbol{r})$ obeying $B_i(\boldsymbol{r}) = \epsilon_{ij} \partial_j h(\boldsymbol{r})$. The action for PDM in the height representation regime is given as

$$S_{\mathrm{PDM}} = \int d^2\boldsymbol{r} \frac{\kappa}{2} |\boldsymbol{B}|^2 = \int d^2\boldsymbol{r} \frac{\kappa}{2} |\nabla h|^2, \tag{2.44}$$

where κ is the stiffness. In the case of non-interacting dimers on square lattice, the stiffness is determined to be $\kappa = \pi$ by comparing the observed values in the continuum regime with the exact results in PDM using the Pfaffian method[25].

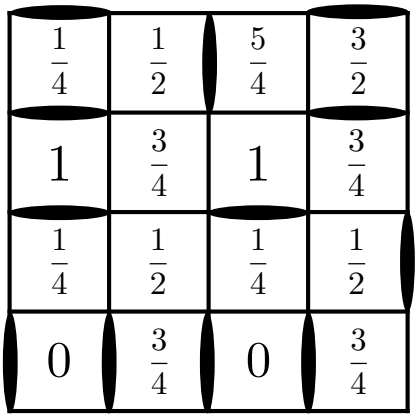

FIGURE 2.12: An example of the height representation for the dimer model on the square lattice.

2.5.2 Height representation of the monomer-dimer model

PDM is mapped to the free Gaussian theory. On the other hand, MDM can be mapped to the Gaussian theory with the dual field. The monomer is seen as a defect on the lattice. Therefore, at the lattice site where a monomer exists, the condition for dimer variables $n_i(\boldsymbol{r})$ is given as

$$\sum_i (n_i(\boldsymbol{r}) + n_i(\boldsymbol{r} - \boldsymbol{e}_i)) = 0. \tag{2.45}$$

From (2.45), the divergence of the magnetic field at the site where a monomer exists becomes

$$\begin{aligned} \sum_i (B_i(\boldsymbol{r}) + B_i(\boldsymbol{r} - \boldsymbol{e}_i)) &= \sum_i \epsilon_{\boldsymbol{r}} \left(n_i(\boldsymbol{r}) + n_i(\boldsymbol{r} - \boldsymbol{e}_i) - \frac{2}{q} \right) \\ &= -\sum_i \epsilon_{\boldsymbol{r}} \cdot \frac{2}{q} \\ &= -\epsilon_{\boldsymbol{r}} =: Q_{\boldsymbol{r}}. \end{aligned} \tag{2.46}$$

(2.46) represents that a monomer corresponds to a monopole whose charge is $Q_{\boldsymbol{r}}$. As an example, we consider the MDM with two monomers exist at $\boldsymbol{r}_+$ and $\boldsymbol{r}_-$. In the case of the bipartite lattice, each monomer is on a different sublattice and the sign of each monopole charge is opposite. To construct the continuum theory, (2.46) is coarse-grained as

$$\nabla \cdot \boldsymbol{B} = Q(\boldsymbol{r}), \quad Q(\boldsymbol{r}) = \mathcal{K}_w(\boldsymbol{r} - \boldsymbol{r}_+) - \mathcal{K}_w(\boldsymbol{r} - \boldsymbol{r}_-), \tag{2.47}$$

where $\mathcal{K}_w$ is a coarse-grained kernel with width w and satisfies normalization

$$\int d^2\boldsymbol{r} \mathcal{K}_w(\boldsymbol{r} - \boldsymbol{r}') = 1. \tag{2.48}$$

The general solution for (2.47) is [76]

$$B_i = -\partial_i \phi + \epsilon_{ij} \partial_j h, \tag{2.49}$$

where h is height function of divergence-free theory, and ϕ is a dual field obeying Poisson equation $\nabla^2\phi = -Q(\boldsymbol{r})$. The action for MDM in the continuum field regime is

$$S_{\mathrm{MDM}}[\phi, h] = \int d^2\boldsymbol{r}\frac{\kappa}{2}(|\nabla\phi|^2 + |\nabla h|^2). \tag{2.50}$$

Integrating out the degree of freedom for h in (2.50), we get the monomer distribution function as follows:

$$\begin{aligned} G_{\mathrm{m}}(\boldsymbol{R}) &= \frac{1}{Z}\int \mathcal{D}h(\boldsymbol{r})e^{-S_{\mathrm{MDM}}[\phi,h]} \\ &= e^{-\int d^2\boldsymbol{r}\frac{\kappa}{2}|\nabla\phi|^2}, \end{aligned} \tag{2.51}$$

where Z is the partition function of PDM and $\boldsymbol{R} = \boldsymbol{r}_+ - \boldsymbol{r}_-$. Here we consider the case where the two monomers are far enough apart that they can be regarded as point charges on each other : $|\boldsymbol{R}| \gg w$. In this problem-setting, the Poisson equation becomes

$$-\nabla^2\phi = Q(\boldsymbol{r}) = \delta^{(2)}(\boldsymbol{r} - \boldsymbol{r}_+) - \delta^{(2)}(\boldsymbol{r} - \boldsymbol{r}_-), \tag{2.52}$$

and (2.51) can be calculated easily as

$$G_{\mathrm{m}}(\boldsymbol{R}) = \exp\left[-\frac{\kappa}{2\pi}\log|\boldsymbol{R}|\right] = |\boldsymbol{R}|^{-\frac{\kappa}{2\pi}}. \tag{2.53}$$

This expression was gotten by the fact that the solution for (2.52) is given as

$$\phi(\boldsymbol{r}) = \int d^2\boldsymbol{r}G(\boldsymbol{r} - \boldsymbol{r}')Q(\boldsymbol{r}') \tag{2.54}$$

$$\nabla^2 G(\boldsymbol{r}) = -\delta^{(2)}(\boldsymbol{r}), \tag{2.55}$$

and the solution for (2.55) is $G(\boldsymbol{r}) = -(2\pi)^{-1}\log|\boldsymbol{r}|$.

From (2.53), the long-distance behavior of the monomer-monomer correlation shows power-law $G_m(|\boldsymbol{R}|) \sim |R|^{-\kappa/2\pi}$ and suggests that PDM on the two-dimensional non-bipartite lattice is critical. In case of a square lattice, the stiffness is $\kappa = \pi$, so $G_m(|\boldsymbol{R}|) \sim |\boldsymbol{R}|^{-1/2}$, and this behavior is consistent with (2.36). Conversely speaking, κ can also be determined by comparing with the independent calculation of the monomer-monomer correlation. The potential (free energy) is defined as

$$-\log G_m(\boldsymbol{R}) \sim \log|\boldsymbol{R}|, \tag{2.56}$$

and this behavior indicates that monomers are confined.

Chapter 3

Numerical method

In this chapter, we introduce numerical methods to calculate the partition function and expectation values. Classical DMRG is a very powerful tool only in two-dimensional lattice, while HOTRG is extended to three or higher-dimensional lattice. However, as the dimension of the lattice increases, the dimension of the tensor also increases exponentially. Therefore, we devised a parallel computation algorithm to circumvent the memory limit of the 3D lattice (explained in Chap.3.2).

3.1 Higher-order tensor renormalization group (HOTRG)

3.1.1 Basic algorithms

We review the basic algorithm of HOTRG following Ref.[57] using an example of 2d MDM on a square lattice. The procedure for the honeycomb lattice and triangular lattice is shown in Appendix A.1. The partition function of MDM is

$$\Xi_N(z) = \sum_{s=0}^{N} w_N(s) z^s, \tag{3.1}$$

where N is the number of sites on the square lattice and $w(s)$ is the number of ways to arrange $(N-s)/2$ dimers and s monomers. In order to represent the partition function as a contraction of a tensor, it is necessary to determine the tensor defined at each site (called *local tensor*). In case of MDM, the tensor network representation of partition function and the local tensor is given as follows:

$$\Xi_N(z) = \mathrm{Tr} \prod_i T_{x_i x_i' y_i y_i'}, \quad x_i, x_i', y_i, y_i' \in \{0, 1\} \tag{3.2}$$

$$T_{x_i x_i' y_i y_i'} = \begin{cases} z & \text{if } x_i = x_i' = y_i = y_i' = 0; \\ 1 & \text{if only one index is 1;} \\ 0 & \text{otherwise,} \end{cases} \tag{3.3}$$

where i runs over all lattice sites and Tr is to sum over all indices of local tensors T. Virtual bond "1" means that the lattice site having a hand for covalent bond with an adjacent atom, while "0" corresponds to no hand. If all indices are "0", there is a monomer on the lattice site and it contributes to the partition function with number weight of z (Fig.3.1).

The goal of HOTRG is to compute Ξ_N for a sufficiently large system where the partition function as accurately as possible. To get such a large lattice system, we sum up the several adjacent tensors iteratively as a renormalization coarse-grained process. However, the number of components of the contracted tensor increase exponentially in the coarse-grained process. In HOTRG, to reduce computational costs, through

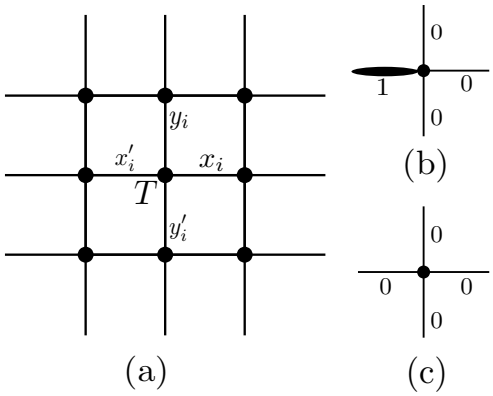

FIGURE 3.1: (a) Tensor representation for 2D square lattice. (b) and (c) Example of a local tensor representing the site where dimer and monomer exists respectively.

the higher-order singular value decomposition (HOSVD), the contracted tensor is trancated into a lower rank tensor. The details of these process are as follows.

First, we contract the vertically adjacent sites (Fig.3.2):

$$M_{XX'yy'} = \sum_a T_{x_1 x'_1 y a} T_{x_2 x'_2 a y'}, \tag{3.4}$$

where $X = x_1 \otimes x_2$, $X' = x'_1 \otimes x'_2$. After this contraction, the dimension of horizontal bond become the square of the original.

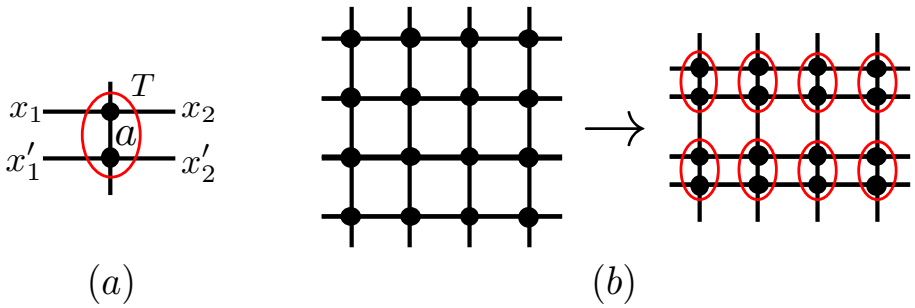

FIGURE 3.2: (a) Contraction of two local tensors. (b) Whole picture of vertical contraction.

Next, we use HOSVD to truncate the contracted tensor M to a lower rank tensor. HOSVD is an extension of the matrix singular value decomposition (SVD) to general higher-order tensors[77]:

$$M_{XX'yy'} = \sum_{ijkl} S_{ijkl} U^L_{Xi} U^R_{X'j} U^U_{yk} U^D_{y'l}, \tag{3.5}$$

where each U represents the unitary matrix and S_{ijkl} is called the core tensor. S_{ijkl} has the following two properties:

(1) orthogonality,

$$\sum_{i,k,l} S_{iJkl} S_{iJ'kl} = 0, \quad \text{if } J \neq J', \tag{3.6}$$

(2) ordered norm,

$$||S_{:,J,:,:}|| \geq ||S_{:,J',:,:}||, \quad \text{if } J < J', \tag{3.7}$$

$$||S_{:,J,:,:}|| := \sum_{a,b,c} (S_{aJbc})^2. \tag{3.8}$$

The norm $||S_{:,J,:,:}||$ plays the same role as the singular value of a matrix. Using these two properties, we can arrange the components of the tensor in order of importance, that is, in order of the norm of the core tensor. Technically, we construct a projection matrix to reduce the components of the tensor from dim$X$ to Dbond, which is the number of components to keep.

- Diagonalization in one direction

$$\sum_{j,k,l} M_{Ijkl} M_{I'jkl} = \left[U^L \Lambda^L (U^L)^\dagger \right]_{II'}, \tag{3.9}$$

where $\Lambda^L_i = ||S_{i,:,:,:}||^2$ and the eigenvalue of matrix $MM^\dagger$. So, singular value $||S_{i,:,:,:}||^2$ can be gotten by applying a diagonalization algorithm for $MM^\dagger$.

- Comparison of left and right singular values

If $M_{XX'yy'}$ is not symmetrical with respect to X and X', compare ϵ_L and ϵ_R to determine which component on the left or right should be truncated:

$$\epsilon_L = \sum_{i > D_{\text{bond}}} ||S_{i,:,:,:}||, \quad \epsilon_R = \sum_{j > D_{\text{bond}}} ||S_{:,j,:,:}||. \tag{3.10}$$

If $\epsilon_L < \epsilon_R$, we truncate the left components. Otherwise, we truncate the right components. D_{bond} represents the number of retained basis. In the case of MDM, the horizontal component of the contraction tensor is symmetric, so there is no need to consider the above discussion.

- Construction of the projection matrix

We consider the case of $\epsilon_L < \epsilon_R$. Same discussion can be applied to the case of $\epsilon_R < \epsilon_L$. Arranging the D_{bond} eigenvectors in order of the singular values, the projection matrices are constructed as

$$(P^L)_{iI} = (\tilde{U}^\dagger_L)_{iI}. \tag{3.11}$$

$\tilde{U}_L$ is constructed by keeping the first columns in U^L, and $\dim(i) = D_{\text{bond}}$, $\dim(I) = \dim(x_1) \cdot \dim(x_2)$.

- Projection

Projecting P^L to $M_{XX'yy'}$, we get the new renormalized local tensor (Fig.3.3):

$$T^{(\text{new})}_{xx'yy'} = \sum_{XX'} P^L_{xX} P^L_{x'X'} M_{XX'yy'}. \tag{3.12}$$

The four steps above illustrate the case of vertical coarse-graining. The same process should be followed for horizontal coarse-graining, and the coarse-graining should

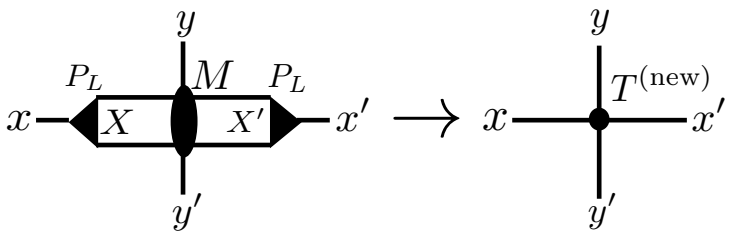

FIGURE 3.3: Trancation of two local tensors. Triangular symbols represent the projectors.

be repeated in turn until the partition function converges. This operation can be directly extended to higher dimensional systems by increasing the number of directions. The strength of HOTRG is that it can be easily made higher dimensional in this way.

I'll comment on the errors that appear in HOTRG. The truncation error in one direction is given as

$$\epsilon = 1 - \frac{\sum_{i=1}^{D_{\text{bond}}} (\Lambda_i)^2}{\sum_{i=1} (\Lambda_i)^2}. \tag{3.13}$$

This error is equivalent to the the deviation between the tensor T_{ijkl} and the truncated tensor $T_{ijkl}^{(\text{truncated})}$ when focusing on a certain component. Therefore, if we minimize the error in each direction, we can minimize the deviation

$$|T_{ijkl} - T_{ijkl}^{(\text{truncated})}|. \tag{3.14}$$

Conversely, by imposing this condition, HOSVD appears naturally.

Finally, we will discuss the larger component of the contraction tensor in iterative process. As the local tensor is contracted, its components grow larger and exceed the capacity of the number of digits the computer can handle. Therefore, to avoid such restrictions, we normalize the components of the contraction tensor at each iteration with characteristic values, e.g., the largest eigenvalue of $MM^\dagger$ or the largest component of $T^{(\text{new})}$. The transition of the partition function Ξ_N in iterative process can be represented as follows:

$$\begin{aligned} \Xi_N &= \text{Tr} \left\{ \prod_{i=1}^{N} T_0 \right\} = \text{Tr} \left\{ \prod_{i=1}^{N/2} T_1 \right\} \lambda_1^{N/2} \\ &= \cdots = \text{Tr}\{T_\nu\} \lambda_1^{N/2} \lambda_2^{N/2^2} \cdots \lambda_\nu^{N/2^\nu}, \end{aligned} \tag{3.15}$$

where λ_i is the largest eigenvalue of $MM^\dagger$ or the largest component of $T^{(\text{new})}$. In the large limit of N, each factor $\lambda_i^{N/2^i}$ is infinitely large. So, we convert the Ξ_N to the value per-site $\Xi_N^{1/N}$ with each iteration. The entropy per-site expressed as

$$s = \frac{\log \Xi_N}{N} = \sum_{i=1}^{\nu} \frac{1}{2^i} \log \lambda_i + \frac{1}{2^\nu} \log \text{Tr}\{T_\nu\}, \tag{3.16}$$

and we extract the first term and record it in each iteration.

For a local operator $\hat{O}$, its expectation value can be calculated in the framework of HOTRG. The expectation value is expressed in terms of the tensor network as

$$\langle \hat{O} \rangle = \frac{\mathrm{Tr}\{S_0 \prod_{i=1}^{N-1} T_0\}}{\mathrm{Tr}\{\prod_{i=1}^{N} T_0\}} = \frac{\mathrm{Tr}\{S_1 \prod_{i=1}^{N/2-1} T_1\}}{\mathrm{Tr}\{\prod_{i=1}^{N/2} T_1\}} = \cdots = \frac{\mathrm{Tr} S_n}{\mathrm{Tr} T_n}, \tag{3.17}$$

where S_0 is a local tensor which contains the corrections of the local operator $\hat{O}$ to T_0 (Fig.3.4). As can be seen from (3.17), the expected value is determined by the ratio of the renormalized S_n to the renormalized local tensor T_n. This algorithm is called the *impurity tensor method*.

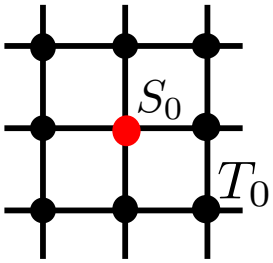

FIGURE 3.4: Tensor network representation of expectation value using impurity tensor.

3.1.2 Calculation of an expectation value using the environmental tensor

HOTRG and other tensor network approaches are optimization methods that minimize the truncation error of contracted tensor M defined in (3.4). In other words, HOTRG can optimize M locally, but it cannot optimize the entire partition function. As pointed out in Ref.[78], we need to consider the effect of the environment including all lattice sites except the two sites where M exists (Fig.3.5). TRG which includes the influence of environment is called Second Renormalization Group (SRG), and HOTRG which includes such an effect is nemed as Higher-Order SRG (HOSRG)[79]. To include the influence of environment, the environment tensor is introduced. In

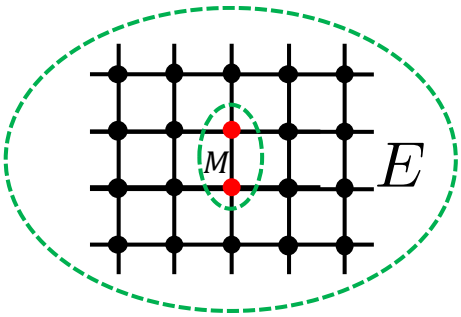

FIGURE 3.5: Environment tensor. The inner ellipse represents the vertically contracted tensor M, which is composed of two local tensors. Tensor E between inner and outer ellipse represents the environment tensor.

this section, we will focus on the construction of environment tensors, rather than the SRG process, and introduce the method we have developed for calculating expectation values using environment tensors.

Environment tensors are constructed by the backward iteration of HOTRG shown as Fig.3.6, where $E^{(n)}$, $T^{(n)}$, and $P^{(n)}$ represent the environment tensor, local tensor, and projector in nth iteration, respectively. The relationship between $E^{(n)}$ and $E^{(n+1)}$

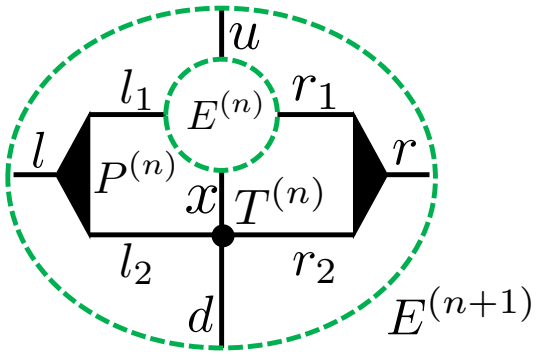

FIGURE 3.6: Relationship between nth and $(n+1)$th environment tensors.

is given as

$$E^{(n)}_{uxl_1r_1} = \sum_{l,r,d,l_2,r_2} E^{(n+1)}_{udlr} T^{(n)}_{l_1r_1xd} P^{(n)}_{l,l_2,l_1} P^{(n)}_{r,r_2,r_1}. \tag{3.18}$$

So, the first step in obtaining the environment tensor is to do a HOTRG and stack the renormalized local tensors $T^{(n)}$ and projections at each iteration step (n indicates the nth iterarion). After the forward iteration, we prepare the initial environment tensor $E^{(\mathrm{maxitr})}$ and perform backward iterations until we get $E^{(0)}$. Since $E^{(0)}$ is an environment tensor at the initial scale, we can calculate the expectation value by contracting this tensor with S_0 defined in (3.17) (Fig.3.7):

$$\langle \hat{O} \rangle = \frac{\mathrm{Tr}\left\{E^{(0)} \cdot S_0\right\}}{\Xi}. \tag{3.19}$$

When calculating the monomer density, it is necessary to determine S_0, which rep-

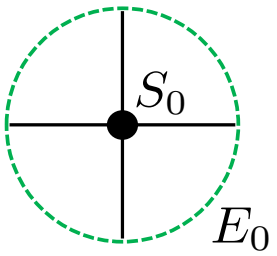

FIGURE 3.7: Calculation of the expectation value based on the environment tensor method.

resents the monomer number operator:

$$S_0 = S_m = \begin{cases} z & \text{if } x_i = x_i' = y_i = y_i' = 0; \\ 0 & \text{otherwise.} \end{cases} \tag{3.20}$$

3.2 Parallel computation method of HOTRG for three-dimensional analysis

HOTRG can be straightforwardly extended from a two-dimensional algorithm to a three-dimensional algorithm. However, in 3D, components of the local tensor increases in orders of magnitude, so the memory usage becomes massive. Therefore, even large computers with hundreds of gigabytes of memory capacity do not have sufficient computational power to accurately analyze the critical behavior. In this section, we give efficient algorithms to avoid the too large consumption of memory. We denote the number of retained components D_{bond} as D throughout this section.

3.2.1 Conventional three-dimensional algorithm of HOTRG

We review the conventional three-dimensional HOTRG[57] and identify bottlenecks in the algorithm that use large amounts of memory.

The change in extension from 2D to 3D is the increase in the number of projection directions, as shown in Fig3.8. The HOTRG process is divided into two steps. (1) construction of the projection tensor using HOSVD as in 3.5, and (2) construction of the renormalized local tensor by truncation using projection. We will count the memory usage, i.e. the number of components of tensor in each steps.

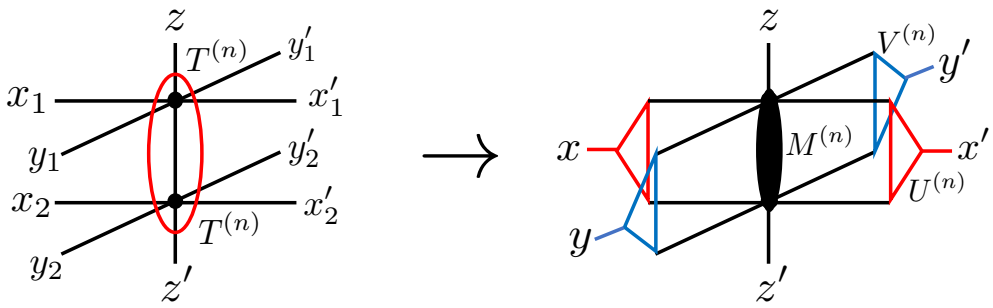

FIGURE 3.8: Renormalization in three-dimensional HOTRG. As an example, the contraction of local tensors in z direction is shown. In this case, projections for x and y direction need to be constructed.

(1) The contraction of two local tensors in z direction are given as:

$$M^{(n)}_{XX'YY'zz'} = \sum_i T^{(n)}_{x_1x_1'y_1y_1'zi} T^{(n)}_{x_2x_2'y_2y_2'iz'}, \tag{3.21}$$

where $X = x_1 \otimes x_2$, $X' = x_1' \otimes x_2'$, $Y = y_1 \otimes y_2$, and $Y' = y_1' \otimes y_2'$. The contracted matrix that we perform diagonalization to get x-direction projector is

$$(M^{(n)}_{z-x})_{II'} := \sum_{X'YY'zz'} M_{IX'YY'zz'} M_{I'X'YY'zz'}. \tag{3.22}$$

(3.22) is an extension from (3.9), as is M_{z-y} and the definition of the x and y directions. The memory costs for $M^{(n)}$ and $M^{(n)}_{z-x}$ are shown in Fig.3.9, and the former is D^{10} and the latter is D^4.

(2) Truncation of x and y components is given as

$$T^{(n+1)}_{xx'yy'zz'} = \sum_{X,X',Y,Y'} U^{(n)}_{xX} U^{(n)}_{x'X'} V^{(n)}_{yY} V^{(n)}_{y'Y'} M^{(n)}_{XX'YY'zz'}, \tag{3.23}$$

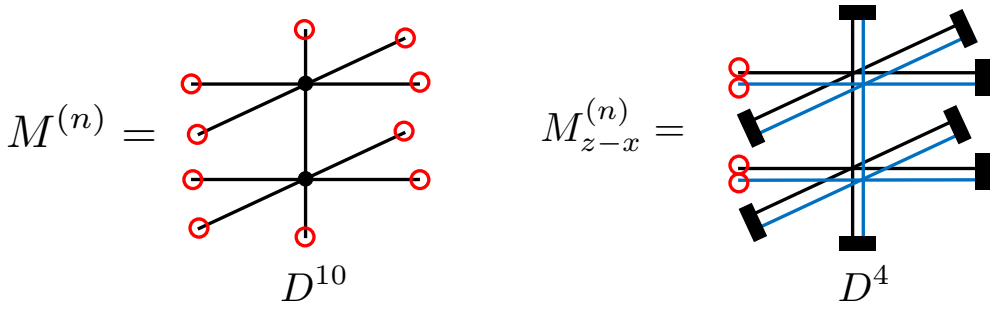

FIGURE 3.9: Graphical representation of memory costs for constructing $M^{(n)}$ and $M^{(n)}_{z-x}$. Red circles represent the components that need to be retained in computer memory, and black rectangles represent the contracted components. The number of components of one red circle corresponds to D.

which is extended from (3.23). The graphical representation of (3.23) is shown as Fig.3.10, and we can see the maximum value of the memory cost is D^6. From discus-

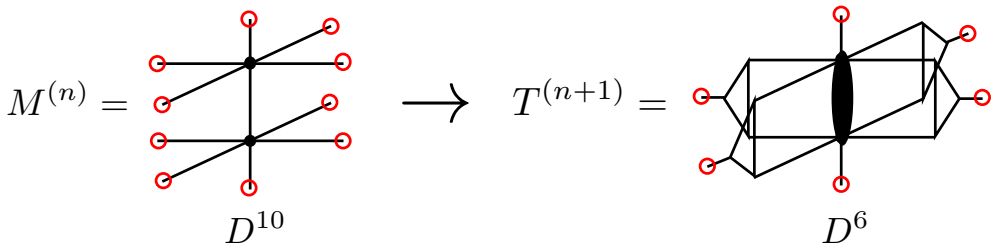

FIGURE 3.10: Graphical representation of memory cost of performing a projection.

sion of (1) and (2), the bottleneck of consumption of memory is construction of $M^{(n)}$ whose memory cost is D^{10}.

3.2.2 Order of contraction to lower the memory costs

By changing the order of contractions, we can avoid the large amount of memory consumption that occurs in the construction of $M^{(n)}$. As in Sec.3.2.1, we show the new algorithms for steps (1) and (2) respectively.

(1) The goal of this step is to construct $M^{(n)}_{z-x}$ to get the projectors. $M^{(n)}_{z-x}$ consists of a graph of two $M^{(n)}$ overlapped on each other, as shown in the right panel of the Fig.3.9. However, the initial construction of $M^{(n)}$ consumes a large memory D^{10}. Therefore, we construct the overlapped local tensor which is a half part of $M^{(n)}_{z-x}$ at first shown as Fig.3.11. This mathematical expression is

$$(m^{(n)}_{z-x})_{l_1 l_2 d_1 d_2} = \sum_{r,f,b,u} T^{(n)}_{l_1 r f b u d_1} T^{(n)}_{l_2 r f b u d_2}. \tag{3.24}$$

$M^{(n)}_{z-x}$ can be constructed by contracting upper and lower part:

$$(M^{(n)}_{z-x})_{LL'} := (M^{(n)}_{z-x})_{l_1 \otimes l_2, l'_1 \otimes l'_2} = \sum_{x_1,x_2} (m^{(n)}_{z-x})_{l_1 l_2 x_1 x_2} (m^{(n)}_{z-x})_{l'_1 l'_2 x_1 x_2}, \tag{3.25}$$

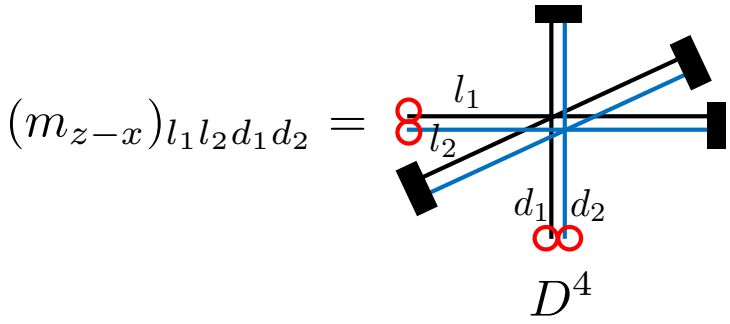

FIGURE 3.11: Graphical representation of half of $M^{(n)}_{z-x}$. This figure is the upper part of $M^{(n)}_{z-x}$, but the lower part can be constructed in the same way.

where the memory usage is D^4. As a result, the graphical representation of (3.25) is the same as the right figure in Fig.3.9. By taking the above steps, we can reduce the memory cost of obtaining $M^{(n)}_{z-x}$, or the projection, from D^{10} to D^4.

(2) The memory cost of constructing the projection operator could be reduced to D^4, but as shown in Fig.3.10, the memory cost required to perform the projection in the original process is still D^{10}. Therefore, we need to improve the projection algorithm in order to maximize the memory cost reduction in process (1). By changing the order of projection, we can reduce the memory cost to D^8 shown as Fig.3.12.

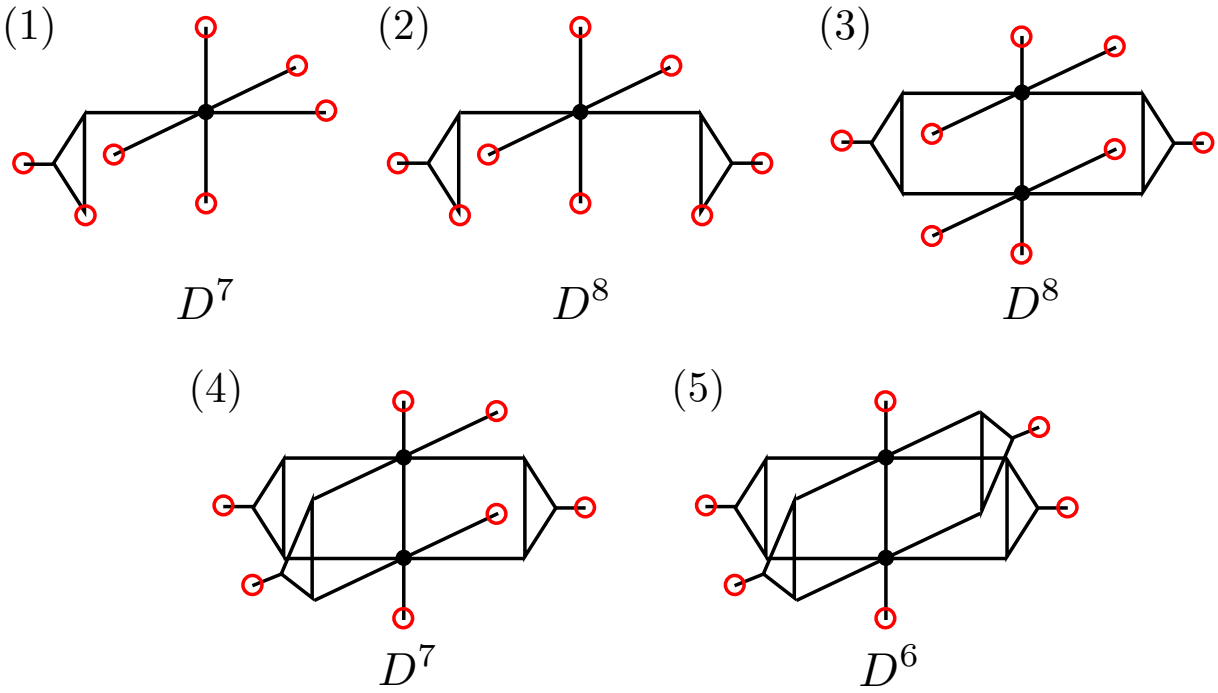

FIGURE 3.12: Order of the projection to reduce the memory cost.

By following steps (1) and (2), the memory usage limit of the entire process can be reduced to D^8, and memory can be saved in each process as well.

3.2.3 Double-leg parallel computation method

In Sec.3.2.2, we introduced an algorithm to reduce the maximum memory cost to D^8 by changing the order of contraction. However, the memory usage of D^8 is still too

large for high-precision analysis of critical behavior. In this section, we introduce a new parallel computation algorithm to significantly reduce the memory cost.

As we saw in Sec.3.2.2, the memory cost of step (1) is D^4, but the memory cost of step (2) is D^8, which is still large. Therefore, we developed a parallel computation method to distribute the two components that are not projected to different cores of the computer (called the *double-leg algorithm*). In the example of contraction in the z direction, the fifth (z) and sixth (z') components of $M^{(n)}_{XX'YY'zz'}$ in (3.21) have nothing to do with projection, so there is no problem storing these components separately. First, enumerate $M^{(n)}_{XX'YY'zz'}$ so that the components (z, z') are in the order of the dictionary expression like as $(1,1),(1,2),\cdots,(1,D),\cdots,(D,D)$, and define each as a new tensor $m^{(z,z')}_{XX'YY'}$:

$$m^{(z,z')}_{XX'YY'} = M^{(n)}_{XX'YY'zz'}. \tag{3.26}$$

Next, perform the projection to $M^{(z,z')}$ on different cores, respectively:

$$t^{(z,z')}_{xx'yy'} := \sum_{X,X',Y,Y'} U^{(n)}_{xX} U^{(n)}_{x'X'} V^{(n)}_{yY} V^{(n)}_{y'Y'} m^{(z,z')}_{XX'YY'}. \tag{3.27}$$

Finally, reconstruct the $T^{(n+1)}_{xx'yy'zz'}$ by collecting all $t^{(z,z')}_{xx'yy'}$, that is

$$T^{(n+1)}_{xx'yy'zz'} = t^{(z,z')}_{xx'yy'} \quad \text{for } z, z' = 1, \cdots, D. \tag{3.28}$$

The above process, including the details of the order of contraction and the memory cost, is illustrated using a figure shown as Fig.3.13. The maximum memory cost in the process of projection is reduced to D^7 from D^8.

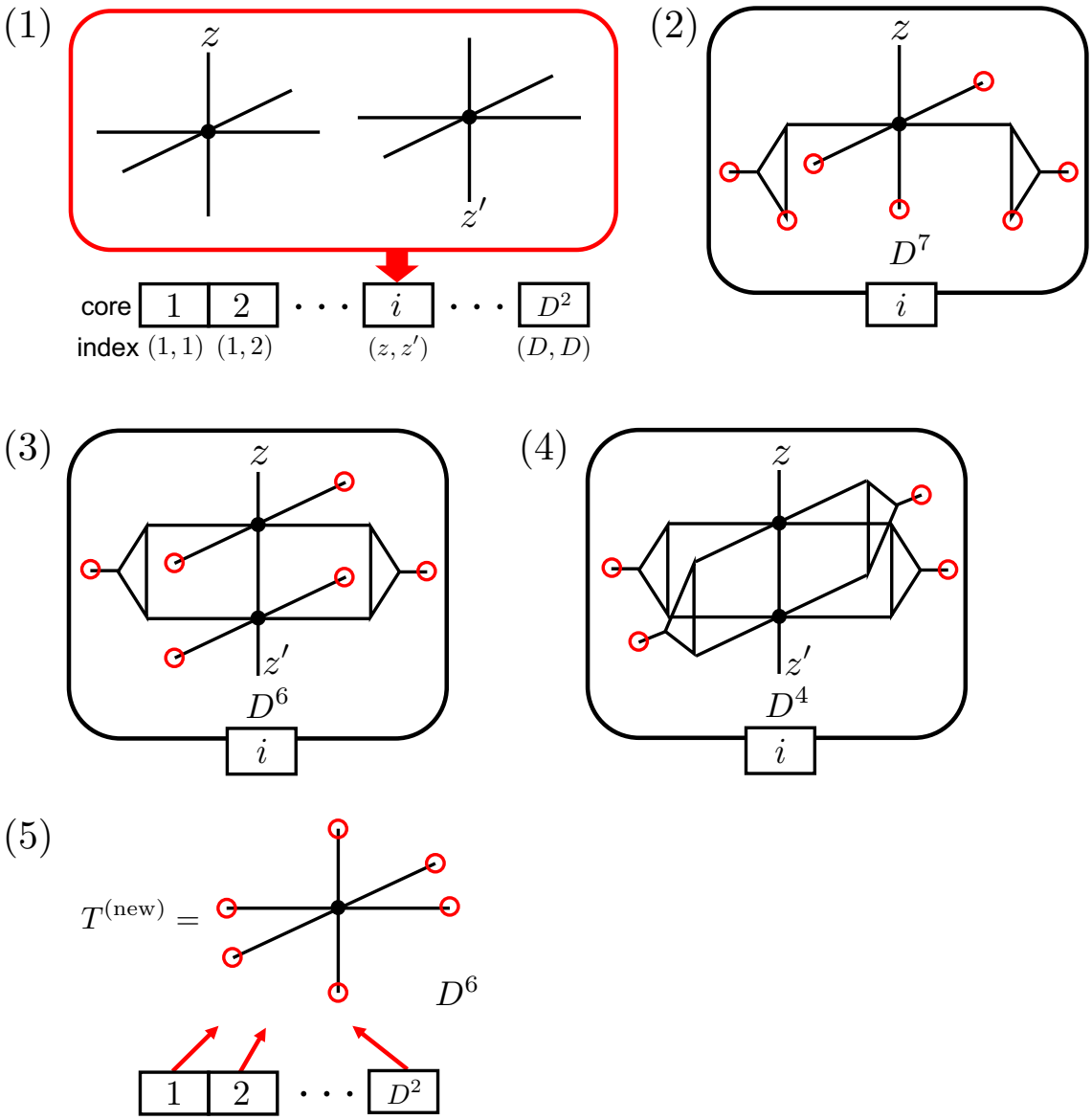

FIGURE 3.13: Graphical representation of the double-leg parallel computation algorithm. (1) Distribute the components in two direction of local tensors to different cores of the computer. (2-4) Perform projections in order of the algorithm introduced in Sec.3.2.2. (5) Collect all the components of the truncated tensor of each core to build a new renormalized tensor.

3.3 Density matrix renormalization group (DMRG)

In this section, we describe density renormalization group (DMRG) as an another numerical tool[47, 48, 80]. DMRG is a predecessor tool of tensor network methods, and is a powerful tool to analyze one-dimensional quantum systems and two-dimensional classical systems. We use DMRG for 2D MDM to calculate high accuracy and compare it with the accuracy of HOTRG.

3.3.1 Basic algorithm

DMRG for transfer-matrix diagonalizaton is based on the power method for obtaining the largest-eigenvalue eigenvector of a matrix.

First, we represent the partition function as a trace of local tensors as a tensor network:

$$Z_{M,N} = \mathrm{Tr}\{T^{N\times M}\}, \tag{3.29}$$

where M and N denote the number of lattice sites in the vertical and horizontal directions, respectively. In terms of a single matrix $\mathcal{T}$, called the transfer matrix, $Z_{M,N}$ in the limit of $M \to \infty$ is determined by the largest eigenvalue of $\mathcal{T}$. The largest-eigenvalue eigenstate $|\lambda_{\max}\rangle$ can be gotten by operating $\mathcal{T}$ many times to any state $|\lambda_0\rangle$ ($|\lambda_0\rangle$ must not be an orthogonal state to $|\lambda_{\max}\rangle$):

$$|\lambda_{\max}\rangle \propto \mathcal{T}^M |\lambda_0\rangle \ \ (M \to \infty). \tag{3.30}$$

In the case of MDM, the transfer matrix is defined as

$$\mathcal{T}_{\{\sigma'\}\{\sigma\}} = \sum_{\nu_1,\nu_2,\cdots,\nu_N,\nu_{N+1}} \prod_{i=1}^{N} T_{\nu_i\nu_{i+1}\sigma'_{i+1}\sigma_i}, \tag{3.31}$$

where $T_{\nu_i\nu_{i+1}\sigma'_{i+1}\sigma_i}$ is a local tensor of MDM in (3.3) (Fig.3.14).

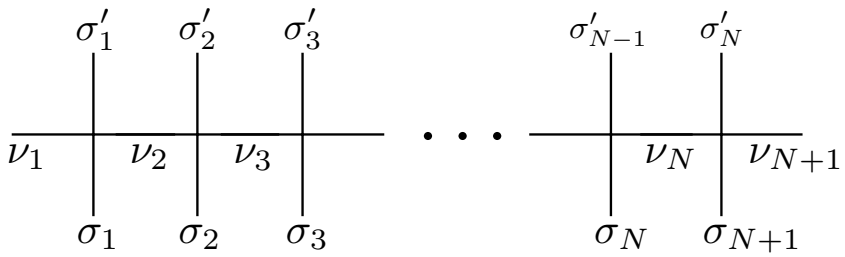

FIGURE 3.14: Graphical representation of the transfer matrix.

Next, we consider the thermodynamic limit $N, M \to \infty$. As the system expands, we must reduce the dimension of the matrix by selecting only the important bases of the transfer matrix to avoid an explosion in the number of basis. We describe the basis truncation algorithm as follows. Here, our discussion is restricted to the case of the real symmetric transfer matrix. The algorithm for the triangular lattice as an example of the non-symmetric transfer matrix is shown in Appendix A.2.

(1) Initial preparation of the maximum eigenstate.

Construct maximum eigenstate $\psi_{\max}$ of $\mathcal{T}$ in $2M_0$ system size by using exact diagonalization, where $2M_0$ should be small enough to be handled by the finite memory of the computer. The obtained state is denoted as $\psi_{\max}(\sigma_1, \sigma_2, \cdots, \sigma_{2M_0})$ and is shown in the graph in Fig.3.15. After constructing the maximum eigenstate, reserve the

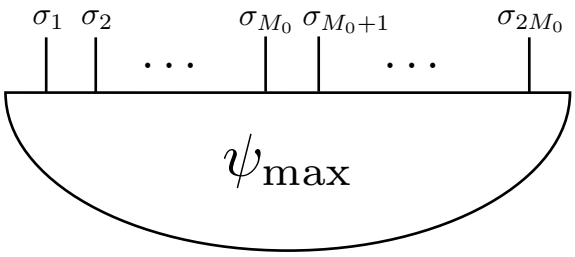

FIGURE 3.15: Maximum eigenstate of transfer matrix. Lines represent the components of the eigenstate.

important basis and discard the remaining basis. Divide the entire system in half and trace out the left(right) system to construct the density matrix (Fig.3.16):

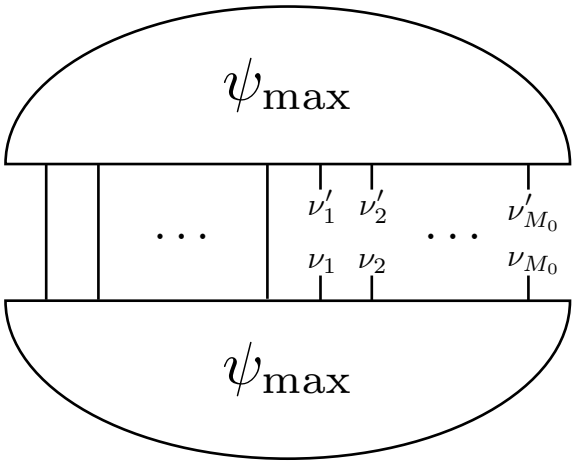

FIGURE 3.16: Density matrix for right half system.

$$\rho_{\text{right}}(\nu_1,\cdots,\nu_{M_0}|\nu'_1,\cdots,\nu'_{M_0}) = \sum_{\sigma_1,\sigma_2,\cdots,\sigma_{M_0}} \psi_{\max}(\sigma_1,\sigma_2,\cdots,\sigma_{M_0},\nu_1,\cdots,\nu_{M_0})\psi_{\max}(\sigma_1,\sigma_2,\cdots,\sigma_{M_0},\nu'_1,\cdots,\nu'_{M_0}). \tag{3.32}$$

Diagonalize the ρ_{right} and calculate the eigenvalues and eigenstates. Arrange the eigenstates in order of increasing eigenvalue as $\lambda_1 \geq \lambda_2 \geq \cdots \geq \lambda_m \geq \lambda_{m+1} \geq \cdots$ and reserve m basis $|\lambda_1\rangle, \cdots |\lambda_m\rangle$. We define these basis as *block basis*:

$$|\alpha\rangle = |\lambda_\alpha\rangle, \quad (\alpha = 1,\cdots,m). \tag{3.33}$$

By doing the same for the left half of the system, we get the block base for the left half of the system.

This number of m controls the accuracy of the calculation. The finite bond dimension m gives an additional length scale, as does the finite size scaling, and the large-small relation between this and the finite size scaling is important[81] (details are given in Appendix B).

(2) Enlargement of the system.

Add the two lattice sites to the center of the entire system and update the transfer matrices. We denote the new right transfer matrix as

$$\mathcal{T}^{\nu}_{\text{right}}(\sigma',\alpha'|\sigma,\alpha), \tag{3.34}$$

where ν is the left component, σ and σ' are additional components, and α and α' are block basis of original system (Fig.3.17).

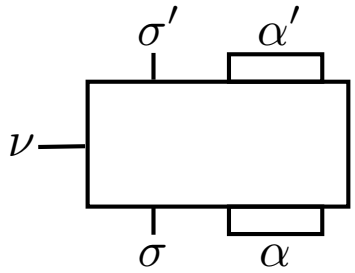

FIGURE 3.17: Transfer matrix for the right half system .

In the same way, the left transfer matrix can be constructed, and by combining the left and right matrices, a new entire transfer matrix can be constructed (Fig.3.18).

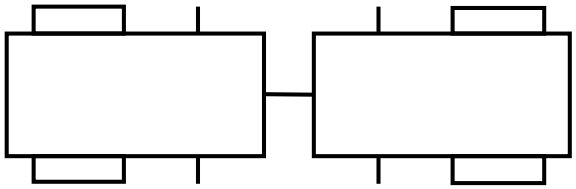

FIGURE 3.18: New transfer matrix for the entire system.

(3) The maximum eigenstate of enlarged system.
Diagonalize a new transfer matrix and get the maximum eigenstate $(\psi_{\max})_{\text{new}}(\alpha', \sigma', \sigma, \alpha)$ (Fig.3.19).

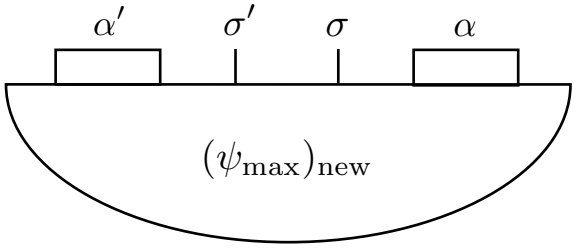

FIGURE 3.19: Maximum eigenstate of the new state.

Construct the density matrix of the half system using $(\psi_{\max})_{\text{new}}(\alpha', \sigma', \sigma, \alpha)$ and diagonalize it to get new block basis $\{|\beta\rangle\}$.

(4) Transformation matrix from the old basis $\{|\alpha\rangle\}$ to the new basis $\{|\beta\rangle\}$.
Transformation matrix for the right half of the system $A_R(\beta|\sigma, \alpha)$ can be defined as

$$|\beta\rangle = \sum_{\sigma,\alpha} A_R(\beta|\sigma, \alpha)\, |\sigma\rangle \otimes |\alpha\rangle\,. \tag{3.35}$$

This definition is the same for the left half of the system. These transformation matrices are shown as Fig.3.20.

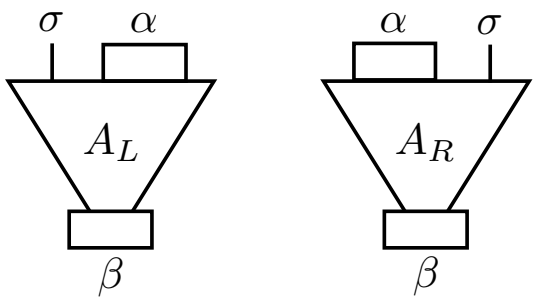

FIGURE 3.20: Transformation matrices from the old basis to the new basis.

Update the transfer matrix by letting the transformation matrix act on the old transfer matrix of half of the system (Fig.3.21).

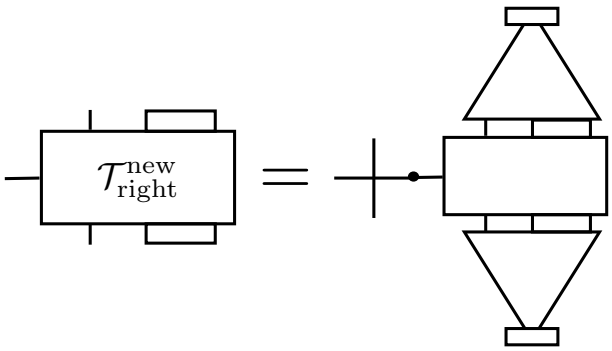

FIGURE 3.21: Update of the transfer matrix of the half of the system.

Iterate process of (2)∼(4) until the eigenstates converges.

3.3.2 Calculation of the expectation value

We introduce the method to calculate an expectation value. In DMRG terms the expectation value of local operatpr $\hat{O}$ is written as

$$\langle \hat{O} \rangle = \frac{\langle \psi_{\max} | \hat{O} | \psi_{\max} \rangle}{\langle \psi_{\max} | \psi_{\max} \rangle}, \tag{3.36}$$

where $|\psi_{\max}\rangle$ is the converged maximum eigenstate. The essence of the calculation is the same as in the case of HOTRG in Sec.3.1.2, and what we should do is to contract the local tensor with information about a local operator S_0 defined in (3.17) with the all local tensors except single site. At first, construct $|\psi_{\max}\rangle$ by the process in Sec.3.3.1. Next, add S_0 to the transfer matrix for the right half of the system and add the T_0 to the transfer matrix for the left half of the system in the process of update of the transfer matrix. Finally, combine the left and right matrices and sandwich them between $|\psi_{\max}\rangle$ (Fig.3.22).

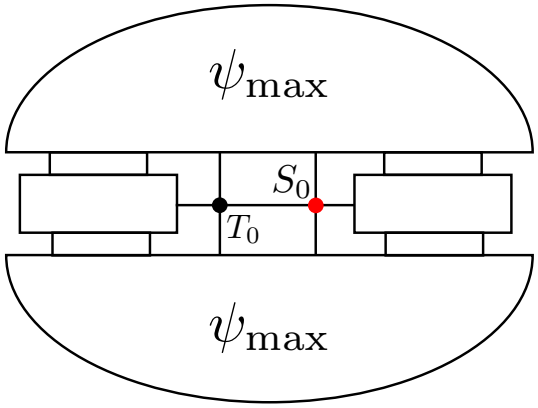

FIGURE 3.22: Graphical representation of the calculation of the expectation value by DMRG.

3.3.3 Calculation of the correlation length

Since the correlation length is expressed as the ratio of the largest eigenvalue of the transfer matrix to the second largest eigenvalue, it can be calculated by DMRG. These facts and the DMRG algorithm are explained below.

The correlation function for local operator $\hat{O}$ is defined as

$$\langle \hat{O}_i \hat{O}_j \rangle = \frac{\langle \Phi | \hat{O}_i \hat{O}_j | \Phi \rangle}{\langle \Phi | \Phi \rangle}, \tag{3.37}$$

where index i represents the site where $\hat{O}_i$ exists and we impose $j > i$. The denominator of (3.37) satisfies ,in the limit where the system size is large $M \to \infty$,

$$\langle \Phi | \Phi \rangle \sim \langle \psi_{\max} | \psi_{\max} \rangle = \lambda_{\max}^M. \tag{3.38}$$

On the other hand, denoting the local tensor at site i as $T^{[i]}$ and that with $\hat{O}_i$ as $T_O^{[i]}$, the numerator is transformed as follows:

$$\begin{aligned}
\langle \Phi | \hat{O}_i \hat{O}_j | \Phi \rangle &= \mathrm{Tr}\left[T^{[1]} T^{[2]} \cdots T^{[i-1]} T_O^{[i]} T^{[i+1]} \cdots T^{[j-1]} T_O^{[j]} T^{[j+1]} \cdots T^{[M]} \right] \\
&= \mathrm{Tr}\left[T_O^{[i]} T^{(j-i-1)} T_O^{[j]} T^{(M-j)-(i-1)} \right] \\
&= \sum_{\alpha,\beta,\gamma,\delta} \langle \psi_\alpha | T_O^{[i]} | \psi_\beta \rangle \langle \psi_\beta | T^{(j-i-1)} | \psi_\gamma \rangle \langle \psi_\gamma | T_O^{[j]} | \psi_\delta \rangle \langle \psi_\delta | T^{(M-j+i-1)} | \psi_\alpha \rangle \\
&= \sum_{\alpha,\beta} \langle \psi_\alpha | T_O^{[i]} | \psi_\beta \rangle \lambda_\beta^{(j-i-1)} \langle \psi_\beta | T_O^{[j]} | \psi_\alpha \rangle \lambda_\alpha^{(M-j+i-1)}.
\end{aligned} \tag{3.39}$$

Therefore,

$$\begin{aligned}
\frac{\langle\Phi|\hat{O}_i\hat{O}_j|\Phi\rangle}{\langle\Phi|\Phi\rangle} &= \sum_{\alpha,\beta} \frac{\langle\psi_\alpha|T_O^{[i]}|\psi_\beta\rangle}{\lambda_{\max}} \left(\frac{\lambda_\beta}{\lambda_{\max}}\right)^{j-i-1} \frac{\langle\psi_\beta|T_O^{[j]}|\psi_\alpha\rangle}{\lambda_{\max}} \left(\frac{\lambda_\alpha}{\lambda_{\max}}\right)^{L-j+i-1} \\
&\to \sum_{\beta} \frac{\langle\psi_\alpha|T_O^{[i]}|\psi_\beta\rangle}{\lambda_{\max}} \tilde{\lambda}_\beta^{j=i-1} \frac{\langle\psi_\beta|T_O^{[j]}|\psi_\alpha\rangle}{\lambda_{\max}} \cdot 1 \ (M\to\infty), \quad \tilde{\lambda}_i = \frac{\lambda_i}{\lambda_{\max}} \\
&= \frac{\langle\psi_{\max}|T_O^{[i]}|\psi_{\max}\rangle}{\lambda_{\max}} \cdot \frac{\langle\psi_{\max}|T_O^{[j]}|\psi_{\max}\rangle}{\lambda_{\max}} + \sum_{\beta<\max} \frac{\langle\psi_{\max}|T_O^{[i]}|\psi_\beta\rangle}{\lambda_{\max}} \cdot \frac{\langle\psi_\beta|T_O^{[j]}|\psi_{\max}\rangle}{\lambda_{\max}} (\tilde{\lambda}_\beta)^{j-i-1} \\
&=: \langle\hat{O}_i\rangle\langle\hat{O}_j\rangle + \sum_{\beta<\max} c_\beta(\tilde{\lambda}_\beta)^r, \qquad (3.40)
\end{aligned}$$

where $r = j - i - 1$ represents the distance between site i and j, and c_β is the factor in front of $\tilde{\lambda}_\beta$ in the summation. So, the connected correlation function at large r is determined by the ratio of the largest eigenvalue of the transfer matrix to the second largest eigenvalue $\tilde{\lambda}_{\max-1}$ as

$$\begin{aligned}
\langle\hat{O}_i\hat{O}_j\rangle_c &= \langle\hat{O}_i\hat{O}_j\rangle - \langle\hat{O}_i\rangle\langle\hat{O}_j\rangle \\
&= \sum_{\beta<\max} c_\beta(\tilde{\lambda}_\beta)^r \\
&\to c_{\max-1}(\tilde{\lambda}_{\max-1})^r \ (r\to\infty). \qquad (3.41)
\end{aligned}$$

If we define the correlation length ξ by assuming following exponential form except constant factor:

$$\langle\hat{O}_i\hat{O}_j\rangle_c \sim \exp\left(-\frac{r}{\xi}\right), \qquad (3.42)$$

ξ can be written as

$$\xi = -\frac{1}{\log\tilde{\lambda}_{\max-1}}. \qquad (3.43)$$

Since DMRG is based on the power law, we can obtain the second largest eigenvalue and use the relation (3.43) to calculate the correlation length. At first, construct the converged transfer matrix $\mathcal{T}_{\mathrm{FP}}$ at fixed point by the process in Sec.3.3.1. If we operate $\mathcal{T}_{\mathrm{FP}}$ to any state $|\psi_0\rangle$, $|\psi_0\rangle$ approaches $|\psi_{\max}\rangle$ slightly. Then, subtracting the direction of $\mathcal{T}_{\mathrm{FP}}|\psi_0\rangle$ from $|\psi_0\rangle$, and operating $\mathcal{T}_{\mathrm{FP}}$ to them, the remaining state approaches second largest eigenstate. These process is represented as a following calculation. The subtracted state is

$$|\delta\psi\rangle = |\psi_0\rangle - (\langle\psi_0|\psi_1\rangle)|\psi_1\rangle, \quad |\psi_1\rangle = \mathcal{T}_{\mathrm{FP}}|\psi_0\rangle, \qquad (3.44)$$

and $\mathcal{T}_{\mathrm{FP}}|\delta\psi\rangle$ is the state that is approaching the second largest eigenstate. By repeating the above process until $|\delta\psi\rangle$ converges, the second largest eigenstate is obtained.

Chapter 4

Critical behavior of the monomer-dimer model on two-dimensional lattices

The role of monomers in MDM is similar to the role of magnetic fields in Ising model, as discussed in Ref.[31]. In Ising model at critical temperature, the criticality is reflected in the dependence of magnetization on magnetic fields1.8. From the analogy with Ising model, we can assume that the criticality is reflected in physical quantities related to the monomer, such as the monomer density in MDM. In this chapter, we propose a critical behavior of monomer density, confirm that this form is correct, and determine the critical exponent numerically. With the results, we discuss the relationship and differences between Ising model and MDM in terms of critical behavior. We note that the dimension discussed in this chapter is restricted to two-dimension.

4.1 Our conjecture for the critical behavior of the monomer density

Our assertion is that the critical behavior of the monomer density is given as

$$\rho(z) \sim z^{1+\frac{1}{\delta}} \quad (z \sim 0). \tag{4.1}$$

δ is defined to play the same role as the critical exponent appearing in $m(h) \sim h^{\frac{1}{\delta}}$ of Ising model, that is, δ is related to the critical exponent of the correlation function η through the scaling relation:

$$\delta = \frac{d+2-\eta}{d-2+\eta}, \tag{4.2}$$

$$M(\boldsymbol{r}_i, \boldsymbol{r}_j) = \langle M(\boldsymbol{r}_i) M(\boldsymbol{r}_j) \rangle_c \sim |\boldsymbol{r}_i - \boldsymbol{r}_j|^{-(d-2+\eta)}, \tag{4.3}$$

where $M(\boldsymbol{r}_i)$ is a proper field introduced in (2.35) as the monomer creation operator. The form of (4.1) is predicted from following discussion focused on the determination of the proper field. We introduce the monomer occupation variable P_i with values of 0 and 1 corresponding to the case where the monomer occupies the site i or not. We note that P_i is not necessarily the same as $M(\boldsymbol{r}_i)$. Using P_i, the partition function can be represented as

$$\Xi(z) = \sum_{\{P\}} z^{\sum_k P_k} w(\{P\}), \tag{4.4}$$

where $w(\{P\})$ represents the number of ways to arrange dimers that satisfy the constraints by $\{P\}$, and the summation is taken over all possible case of P_k. $M(\boldsymbol{r}_i, \boldsymbol{r}_j)$ is defined as the ratio of the number of configurations with the two monomers to the number without them as (2.32). Therefore, by using $\{P_i\}$, $M(\boldsymbol{r}_i, \boldsymbol{r}_j)$ can be written as

$$M(\boldsymbol{r}_i, \boldsymbol{r}_j) = \frac{1}{\Xi(0)} w\left(P_i = 1, P_j = 1, P_k = 0 \ (k \neq i, j)\right). \tag{4.5}$$

On the other hand, the expectation value of $P_i/z \cdot P_j/z$ is

$$\begin{aligned}\left\langle \frac{P_i}{z} \cdot \frac{P_j}{z} \right\rangle &= \frac{1}{\Xi(z)} \sum_{\{P\}} \left(\frac{P_i}{z}\right)\left(\frac{P_j}{z}\right) z^{\sum_k P_k} w(\{P\}) \\ &= \frac{1}{\Xi(z)} \sum_{\{P\}} P_i P_j z^{\sum_{k\neq i,j} P_k} w(\{P\}).\end{aligned} \tag{4.6}$$

In the limit of $z \to 0$, since only $P_k = 0$ $(k \neq i, j)$ survives, the expression (4.6) matches the definition of $M(\boldsymbol{r}_i, \boldsymbol{r}_j)$ in (4.5). So proper field of monomer $M(\boldsymbol{r}_i)$ is identified as P_i/z. Comparing the scaling relation for magnetization in Ising model $\langle s(x)\rangle = m \sim h^{1/\delta}$ and identifying z as h, we get (4.1):

$$\langle M(\boldsymbol{r}_i)\rangle = \frac{\langle P_i\rangle}{z} = \frac{\rho(z)}{z} \sim z^{\frac{1}{\delta}}. \tag{4.7}$$

4.2 Numerical result

In this section, we verify that our conjecture of critical behavior of $\rho(z)$ (4.1) is correct or not numerically, and determine critical exponent δ. DMRG is a high-accuracy method in two-dimensional system, so we use not only HOTRG, but also DMRG. First, we compare the accuracy of HOTRG and DMRG using the exact solution of entropy at $z = 0$. As we will show in Sec.4.2.1, there is a slight difference between the numerical value of HOTRG and DMRG, and when compared to the exact solution, DMRG seems to be more accurate than HOTRG. So, we determine the critical properties by using DMRG as accurately as possible, while we also make calculations by HOTRG as a test to confirm whether HOTRG has enough accuracy to discuss the critical behavior of two or higher dimensional models. We note that the parallel computation method introduced in Sec.3.2 is not used for two-dimensional calculation in this section. As concrete examples, we will consider square and honeycomb lattices for critical systems, and triangular lattices for non-critical systems.

4.2.1 Calculation of the residual entropy

We calculate the residual entropy $\psi(0)$ defined as (2.5) by using HOTRG and DMRG (Table4.1). Here, the number of retained basis of HOTRG (bond dimension) D_{bond} defined in (3.10) is 40, and that of DMRG "m" defined in (3.33) is 400. From these results, DMRG is more accurate than HOTRG in both critical and non-critical cases. For DMRG, the accuracy in the non-critical system is much higher than that in the critical system, and the numerical results are very close to the exact solution. However, in HOTRG, the accuracy in a non-critical system is supposed to be higher than that in a critical system, but in reality, both are the same. This is because the required number of dimensions of the initial local tensor of a triangular lattice is larger than

that of a square lattice, and the effective number of retained bases of a triangular lattice is smaller (see Appendix A.1.2).

TABLE 4.1: The free energy at $z = 0$ from HOTRG and DMRG versus exact solutions shown in Table2.1. The calculations are done by HOTRG with $D = 40$, and DMRG with $m = 400$.

Geometry	Exact solution	DMRG	HOTRG
Critical system			
square	0.291560904030818...	0.29156042...	0.291599...
honeycomb	0.161532973609725...	0.161528...	0.161525...
Non-critical system			
triangular	0.428594537464958...	0.428594537464982...	0.428574...

4.2.2 Critical models

We analyze the dependence on z of the entropy and the monomer density in square and honeycomb lattice as critical systems. The entropy is shown in Fig.4.1. z-dependence is not linear, reflecting the criticality. At the level visible in the graph, the HOTRG and DMRG data are in agreement.

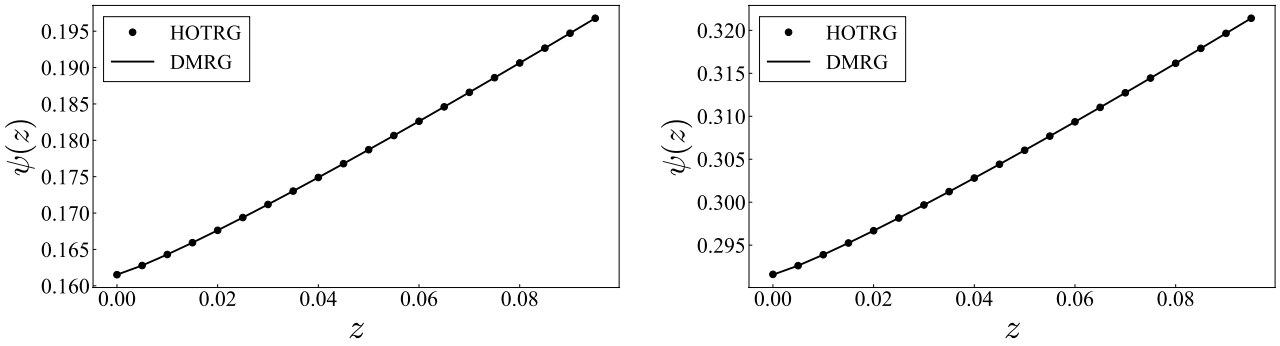

FIGURE 4.1: (Left) Entropy on the square lattice as a function of the monomer weight z. The plots are extracted from HOTRG, and DMRG method. In HOTRG the bond dimension is truncated at $D = 40$, and in DMRG the number of retained basis m is 200 (m is 400 only at $z = 0$). (Right) The same function is plotted for the honeycomb lattice.

Next, we discuss the behavior of the monomer density of the critical system. z-dependence of the monomer density calculated by DMRG based on the method in Sec.3.3.2 is shown in Fig.4.2. Since the monomer density is defined as the derivative of the entropy with respect to z as (2.8), it reflects criticality as well as entropy, and the z-dependence is not linear. To verify the critical behavior of $\rho(z)$ as (4.1) and determine the critical exponent δ, we take two different approaches.

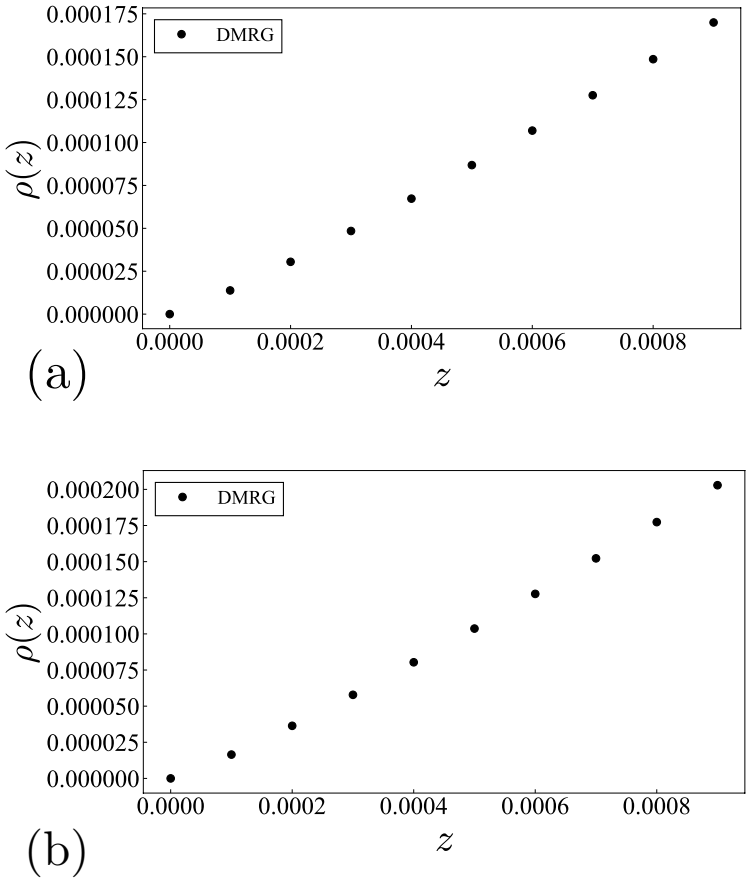

FIGURE 4.2: (a) Monomer density on the square lattice as a function of the monomer weight z. The plots are extracted from DMRG with $m = 200$ ($m = 400$ only at $z = 0$). (b) The same function is plotted for the honeycomb lattice.

(1) Fitting approach.
Taking logarithmic of both sides of (4.1), it becomes

$$\log\left(\frac{\rho(z)}{z}\right) \sim \frac{1}{\delta}\log z. \tag{4.8}$$

The plots of $\log(\rho(z)/z)$ about z are shown as an one-logarithmic graph Fig.4.3.

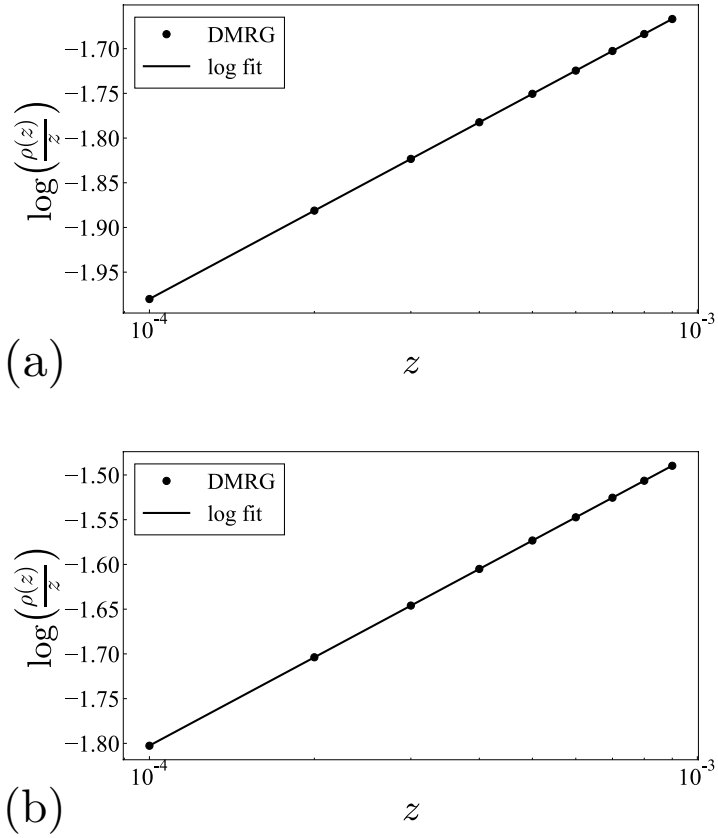

FIGURE 4.3: (a) The log of the monomer density over the monomer weight on the square lattice as a function of monomer weight z. The horizontal axis is log scale. (b) The same plots for the honeycomb lattice.

We can see that our assertion (4.1) is correct, as it is plotted on a straight line as shown in Fig.4.3. From the slope of fitting function, the critical exponent is read as $\delta = 7.014$ for the square lattice and 7.021 for the honeycomb lattice.
(2) Integral approach.
We also show another way of calculating the critical exponent using the exact solution of $z = 0$, which can avoid the low-precision point $z = 0$. Integrating (4.1) from 0 to z

$$\int_0^z dz' \frac{\rho(z')}{z'} = \psi(z) - \psi(0), \tag{4.9}$$

and the left hand side can be transformed as

$$\int_0^z dz' \frac{\rho(z')}{z'} \approx \frac{1}{1+\frac{1}{\delta}} z^{1+\frac{1}{\delta}} \sim \frac{1}{1+\frac{1}{\delta}} \rho(z) \tag{4.10}$$

near the $z = 0$. From (4.9) and (4.10),

$$\delta \approx \left[\frac{\rho(z)}{\psi(z) - \psi(0)} - 1 \right]^{-1}. \tag{4.11}$$

Therefore, using exact solutions (2.1) as $\psi(0)$ and numerical results as $\rho(z)$ and $\psi(z)$ in (4.11), the critical exponent can be determined more precisely. In this method, $\rho(z)$ and $\psi(z)$ are calculated by both HOTRG and DMRG. The results are shown in Table4.2 combining the result from method (1).

TABLE 4.2: (2) Critical exponent calculated using formula (4.11) from HOTRG and DMRG. In HOTRG the expectation value of monomer density at $z = 0.005$ with $D = 42$ is used, and in DMRG the value of at $z = 0.00002$ with $m = 400$ is used. (1) The data calculated by method (1).

Geometry	(2) HOTRG	(2) DMRG	(1) DMRG
square	7.000104...	7.00014...	7.014...
honeycomb	7.026...	7.00098...	7.021...

From above analysis, we conclude $\delta = 7$. On the other hand, the power-law behavior of the correlation function with critical exponent $\eta = 1/2$ has been calculated for the square lattice as (2.36). Our result $\delta = 7$ agrees with $\eta = 1/2$ if we assume scaling relation(4.2), so $\delta = 7$ is reasonable value. As in 1.1, since the critical exponents of the 2D Ising model is $\delta = 15$ and $\eta = 1/4$, MDM on square lattice and MDM on honeycomb lattice are classified into different criticality class from 2D Ising model. This may be attributed to the fact that the correspondence between the Ising model and the MDM is not for lattices of the same shape in terms of bipartiteness.

The value of η is also important for the mapping of MDM to the bosonic Gaussian theory to determine the coupling constant. Gaussian theory is classified as $c = 1$ CFT, and the value of central charge $c = 1$ is confirmed by analyzing the finite size effect[82]. By calculating the δ, we can further confirm the value of $\eta = 1/2$, and this result supports the discussion to conclude that $c = 1$ in Ref.[82].

4.2.3 Non-critical models

In this section, we consider the triangular lattice which is one of the non-critical lattice models. The entropy calculated from HOTRG and DMRG is shown as Fig.4.4, and the monomer density calculated from DMRG is shown as Fig.4.5. The linear dependence on z of the entropy and the monomer density are shown in Fig.4.4 and Fig.4.5, and these results reflect the non-criticality of MDM on triangular lattice.

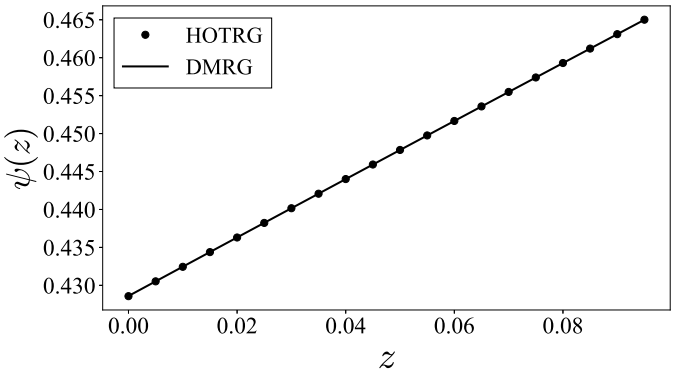

FIGURE 4.4: Entropy on the triangular lattice as a function of the monomer weight z. The plots are calculated from HOTRG with $D = 40$, and DMRG with $m = 200$.

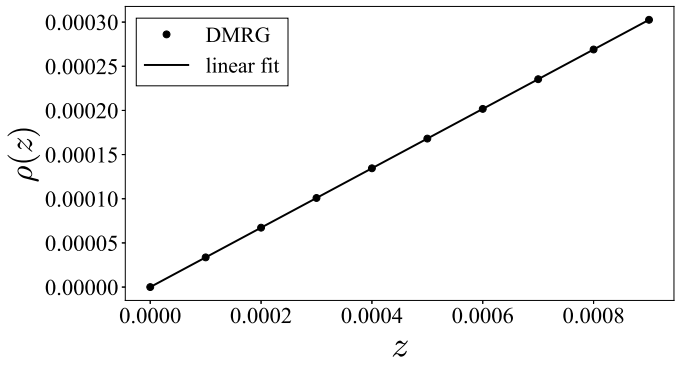

FIGURE 4.5: The monomer density on the triangular lattice as a function of monomer weight z, and the linear fitting for them. The plot is calculated from DMRG with $m = 200$ and their dependence on z is linear (m is 400 only at $z = 0$).

From the above calculations for the critical and non-critical models, it is found that the accuracy of HOTRG is close to that of DMRG in the calculation of thermodynamic quantities and critical exponents. This fact indicates that HOTRG may be effective in analyzing thermodynamic quantities and critical behaviors of three-dimensional systems.

4.3 Comparison with the Gaunt's conjecture

In 1969, Gaunt studied the behavior of monomer density near the critical point.[83]. Using the series expansion method introduced in Nagle[84] and the Padé approximation, they found that the monomer density has a common form in different lattices. They do not mention the critical exponent of monomer density and its universality class, but the resulting form can be compared with our results. In this section, we briefly review the Gaunt results and show that our numerical results are consistent with the Gaunt results. Note that to avoid confusion with the quantity of monomer, x represents the "dimer" activity and ρ_d represents the "dimer" density.

The grand partition function per-site in thermodynamic limit can be expanded for dimer activity x as

$$\Xi(x) = \lim_{N\to\infty} (\Xi_N(x))^{\frac{1}{N}} = 1 + \sum_{s=1}^{\infty} g_s x^s. \tag{4.12}$$

Determining the first few terms of (4.12) corresponds to the expansion for low dimer density. Gaunt uses the correspondence between MDM and Ising model with magnetic field to determine the coefficients $\{g_s\}$ for small s. By applying Padé approximation to $\{g_s\}$ for small s, the properties in the region of high dimer density can be obtained. According to above process, they get the asymptotic form near the critical point as

$$x = A\left(1 - \frac{\rho_d(x)}{\rho_d(\infty)}\right)^{-\gamma} \quad (x \to \infty), \tag{4.13}$$

where A is constant. Here, the $\rho_d(x)$ is defined as the number of sites occupied by dimers over the number of whole sites. Therefore, $\rho_d(\infty) = 1$ in (4.13). Gaunt computes the exponents γ numerically and conjectures γ as a rational number close to the numerical value (Table4.3).

TABLE 4.3: Values of exponent γ in (4.13) conjectured by Gaunt based on their numerical calculation[83]. Only the value of the honeycomb lattice is a conjecture and is not based on numerical calculations.

Geometry	square	honeycomb	triangular	cubic	bcc	fcc
γ	7/4	7/4	2	1.95	1.95	2

They also mention the possibility of the exponent γ being classified into some sort of lattice group. First, they classify lattices into two groups: loose-packed lattice and close-packed lattice. Loose-packed lattice is defined as a lattice containing only polygons with an even number of lines, while close-packed lattice is defined as a lattice containing polygons with an odd and even number of lines. Next, their prediction for γ is shown below. Two-dimensional loose-packed lattices such as square and honeycomb lattice have commonly have the value $\gamma = 7/4$. Three-dimensional loose-packed lattices such as cubic and bcc lattice have commonly have the value $\gamma = 1.95$. For loose-packed lattice, the values of γ are commonly determined depending on the dimension of the lattice. On the other hand, close-packed lattices have commonly have the value $\gamma = 2$ not depending on the dimension of the lattice.

Finally, we compare the our assertion of critical behavior (4.1) and the numerical results for critical exponent δ with Gaunt's work. The relationship between dimer activity x and monomer activity z is

$$z = x^{-\frac{1}{2}}, \tag{4.14}$$

and the relationship between dimer density $\rho_d(x)$ and monomer density $\rho(z)$ is

$$\rho(z) = 1 - \rho_d(x(z)). \tag{4.15}$$

By using (4.14) and (4.15), (4.13) can be represented in terms of the quantity of monomer:

$$\rho(z) = \left(\frac{z}{\sqrt{A}}\right)^{\frac{2}{\gamma}} \sim z^{\frac{2}{\gamma}} \quad (z \to 0). \tag{4.16}$$

This form is the same as (4.1), and the relationship between γ and δ is given as

$$\gamma = \frac{2}{1 + \frac{1}{\delta}}. \tag{4.17}$$

Applying our numerical results to the Eq.(4.17), we obtain $\gamma = 7/4$ from $\delta = 7$ for square and honeycomb lattice, and $\gamma = 2$ from $\delta = \infty$ for triangular lattice. The values of γ obtained by this correspondence are matched Gaunt's results in Table4.3, and thus our numerical results strongly support their conjecture.

We suggest the new conjecture about two-dimensional MDM as a updated version of Gaunt's argument (4.13) as follows:

$$\rho(z) \sim \begin{cases} z^{1+\frac{1}{\delta}}, & \delta = 7 \quad \text{(bipartite lattice)}, \\ z & \text{(non-bipartite lattice)}. \end{cases} \tag{4.18}$$

Bipartite and non-bipartite are definitions that are similar in meaning to loose-packed lattices and close-packed lattices, respectively. There are some papers on the relationship between bipartiteness and criticality in MDM, such as [29, 61], but our argument

(4.18) is new in that it mentions even the universality class.

4.4 Correspondence of the monomer density in the Ising model

Ref.[31] states that there is a correspondence relation between the monomer in MDM and the magnetic field. However, critical behavior of magnetization at $T = T_c$ is $m(h) \sim h^{\frac{1}{\delta}}$, and our result for the monomer density is $\rho(z) \sim z^{1+\frac{1}{\delta}}$, so the two forms do not match. Therefore, we investigate the counterparts of the monomer density in the Ising model, where the form of the exponent is $1+\frac{1}{\delta}$ at $T = T_c$. Heilmann and Lieb used the high-temperature expansion for Ising model with magnetic fields to prove the correspondence between the partition function in MDM and the partition function in Ising model with magnetic fields[31]. We will also peform the high-temperature expansion for Ising model with field using some part of their discussion, and show that the "odd vertex density" corresponds to the monomer density. We denote Ising model with fields as Ising model simply throughout this section.

4.4.1 High-temperature expansion of the Ising model with magnetic fields

The partition function for Ising model is

$$Z_N = \sum_{\{\sigma\}} e^{-\beta\mathcal{H}} \tag{4.19}$$

$$\beta\mathcal{H} = -\beta J \sum_{<i,j>} \sigma_i\sigma_j - \beta h \sum_i \sigma_i. \tag{4.20}$$

Z_N can be expanded for β as

$$Z_N = (\cosh\beta J)^{N_B}(\cosh\beta h)^N \sum_\sigma \prod_{<i,j>} (1 + v\sigma_i\sigma_j) \prod_k (1 + z\sigma_k), \tag{4.21}$$

where where N and N_B are the number of sites and edges, and $v = \tanh\beta J, z = \tanh\beta h$. In the summation in (4.21), only terms with an even number of spins on each site survive shown as Fig.4.6 (a, b). We call the contributing vertices that have odd number of bonds such as Fig4.6 (b) "odd vertex". Thus, the contributing term is

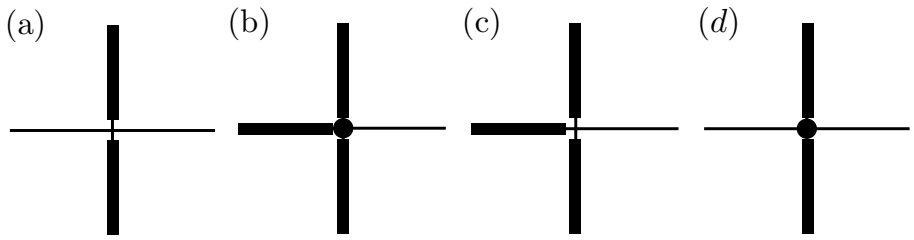

FIGURE 4.6: Diagram of the vertices that can contribute to the terms included in the high-temperature expansion. A round symbol represents the magnetic field at a site, and a rod-shaped symbol represents the magnetic field between adjacent sites. (a) and (b) are examples of contributing vertices, while (c) and (d) are examples of non-contributing vertices.

represented as a diagram consisting only of vertices with even spins and characterized

by a pair (n, l) of vertex and bond numbers (Fig.4.7). Introducing the number of

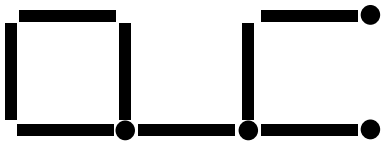

FIGURE 4.7: An example of diagram characterized by $(n, l) = (4, 8)$.

diagrams with (n, l) notated as $W_{n,l}$, Z_N can be transformed to

$$Z_N = (\cosh \beta J)^{N_B} (\cosh \beta h)^N S_N, \tag{4.22}$$

$$S_N = \sum_{n,l} z^n v^l W_{n,l}. \tag{4.23}$$

4.4.2 The correspondence between the odd vertex density and the monomer density

In high-temperature expansion of Ising model, we define odd vertex density $\rho_{\text{odd}}(z)$ as the number density of the odd vertices:

$$\rho_{\text{odd}}(z) = \frac{1}{N} S_N^{-1} \left(\sum_{n,l} n z^n v^l W_{n,l} \right). \tag{4.24}$$

We show that the form of critical behavior of $\rho_{\text{odd}}(z)$ near $z = 0$ at $T = T_c$ is the same as that of the monomer density (4.1) by using the critical behavior of magnetization $m(h) \sim h^{\frac{1}{\delta}}$ (of course, δ is not the same value). By using (4.24), the magnetization is represented as follows:

$$\begin{aligned} m &= \frac{1}{N} \frac{\partial}{\partial(\beta J)} \log Z_N \\ &= z + \frac{1}{N} \frac{\partial}{\partial(\beta J)} \log S_N \\ &= z + \frac{dz}{d(\beta J)} \frac{1}{z} \frac{1}{N} \left(\sum_{n,l} n z^n v^l W_{n,l} \right) \\ &= z + \frac{1}{\cosh \beta J \sinh \beta J} \rho_{\text{odd}(z)} \end{aligned} \tag{4.25}$$

Therefore, $\rho_{\text{odd}}(z)$ is represented as

$$\begin{aligned} \rho_{\text{odd}}(z) &= \cosh \beta J \sinh \beta J \cdot (m - z) \\ &\sim z(z^{\frac{1}{\delta}} - z) \sim z^{1+\frac{1}{\delta}}, \end{aligned} \tag{4.26}$$

where in the last line of the transformation, we use $m(h) \sim h^{\frac{1}{\delta}} \sim z^{\frac{1}{\delta}}$ and $\cosh \beta J \sim 1$ $(z \to 0)$. (4.26) is the same form as the critical behavior of the monomer density (4.1).

Finally, we show the numerical calculation of the critical behavior of $\rho_{\text{odd}}(z)$ by DMRG to confirm (4.26). In high-temperature expansion, the partition function is represented as a combination of the graph consisting vertices with weight z and bonds with weight v. So, the local tensor of Ising model with high-temperature expansion

can be constructed by extending the case of MDM:

$$T_{ijkl}^{(\mathrm{Ising})} = \begin{cases} 1 \quad \text{if } i=j=k=l=0; \\ z \cdot v \quad \text{if only one index is 1;} \\ v^2 \quad \text{if two indices are1 , and the other two are 0} \\ z \cdot v^3 \quad \text{if only one index is 0;} \\ v^4 \quad \text{if } i=j=k=l=1, \end{cases} \tag{4.27}$$

where the index "1" means that the vertex has a bond, and weight z is multiplied if the vertex has an odd number of bonds. The plots of $\log(\rho_{\mathrm{odd}}(z)/z)$ about z are shown as an one-logarithmic graph Fig.4.8. The linear dependence on z in Fig.4.8 indicates

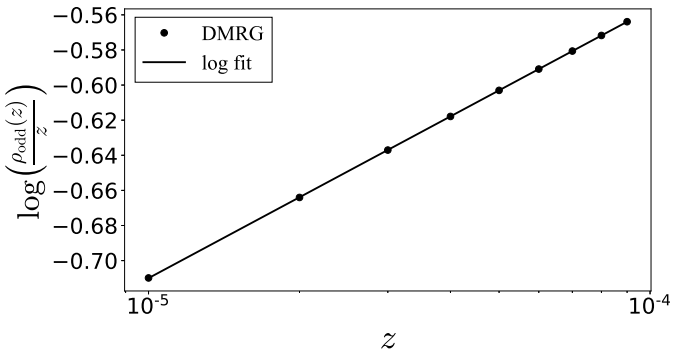

FIGURE 4.8: The log of the odd vertex density over the z on the square lattice as a function of z. The horizontal axis is log scale, and the plots are calculated by DMRG with $m = 150$.

that the form (4.26) is correct. From the slope of fitting linear function, the critical exponent is read as $\delta = 15.04$ and its value matches the exact value of Ising model shown in Table1.1. We again conclude that the role of monomers in monomer-dimer model is similar to the role of magnetization in Ising model, but that the models do not correspond in terms of critical properties.

Chapter 5

Critical behavior of the monomer-dimer model on multilayer lattices

In this chapter, we consider MDM on the multilayer lattices. Although multilayer lattices belong to a three-dimensional system, a numerical framework for two-dimensional is possible when the number of layers is small. In this sense, a series of multilayer models serves as a bridge between two and three dimensions. Not only that, but each multilayer model shows the properties specific to the layered structures. For the two- and three-layer models, we will perform numerical analysis using DMRG. On the other hand, for the multilayer model, we construct a bosonic field theory as an extension from 2D. For the two-layer model, numerical analysis is also performed by varying the interlayer dimer activity.

5.1 Critical behavior of multilayer bipartite lattice models

We consider the case where the constituent layers are a bipartite lattice such as a square lattice or a honeycomb lattice. In this case, the whole system is also bipartite lattice. From the insights of two-dimensional MDM, we can propose some simple hypothesis about critical properties of multilayer bipartite models.

(A) Multilayer bipartite models are critical because of their bipartiteness.

(B) The multilayer bipartite model is non-critical, because the interlayer dimers can be regarded as monomers on each layer plane as shown in Fig.5.1, and the dimer system with monomers is non-critical. Therefore, z-dependence of monomer density is expected to be linear.

FIGURE 5.1: Schematic representation of the correspondence between a two-layer PDM and two 2D MDMs.

The conclusion is that neither hypothesis is correct. To be precise, the critical properties are not common to each multilayer model, at least not to the two- and three-layer models. There are unique properties of the layered structure that cannot be explained by two-dimensional knowledge alone. We show such properties by analyzing two- and three-layer bipartite lattice models.

5.1.1 Two-layer models

We study MDM on square and honeycomb two-layer lattices by DMRG (Fig.5.2).

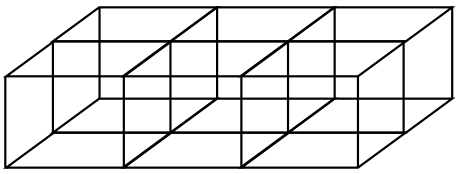

FIGURE 5.2: Two-layer lattice in which the constituent layers are square in shape.

In order to treat the two-layer model as a two-dimensional system, the local tensors defined in each layer are contracted in the vertical direction of the layer to construct a compressed initial local tensor. The construction of the local tensor is illustrated with an example of a square layer lattice. This method is the same for honeycomb layer lattices and other layer lattices, so the details are omitted. The procedure is as follows.
(1) Define the local tensor on the constituent layers (Fig.5.3). The components of the

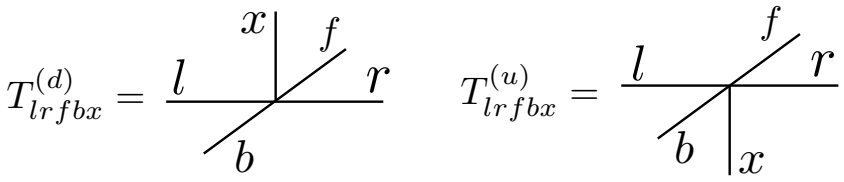

FIGURE 5.3: Local tensor for each constituent layer. $T^{(d)}$ and $T^{(u)}$ represent the local tensors on the lower and upper lattices, respectively.

local tensor in the planar direction are the same as in the 2D case, but one component is added for the vertical edges because of the presence of dimers:

$$T^{(d)}_{lrfbx} = \begin{cases} z & \text{if } l=r=f=b=x=0; \\ 1 & \text{if only one index is 1;} \\ 0 & \text{otherwise,} \end{cases} \qquad T^{(u)}_{lrfbx} = \begin{cases} z & \text{if } l=r=f=b=x=0; \\ 1 & \text{if only one index is 1;} \\ 0 & \text{otherwise,} \end{cases} \tag{5.1}$$

where the fifth index represents the upper (lower) direction of the lower (upper) layer.
(2) Compress the upper and lower local tensors (Fig.5.4):

$$T^{(\text{2layer})}_{LRFB} = \sum_{x} T^{(d)}_{l_1 r_1 f_1 b_1 x} T^{(u)}_{l_2 r_2 f_2 b_2 x}, \tag{5.2}$$

where large letter on the left side represents the tensor product of the indices of each tensor on the right side, e.g. $L = l_1 \otimes l_2$.

We show the numerical results of the entropy and the monomer density calculated by DMRG using local tensor $T^{(\text{2layer})}_{LRFB}$. The entropy of square layer model and honeycomb layer model is shown as Fig.5.5, where the curvilinear behavior can be seen.

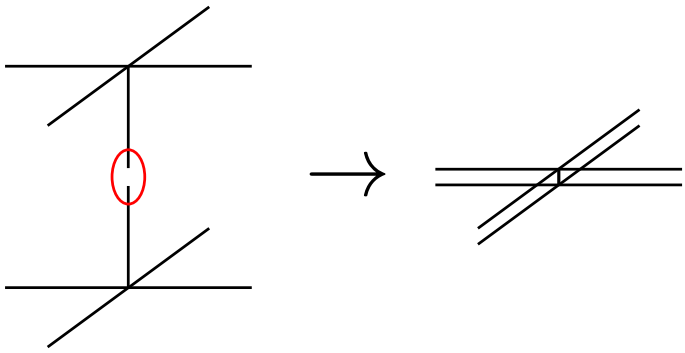

FIGURE 5.4: Compression of the upper and lower local tensors.

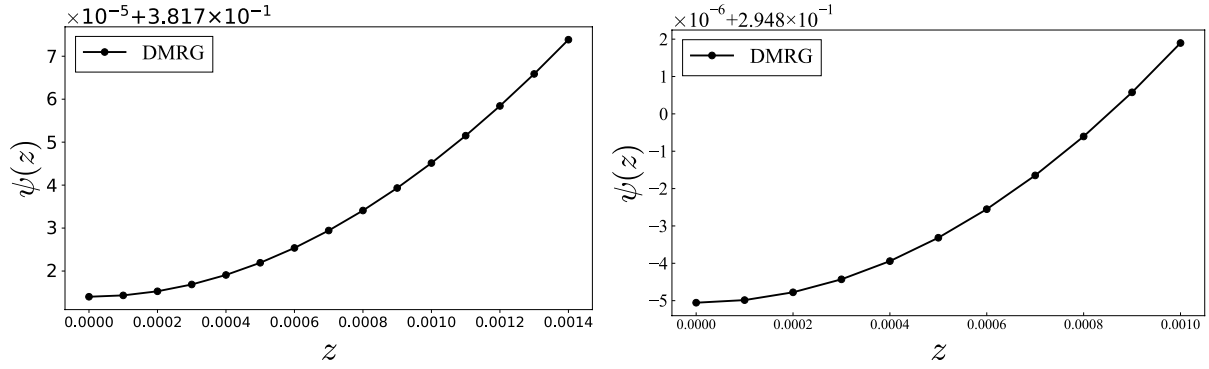

FIGURE 5.5: (Left) Entropy of square layer model as a function of the monomer weight z. The plot is computed by DMRG with $m = 200$. (Right) The same function is plotted for honeycomb layer model.

A similar curvilinear behavior can be seen for the monomer density shown in Fig.5.6. From the plots in Fig.5.6, z-dependence of the monomer density near $z = 0$ is $\rho(z) \sim z^2$. To investigate the detail behavior near $z = 0$, we show the graph of $\rho(z)/z^2$ in Fig.5.7. From Fig.5.7, the slope approaches the constant value as z approaches zero. Therefore, the relation $\rho(z) \sim z^2$ is considered to be valid in the vicinity of $z = 0$. According to the dependence of powers of an integer of the monomer density, two-layer bipartite models are considered to be non-critical.

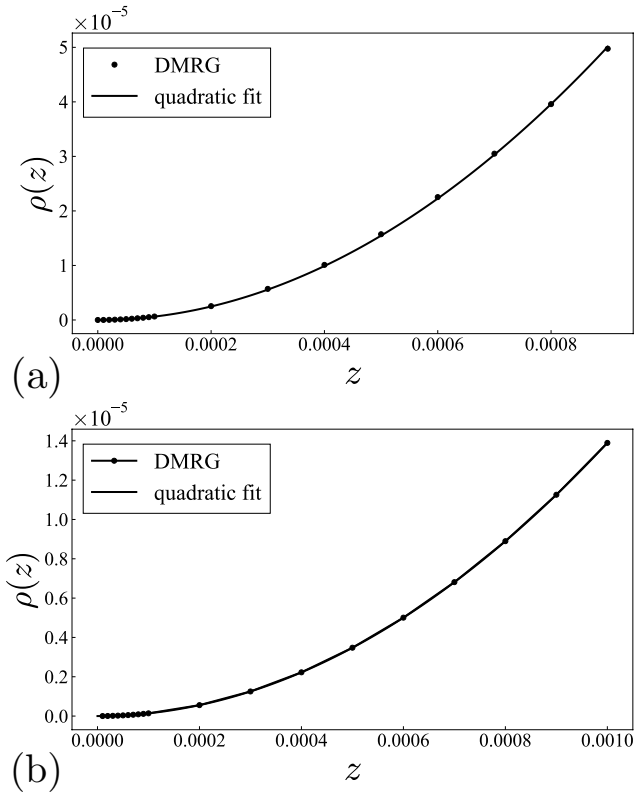

FIGURE 5.6: (a) Monomer density of the square layer model as a function of the monomer weight z. The plot is computed by DMRG calculations, using base numbers of $m = 500$ for $z \leq 9.0 \times 10^{-5}$ and $m = 200$ for $z > 9.0 \times 10^{-5}$. The line represents a fitting function of the form Az^2. (b) The same functions are plotted for the honeycomb layer model.

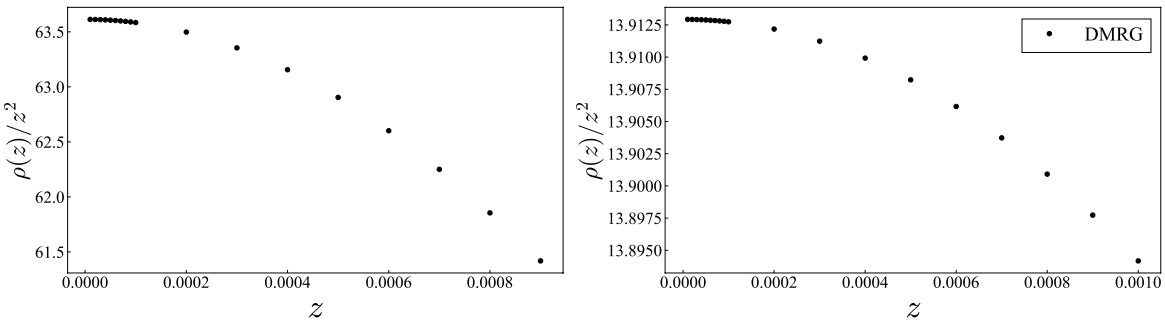

FIGURE 5.7: (Left) Monomer density over z^2 of the square layer model. (b) The same function for the honeycomb layer model.

We show the correlation length data of the monomer-monomer correlation function as a supplementary evidence of non-criticality in Fig.5.8. Fig.5.8 shows that ξ^{-1} approaches a non-zero value as z approaches 0, i.e., ξ^{-1} is not diverge at $z = 0$. On the other hand, Fig.5.9 shows that ξ^{-1} approaches 0 at $z = 0$ (ξ diverges at $z = 0$) in two-dimensional square lattice that is classified as a critical system. Even by comparing the behavior of the correlation length of the two-layer bipartite lattice with that of square lattice, the two-layer bipartite model considered to be non-critical and this result is consistent with Ref.[63].

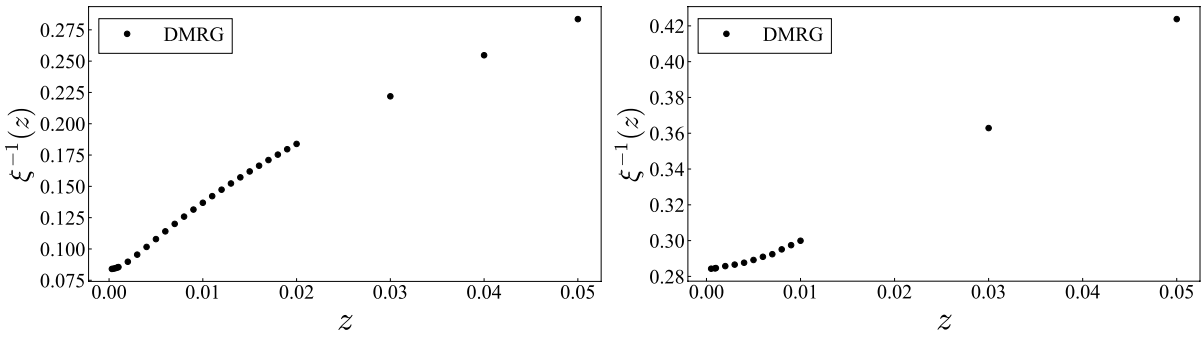

FIGURE 5.8: (Left) z-dependence of inverse of correlation length of the square layer model calculated from DMRG with $m = 200$ by the method introduced in Sec.3.3.3. (b) The same functions are plotted for the honeycomb layer model.

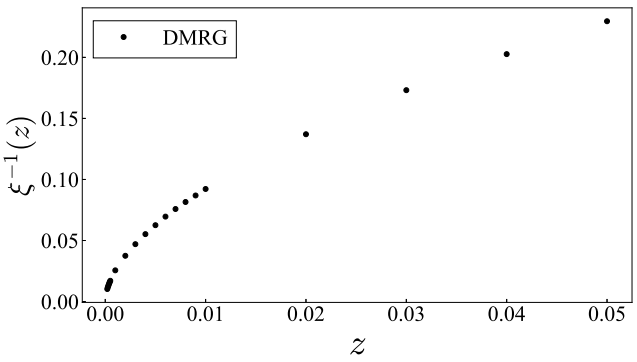

FIGURE 5.9: z-dependence of inverse of the correlation length of the two-dimensional square model.

In summary, in the two-layer bipartite model, $\rho(z) \sim z^2 (z \sim 0)$ and this model is non-critical. This result does not apply to either hypothesis (A) or (B) above for the following two aspects:

- In spite of the bipartiteness, the two-layer bipartite model is non-critical.
- z-dependence of $\rho(z)$ is not linear but z^2.

As an illustration of these properties, we propose that PDM on the the two-layer lattice can be identified as a system of two stacked MDMs on a two-dimensional lattice. The mapping from PDM to MDM comes from the fact that the interlayer dimers are recognized as two monomers on each layer. Based on this hypothesis, the non-criticality of PDM on a two-layer lattice is due to the fact that it is essentially MDM. Therefore, unlike the Ising model[85], the extension from two dimensions to two layers essentially change the critical properties of PDM. On the other hand, the z^2 dependence of $\rho(z)$ represents the confinement of monomers such that the monomers exist in pairs, and the confinement is due to the inherited properties of two-dimensional square and honeycomb lattices. These properties suggest that the two-layer model strongly inherits the lattice properties of the 2D constituent layers.

5.1.2 Three-layer models

In this section, MDM on square and honeycomb three-layer lattices (Fig.5.10). The three-layer model is a simple extension of the two-layer model system, but the three-layer system exhibits a completely different behavior of thermodynamic quantities than the two-layer system.

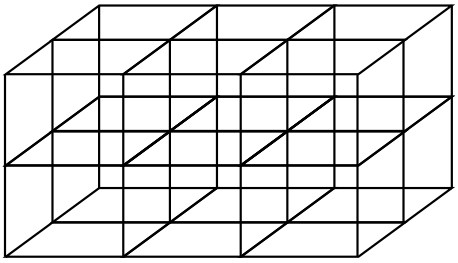

FIGURE 5.10: Three-layer lattice in which the constituent layers are square in shape.

Construction of the local tensor of square three-layer model is performed in the same way as the two-layer model. The process of compression of the local tensor from three-layer to two-dimensions is as follows.
(1) Define the local tensor on the constituent layers (Fig.5.11). The local tensors on

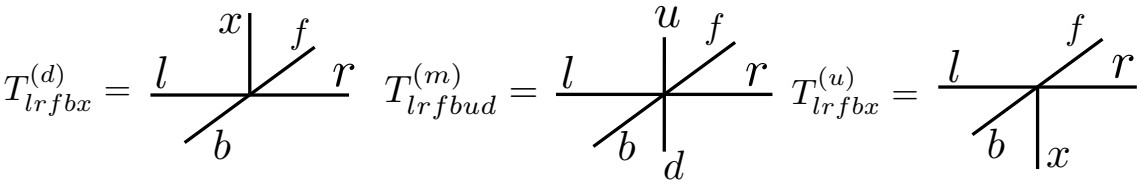

FIGURE 5.11: Local tensor for each constituent layer. $T^{(d)}$ and $T^{(u)}$ represent the local tensors on the lower and upper edge layer, respectively. $T^{(m)}$ represents the local tensor on the middle layer.

the edge layer are defined as in the two-layer case, but the local tensor of the middle layer has components that connects the upper and lower layers:

$$T^{(d)}_{lrfbx} = \begin{cases} z & \text{if } l=r=f=b=x=0; \\ 1 & \text{if only one index is 1;} \\ 0 & \text{otherwise,} \end{cases} \qquad T^{(u)}_{lrfbx} = \begin{cases} z & \text{if } l=r=f=b=x=0; \\ 1 & \text{if only one index is 1;} \\ 0 & \text{otherwise,} \end{cases} \tag{5.3}$$

$$T^{(m)}_{lrfbud} = \begin{cases} z & \text{if } l=r=f=b=u=d=0; \\ 1 & \text{if only one index is 1;} \\ 0 & \text{otherwise,} \end{cases} \tag{5.4}$$

where the last two indices of the $T^{(m)}$ represents the components that connect upper and lower layers.
(2) Compress the upper, middle and lower tensors (Fig.5.12):

$$T^{(\text{3layer})}_{LRFB} = \sum_{x} T^{(d)}_{l_1 r_1 f_1 b_1 u} T^{(m)}_{l_2 r_2 f_2 b_2 u d} T^{(u)}_{l_3 r_3 f_3 b_3 d}, \tag{5.5}$$

where large letter on the left side represents the tensor product of the indices of each tensor on the right side, e.g. $L = l_1 \otimes l_2 \otimes l_3$.

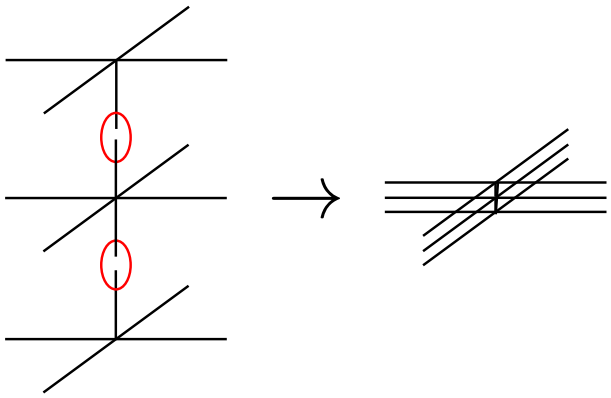

FIGURE 5.12: Compression of the upper, middle and lower local tensors.

We show the numerical results of the entropy and the monomer density calculated by DMRG using local tensor $T^{(3\text{layer})}_{LRFB}$. Fig.5.13 shows the entropy and linear fitting functions for a square three-layer lattice and a honeycomb three-layer lattice. At first glance, the plot is on a linear function, but if you look closely at the plot, you can see the deviation from the linear function.

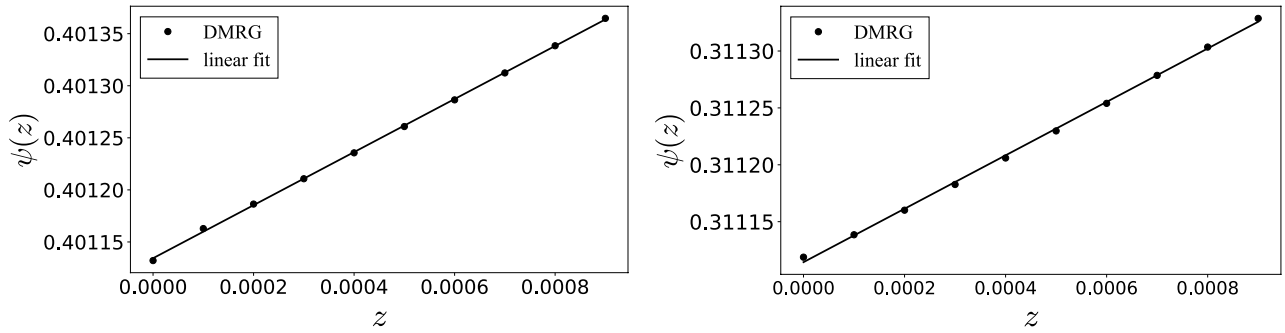

FIGURE 5.13: (Left) Entropy of square three-layer model as a function of the monomer weight z and the linear fitting function for it. In order to clearly show the deviation from linear behavior, a linear fitting function is displayed. The plots are extracted from DMRG with $m = 250$. (Right) The same function is plotted for honeycomb three-layer model ($m = 200$).

The same deviation from the linear function is shown in the monomer density in Fig.5.14. To confirm whether this deviations are caused by criticality, we plot $\rho(z)/z$ versus z in Fig.5.15 based on the assumption of $\rho(z) \sim z^{1+\frac{1}{\delta}}$ at $z \sim 0$. In Fig.5.15, the plots are on the linear straight line, therefore square three-layer and honeycomb three-layer lattice models are considered to be critical. According to the slope of the linear fitting function, the critical exponent is $\delta = 15.611$ for the square three-layer model and $\delta = 11.416$ for the honeycomb three-layer model. We have not clarified the reason for the difference in the value of δ between the square three-layer model and the honeycomb three-layer model. This difference may be due to the fact that the lattice geometry is isotropic or not to the bottom and sides.

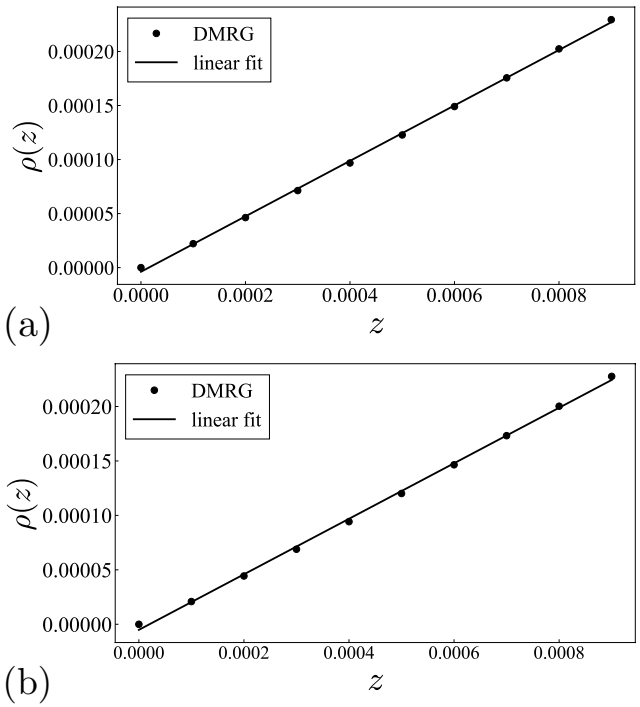

FIGURE 5.14: (a) Monomer density of the square three-layer model as a function of the monomer weight z and the linear fitting function for it. The plots are extracted from DMRG with $m = 250$. (b) The same function is plotted for the honeycomb three-layer model ($m = 200$).

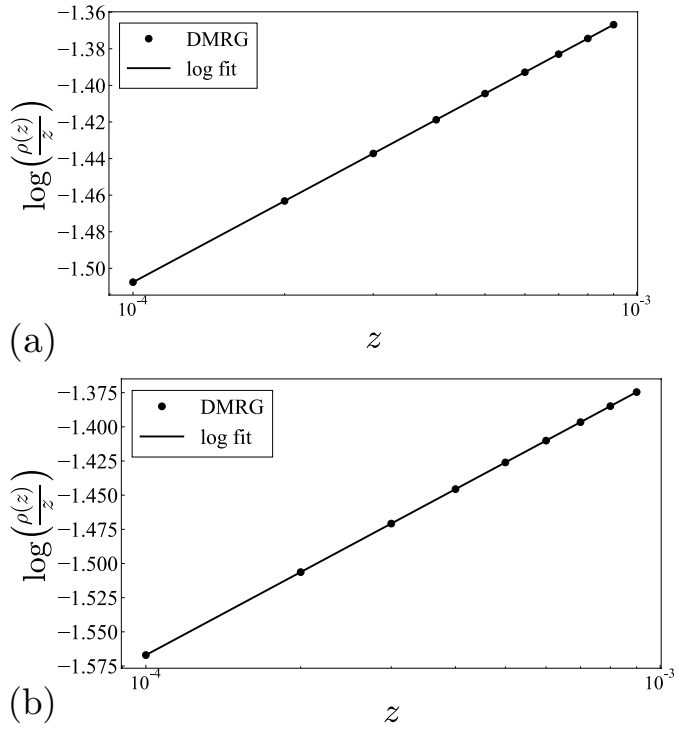

FIGURE 5.15: (a) The log of the monomer density over the monomer weight on the square three-layer lattice as a function of monomer weight z. The horizontal axis is log scale. (b) The same plots for the honeycomb three-layer lattice.

We show the correlation length data of the monomer-monomer correlation function as a supplementary evidence of criticality in Fig.5.16. Fig.5.16 shows that ξ diverges at $z = 0$ because ξ^{-1} approaches 0 as z approaches 0. Therefore square three-layer model and honeycomb three-layer model are critical, and three-layer bipartite lattice models are considered to be critical. This result seems to be consistent with hypothesis (A). In contrast to the two-layer case, the three-layer model reflects the characteristics of a bipartite 3D model, rather than a stack of 2D models.

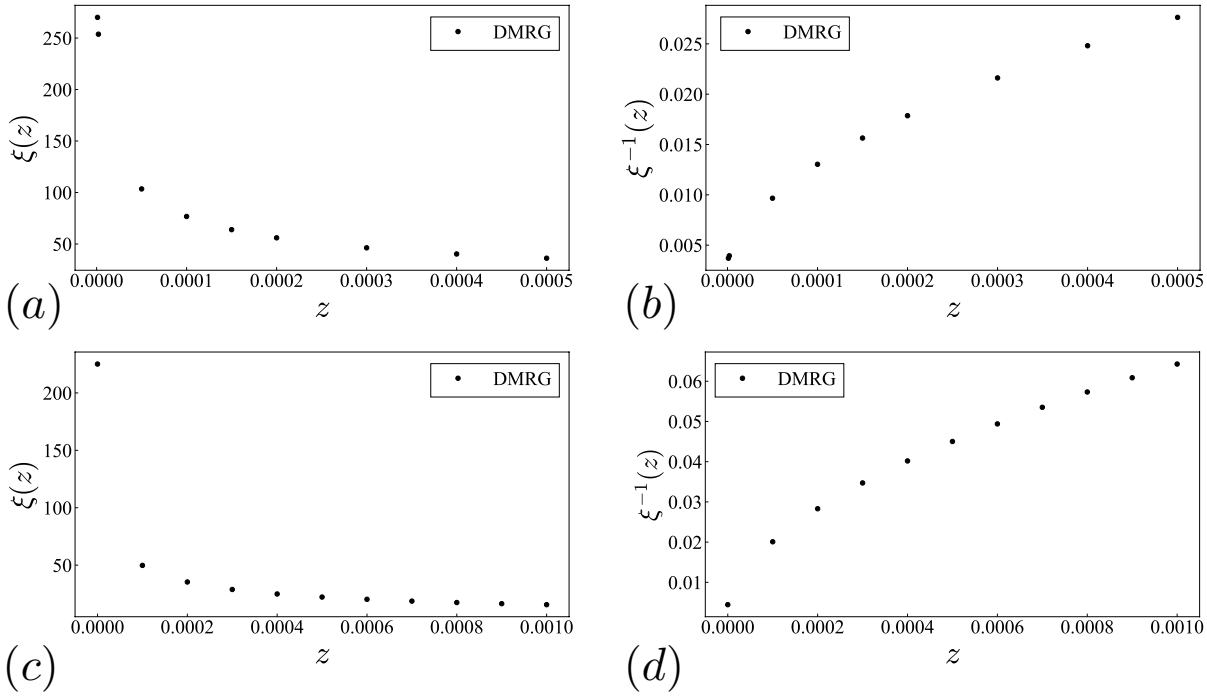

FIGURE 5.16: (a), (b) z-dependence of the correlation length and inverse of correlation length of the square three-layer model calculated from DMRG with $m = 200$. (c), (d) The same plots for the honeycomb three-layer lattice.

5.1.3 Discussion for multilayer bipartite lattice models

From the above analysis, we can see that the two-layer model is non-critical, while the three-layer model is critical. As a result, two hypotheses about the criticality of the multi-layer model can be naturally constructed.

1. Criticality depends on the oddness of the number of layers.
2. Only the two-layer model is a special system and is non-critical, while the multi-layer model other than the two-layer model is critical.

In order to confirm which hypothesis is correct, it is necessary to perform the analysis on a system with a larger number of layers. So, as a test, we perform calculations for the four-layer model. We show the z-dependence of the entropy by HOTRG in Fig.5.17. From the deviation of the entropy from the linear fitting function, the four-layer model seems to be critical. However, the accuracy of this calculation is not sufficient to determine criticality, but it does suggest that Hypothesis 2 is correct at this stage.

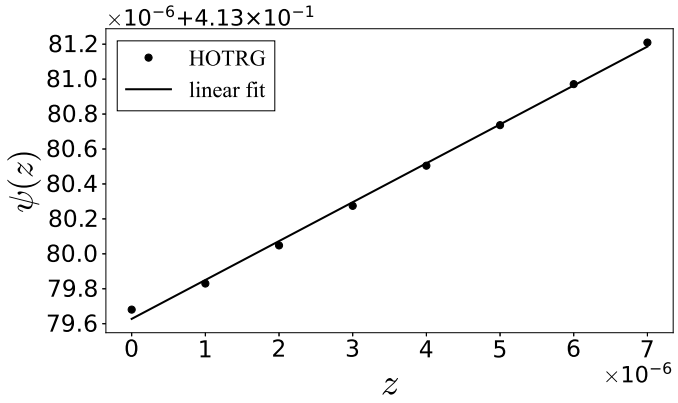

FIGURE 5.17: Entropy of the four-layer square model as a function of the monomer weight z and the linear fitting function for it. The plots are calculated using HOTRG with $D_{\text{bond}} = 100$.

5.2 Criticality of multilayer non-bipartite lattice models

We analyze MDM on a two-layer triangular lattice as an example of two-layer non-bipartite model. Since two-layer triangular lattice is non-bipartite, this model considered to be non-critical. Actually, non-criticality is reflected in the linear behavior of the entropy (Fig.5.18) and the monomer density (Fig.5.19).

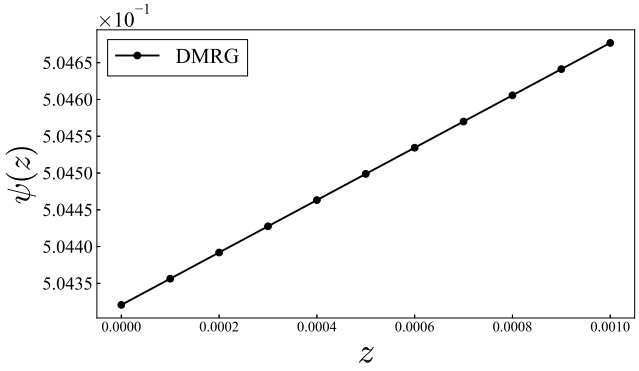

FIGURE 5.18: Entropy of the two-layer triangular model as a function of the monomer weight z and the linear fitting function for it. The plots are calculated using DMRG with $m = 180$.

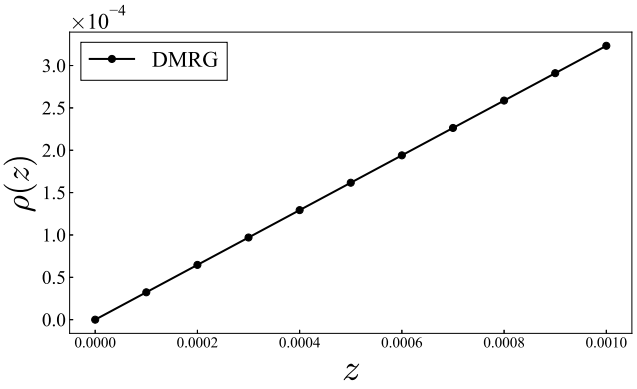

FIGURE 5.19: Monomer density of the two-layer triangular model as a function of the monomer weight z and the linear fitting function for it.

From the analogy of the two-layer triangular model, we guess multilayer non-bipartite lattice models are non-critical.

5.3 Description of the confinement and criticality in multilayer bipartite models based on a bosonic field theory.

In this section, we prepare a theoretical approach to the multilayer model in order to comprehensively understand its layered nature. Following Sec.2.5, dimers on a bipartite lattice can be described as magnetic fields and monomers are recognized as monopoles. With the goal of being able to explain confinement and criticality, we will extend the bosonization mapping introduced in Sec.2.5 to multilayer models.

To study long-distance behavior, coarse-graining the multilayer structure, MDM on the multilayer lattice corresponds to the magnetic field system of finite thickness (Fig.5.20). The direction perpendicular to the layer is the z-axis, and the layer is assumed to lie in the x-y plane. Also, the length of the thickness is L and the x-y plane is assumed to be infinite.

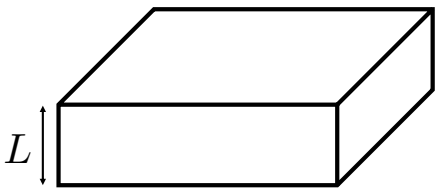

FIGURE 5.20: Magnetic field system of finite thickness.

In this setting, the field generated by a monopole (monomer) is given as the Green function of the Laplace equation:

$$-\Delta^{(3)} G(\boldsymbol{r}) = \delta^{(3)}(\boldsymbol{r}). \tag{5.6}$$

For simplicity, we impose periodic boundary condition and solve equation (5.6). Using Fourier expansion, $G(\boldsymbol{r})$ is given as follows:

$$\begin{aligned} G(\boldsymbol{r}) &= \int \frac{dk_x}{2\pi} \int \frac{dk_x}{2\pi} \frac{1}{L} \sum_{k_z} \frac{1}{k_x^2 + k_y^2 + k_z^2} e^{i(k_x x + k_y y + k_z z)} \\ &= \frac{1}{L} \sum_{k_z} e^{ik_z z} \int \frac{dk_x}{2\pi} \int \frac{dk_x}{2\pi} \frac{1}{k_x^2 + k_y^2 + k_z^2} e^{i(k_x x + k_y y)} \\ &= \frac{1}{L} \sum_{k_z} e^{ik_z z} G_2(\rho, |k_z|), \quad \rho = \sqrt{x^2 + y^2}, \end{aligned} \tag{5.7}$$

where $G_2(\rho, m)$ is defined as

$$G_2(\rho, m) = \int \frac{dk_x}{2\pi} \int \frac{dk_x}{2\pi} \frac{1}{k_x^2 + k_y^2 + m^2} e^{i(k_x x + k_y y)}, \tag{5.8}$$

and it is the Green function of the 2D Helmholtz equation:

$$(\Delta^{(2)} - m^2)\phi = 0. \tag{5.9}$$

The Green function of (5.9) is represented by using the Hankel function:

$$G_2(\rho, m) = \frac{i}{4} H_0^{(1)}(im\rho), \tag{5.10}$$

where $H_\nu^{(1)}$ is defined as

$$H_\nu^{(1)}(x) = \frac{e^{-i\pi\nu/2}}{i\pi} \int_{-\infty}^{\infty} e^{ix\cosh t - \nu t} dt. \tag{5.11}$$

Therefore, the behavior of $G_2(\rho, m)$ for $m \neq 0$ in the limit of $\rho \to \infty$ is

$$G_2(\rho, m) = \frac{1}{4\pi} \int_{-\infty}^{\infty} e^{-m\cosh t} dt \sim e^{-m\rho}. \tag{5.12}$$

In the last transformation, the integrals were evaluated using the saddle point method. On the other hand, zero mode $G_2(\rho, m = 0)$ corresponds to the 2D case. In this boundary condition, the zero mode exists and the long-range behavior is determined by the zero mode:

$$G_2(\boldsymbol{r}) \sim G_2(\rho, 0), \quad (r \to \infty). \tag{5.13}$$

From the behavior of the Green function, the property of the confinement and criticality of multilayer models are attributed to that of 2D bipartite model. Therefore, multilayer models are considered to be basically critical and confined. However, since the existence of zero modes depends on the boundary condition, the confinement and criticality also depend on the boundary condition. It can be seen from (5.7) and (5.12) that the monomer field decays exponentially in the long-range limit when we choose a boundary condition where there are no zero modes.

Even if we could relate the numerical setting to the boundary condition of the bosonic theory, the numerical results of the difference in criticality between the two- and three-layer models in Sec.5.1 cannot be explained in this framework. It is not clear at this stage, but if our numerical calculations correspond to the free boundary condition, then the confinement and criticality maps are shown in Fig.5.21. As for

the two-layer system, it is thought that the unique properties of the lattice model, which cannot be incorporated in the continuous field theory, are at work. For example, interlayer dimers cannot move in the z direction in the two-layer lattice model, but this effect is not reflected in the continuous field theory.

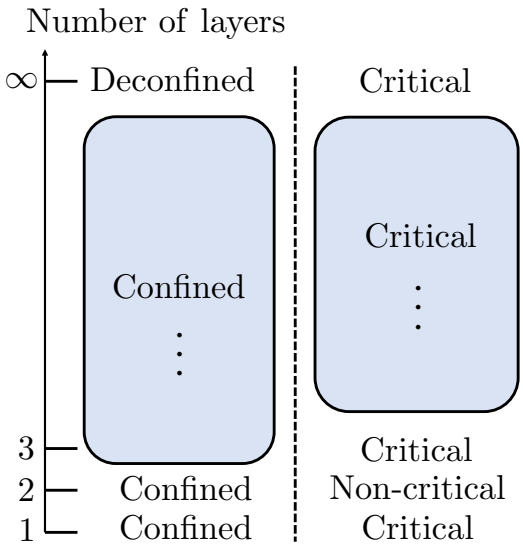

FIGURE 5.21: Classification diagram of criticality and confinement of the MDM on the multilayer bipartite lattice. The area enclosed by the square is the result of the bosonic theory.

5.4 Effect of the anisotropic dimer weight on the multilayer square lattice model

We also investigate the criticality of PDM in the two-layer square lattice model when the interlayer "dimer" activity (denoted by x_v) is varied. In Sec.5.1, we studied the case of $x_v = 1$, and discovered that two-layer bipartite model is non-critical. Even when x_v is changed, the criticality appears to remain unchanged (non-critical).

The local tensor of each constituent layer introduced as (5.1) is redefined as

$$T^{(u,d)}_{lrfbx} = \begin{cases} z & \text{if } l = r = f = b = x = 0; \\ \sqrt{x_v} & \text{if only } x \text{ is 1;} \\ 1 & \text{if the index of one of } l, r, f, \text{ or } b \text{ is 1;} \\ 0 & \text{otherwise.} \end{cases} \tag{5.14}$$

For $x_v \geq 1.0$, the behavior of $\rho(z) \sim z^2$ appears in the region of the order of $z \sim 10^{-3}$ (Fig.5.22, 5.23). The two-layer MDM at $x_v \geq 1.0$ is also considered to be non-critical because it has the same z^2-dependence as the behavior at $x_v = 1.0$ described in Sec.5.1.

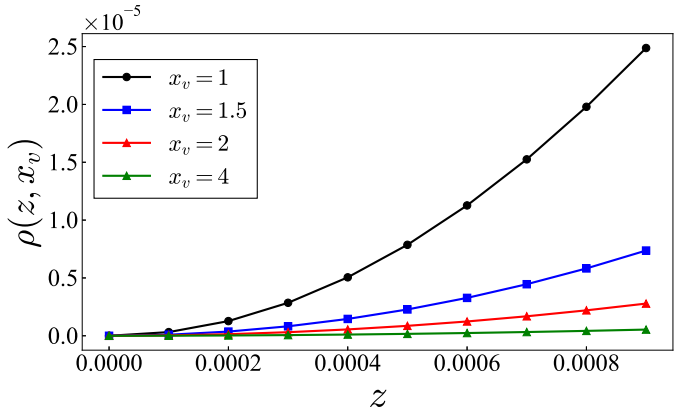

FIGURE 5.22: z-dependence of monomer density for different values of $x_v (x_v \geq 1)$. The plots are calculated from DMRG with $m = 400$.

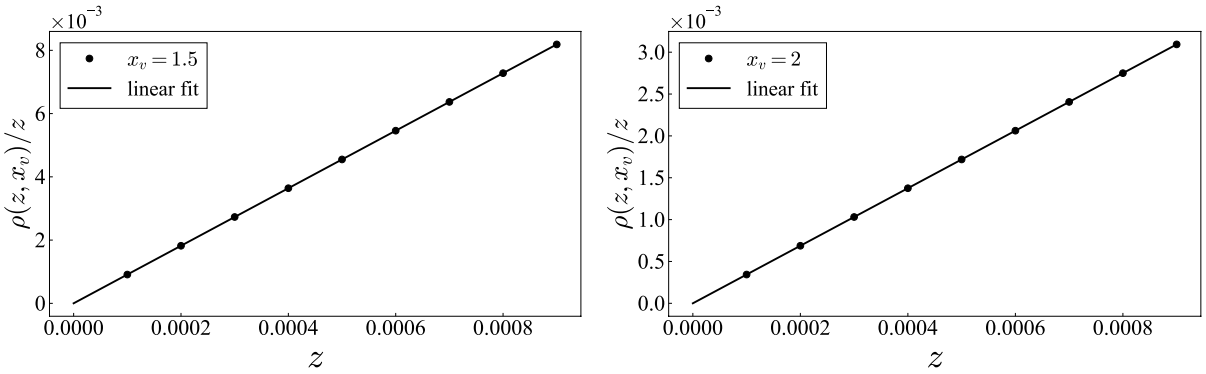

FIGURE 5.23: (Left) Monomer density over z for $x_v = 1.5$ calculated from DMRG with $m = 600$. The straight line represents linear fitting function. (Right) The same plots for $x_v = 2.0$.

For $x_v \geq 0.6$, the behavior of $\rho(z) \sim z^2$ does not appear in the region of the order of $z \sim 10^{-3}$ but appears in the region of the order of $z \sim 10^{-6}$ (Fig.5.24).

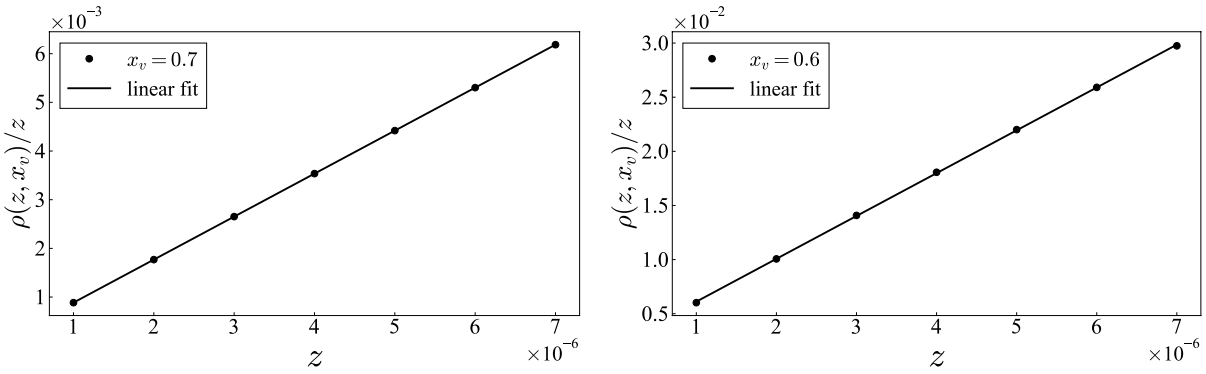

FIGURE 5.24: (Left) Monomer density over z for $x_v = 0.7$ calculated from DMRG with $m = 600$. The straight line represents linear fitting function. (Right) The same plots for $x_v = 0.6$.

For $x_v \leq 0.4$, z^2-dependence of $\rho(z)$ does not still appear as shown in Fig.5.25. From the analysis of the correlation length in Fig.5.26, the correlation length does

not diverge near $z = 0$ and two-layer MDM is considered to be non-critical both for $x_v = 0.1$ and $x_v = 0.4$.

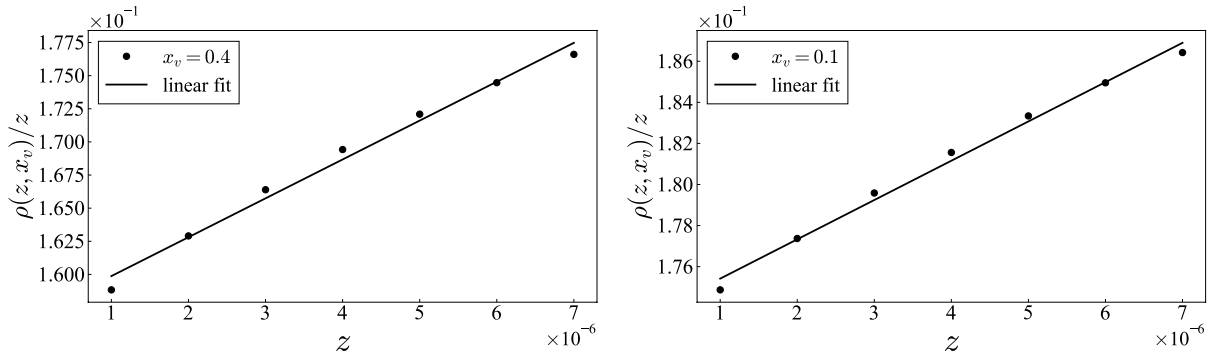

FIGURE 5.25: (Left) Monomer density over z for $x_v = 0.4$ calculated from DMRG with $m = 500$. The straight line represents linear fitting function. (Right) The same plots for $x_v = 0.1$.

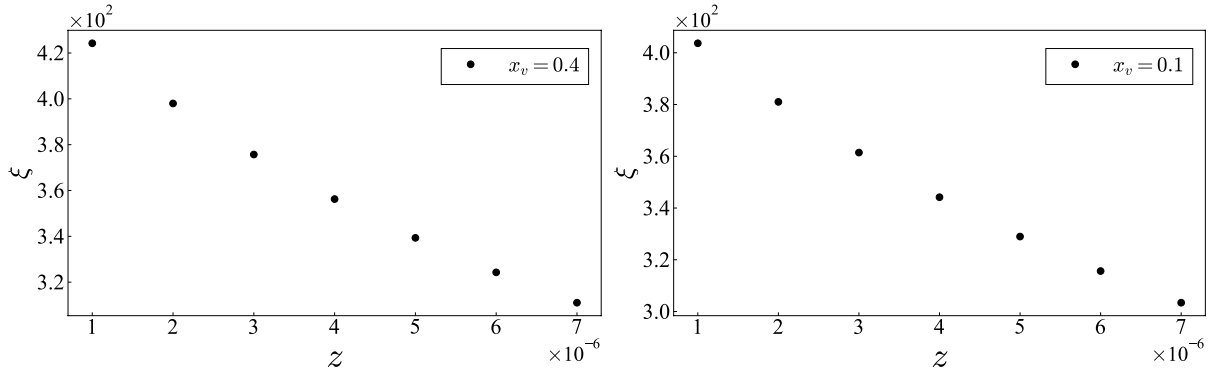

FIGURE 5.26: (Left) z-dependence of correlation length for $x_v = 0.4$ calculated from DMRG with $m = 500$. (Right) The same plots for $x_v = 0.1$.

Here, we refer to Ref.[63] as a comparison, which also studies the criticality of two-layer PDM varying x_v by renormalization group approach. The authors consider the interaction between dimers on different layers, and shows that there is a Kosterlitz-Thouless (KT) transition in the presence of finite repulsive interaction (Fig.5.27). They conclude that in region of small x_v at non-interacting case $V = 0$ (in our case), there seems to be critical region, but it only reflects the long crossover from the finite interaction region and is non-critical.

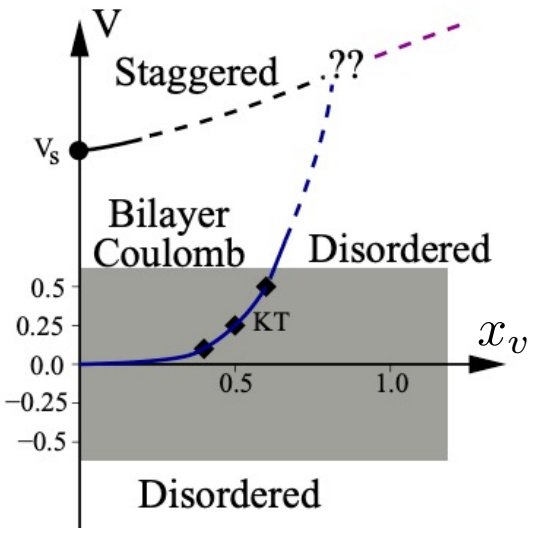

FIGURE 5.27: Phase diagram in terms of the strength of interaction and the dimer activity on the edge perpendicular to the layer surface from Ref.[63]. The phase boundary represents the location where the KT transition from the critical Bilayer Coulomb phase to the non-critical disordered phase occurs.

According to Ref.[63], since the two-layer PDM is non-critical for all $x_v(\neq 0)$, our calculations varying x_v is consistent in terms of the criticality. As an explanation for the behavior in $x_v \leq 0.4$, we guess that the region of z where $\rho(z) \sim z^2$ is valid becomes smaller as x_v approaches $x_v = 0$. This is because two-layer system approaches two decomposed one-layer square lattice as $x_v \to 0$, and the criticality of the square lattice probably affects the behavior of $\rho(z)$. Future work requires analysis in the region close to $z = 0$, and clarification of the relationship between $\rho(z)$ and x_v.

Chapter 6

Analysis of the monomer-dimer model on a three-dimensional lattice

Numerical analysis in three dimensions is one of the important goals of HOTRG. However, in the ordinary algorithm of HOTRG, the memory cost is too large in three dimensions to perform highly accurate calculations. Therefore, in this section, we analyze three-dimensional PDM and MDM using our parallel computation method introduced in Sec.3.2. The criticality of three-dimensional model is known for several lattice geometry[61], but the critical behavior of the thermal quantities is not understood. Therefore, we analyzed the monomer activity dependence of the residual entropy of PDM and the entropy of MDM.

6.1 Numerical calculation of the residual entropy of the pure dimer model

As well as 2D PDM, 3D PDM has a finite residual entropy due to the degenerate ground state. However, unlike the two-dimensional case, the three-dimensional PDM does not have an analytical solution. Therefore, a numerical approach is necessary. In this section, we calculate the residual entropy by HOTRG. Additionally, we will validate the accuracy of HOTRG in three dimensions by comparing it with previous studies.

As shown in Fig.6.1, we calculate the residual entropy of the PDM by varying the number of retained basis D_{bond}. For comparison, the values calculated by the asymptotic expansion [84] and one of the TN methods, PEPS[86] are also shown. On a two-dimensional square lattice, the value of Z_{persite} by the asymptotic expansionis slightly smaller than the exact value, but is consistent within the third minority (± 0.0001)[84]. Therefore, we can assume that the value of the asymptotic expansion is in the neighborhood of the exact value, even for a 3D lattice. From Fig.6.1, it can be seen that our calculated values asymptotically approach slightly above the value of the asymptotic expansion and are closer to the value of PEPS. In conclusion, the optimization of the contraction order done in Sec.3.2.2 and the parallel computation method done in Sec.3.2 allowed us to calculate the residual entropy of PDM on a cubic lattice with higher accuracy than the previous PEPS[86].

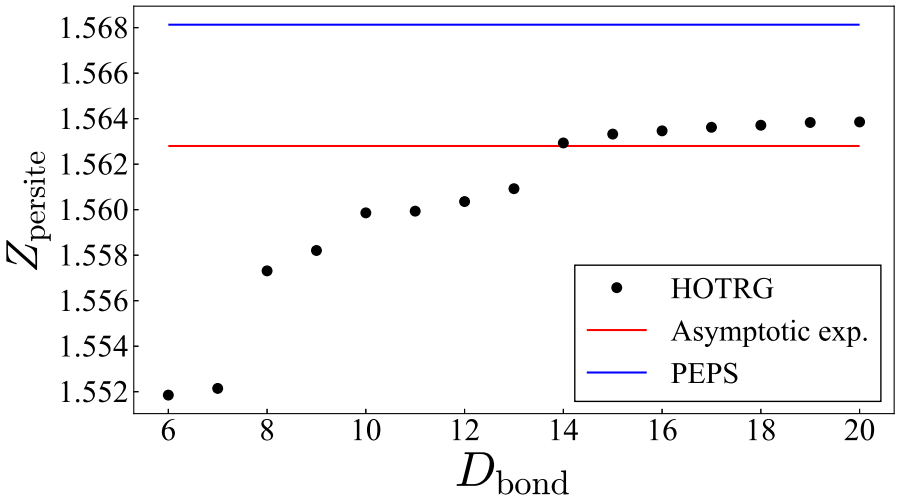

FIGURE 6.1: D_{bond} dependence of the partition function of 3D PDM per site Z_{persite}. The plots for $D_{\text{bond}} \geq 17$ are calculated by the parallel computation method in Sec.3.2. A red line represents the value calculated by the asymptotic expansion[84]. A blue line represents the value calculated by PEPS[86].

6.2 Critical behavior of the entropy

The criticality of 3D PDM is known for the several lattice geometry, such as the cubic, fcc and Fisher lattice as shown in Table2.2[61]. However, the critical behavior of thermal function and the universality class are not known. Therefore, we analyze z-dependence of entropy in MDM on the cubic lattice, and try to determine the critical exponent δ defined as Eq.4.1.

z-dependence of the entropy is shown as Fig.6.2. In the neighborhood of $z = 0$, the behavior of entropy is not linear, but curvilinear. This is the behavior that reflects the criticality.

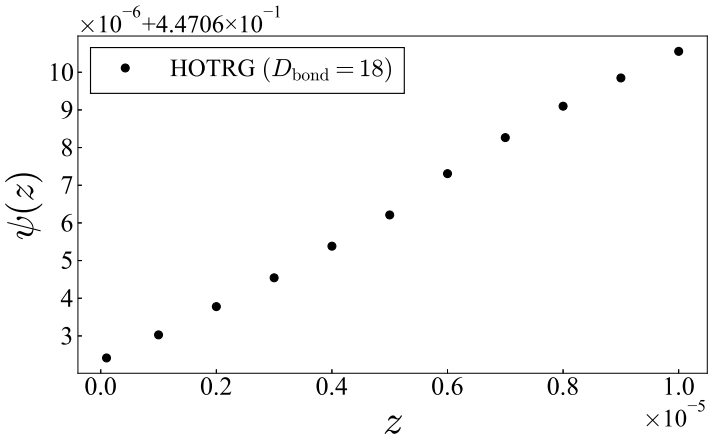

FIGURE 6.2: z-dependence of the entropy of MDM on the cubic lattice calculated by HOTRG with $D_{\text{bond}} = 18$.

Next, we will determine the the critical exponent δ by fitting approach. In order to construct a fitting function, we extract plots of regions with significant curvilinear

behavior. We assume the critical form of fitting function of the entropy as

$$\psi_{\text{fit}}(z) = a + b \cdot z^{1+\frac{1}{\delta}}, \quad z \sim 0 \tag{6.1}$$

which comes from the critical behavior of $\rho(z)$ (4.1) and the relation between $\psi(z)$ and $\rho(z)$ (2.8). Here, we identify the value of a as $\psi(0)$ calculated from HOTRG. δ can then be determined by calculating the slope of the log fitting of the following equation:

$$\log\left(\psi_{\text{fit}}(z) - \psi(0)\right) = \log b + \left(1 + \frac{1}{\delta}\right) \log z. \tag{6.2}$$

The plots of (6.2) is shown in Fig.6.3, and the plots are on the straight line. From this plots, the critical exponent is calculated as $\delta = 7.632629$. However, the value of δ varies depending on the choice of plot. Therefore, the accuracy of the present calculation is not sufficient to determine the critical exponent.

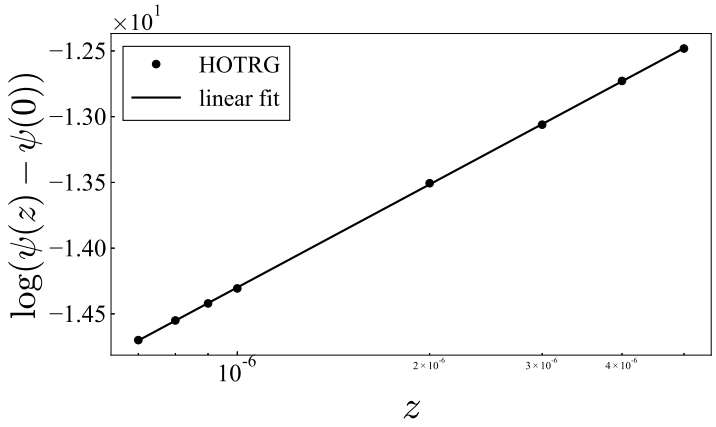

FIGURE 6.3: The log of the entropy on the cubic lattice as a function of z. The horizontal axis is log scale.

6.3 Singular value distribution of the three-dimensional HOTRG

In Sec.6.2, we could not determine the critical exponent δ by HOTRG with $D_{\text{bond}} = 18$. On the other hand, some critical exponents of the three-dimensional Ising model can be precisely determined by HOTRG with $D_{\text{bond}} = 14$[57]. Therefore, in this section, we discuss whether D_{bond} was appropriate for the HOTRG calculation of the monomer-dimer system in this study by analyzing the distribution of singular values (eigenvalues of $MM^\dagger$) defined by (3.10). In particular, we compare the singular value distributions of the monomer-dimer system with those of the Ising model. The comparison of D_{bond}-dependence of the singular value of 3D MDM and the 3D Ising model at the critical point is shown as Fig.6.4. Fig.6.4 shows that the singular value of the 3D Ising model decays rapidly around $D_{\text{bond}} = 11$, while that of 3D MDM does not decay even after $D_{\text{bond}} = 20$. Therefore, D_{bond} was sufficient for HOTRG calculation of the 3D Ising model in Ref.3.8, but the value of D_{bond} that we set is not considered to be sufficient for analyzing the critical behavior of 3D MDM precisely. Furthermore, the degeneracy of the large singular values of 3D MDM is larger than

that of the 3D Ising model, and this degeneracy prevents the singular values from decreasing.

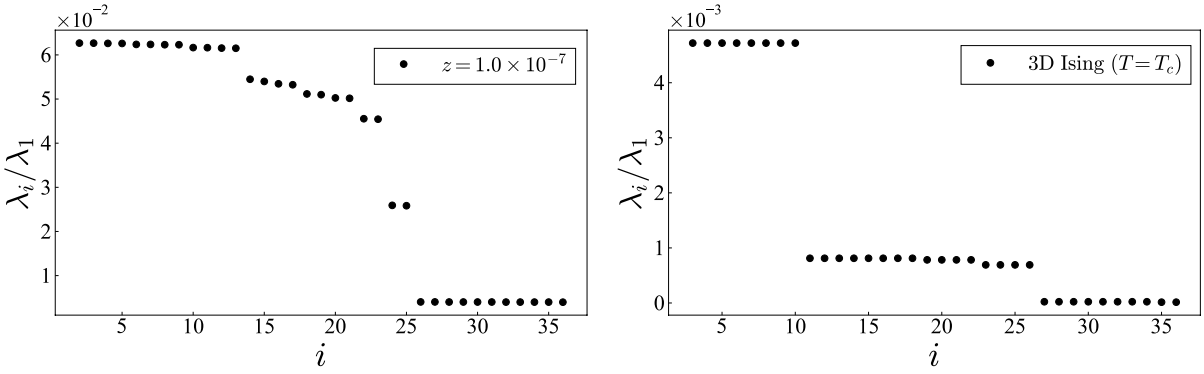

FIGURE 6.4: (Left) D_{bond}-dependence of singular values of 3D MDM at $z = 1.0 \times 10^{-7}$. The value of the singular value is a ratio to the maximum singular value, starting from the value of the second largest singular value. (Right) Same plots for the 3D Ising model.

As shown in Fig.6.5, the degenerate structure and the behavior of singular values of 3D MDM do not change even after leaving the critical point. Therefore, we believe that our HOTRG calculations for the region where critical behavior appears, as well as the critical point, are not accurate enough to determine the critical exponent.

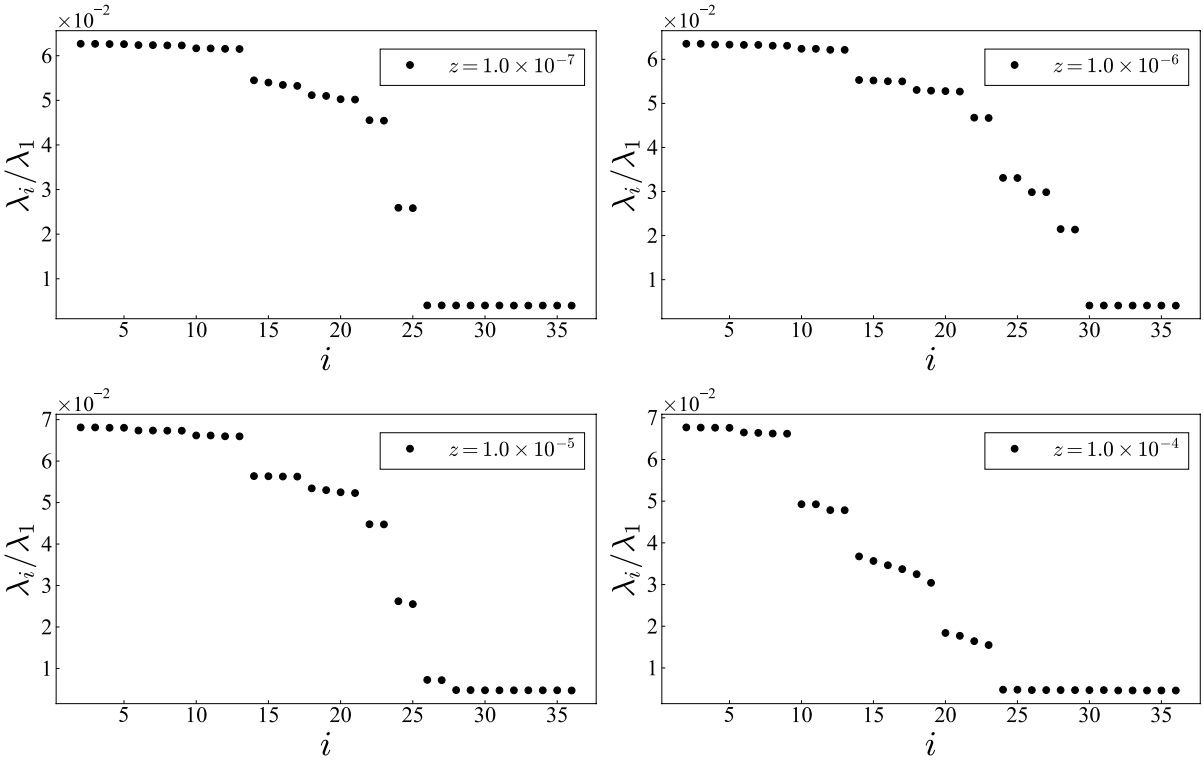

FIGURE 6.5: D_{bond}-dependence of singular values of 3D MDM for various values of z.

To summarize our current status, HOTRG analysis in 3D monomer-dimer system is efficient for calculating residual entropy of PDM. For a discussion of critical phenomena, although we can not determine the critical exponent precisely, we can

capture the critical behavior that appears in the entropy. From the comparison of the singular value distributions of the 3D MDM and the 3D Ising model, the degeneracy of the singular values and the delay in decay are considered to be the cause of the reduced accuracy of HOTRG calculation of MDM. In particular, the high degree of degeneracy is thought to be specific to MDM, but the reason for this has not been clarified. Therefore, the next task is to identify the causes of the difficulties and develop ways to deal with them. We then need to set D_{bond} appropriately, which is sufficient to determine the critical exponent of 3D MDM.

Chapter 7

Asymptotic spectrum distribution of HOTRG: Relationship to the corner transfer matrix

In this chapter, we analyze the asymptotic behavior of the spectrum of $MM^\dagger$ in HOTRG. For the integrable models at off-critical region, $MM^\dagger$ spectrum can be described by the eigenvalue of the Baxter's corner transfer matrix (CTM)[67]. Therefore, we derive the asymptotic form of $MM^\dagger$ spectrum of HOTRG based on the CTM representation and check this form by HOTRG calculation at $D_{\text{bond}} = 240$. Furthermore, we compare the spectra of the density matrix in DMRG to show that there is some relationship between DMRG and HOTRG in the asymptotic behavior of the spectrum.

7.1 Review of the corner double line representation of vertex weights in HOTRG

We consider the vertex weight of the HOTRG in the off-critical region at a fixed point where the correlation length of the system is finite. When the system size is much larger than the correlation length: $L \gg \xi$, the link variables around different corners are disentangled in the square lattice model. Therefore, the vertex tensor at a fixed point W^* is decomposed into four tensors corresponding to the CTM, and such a picture is called a corner double line (CDL) picture[56, 87].

In 2D HOTRG, the renormalization of two adjacent vertex weights (local tensors) is given as

$$M^{(n)}_{x_a x_b x'_a x'_b y_a y'_b} = \sum_y W^{(n)}_{x_a x'_a y_a y} W^{(n)}_{x_b x'_b y y'_b}, \tag{7.1}$$

which corresponds to (3.4). To calculate singular values by HOSRG, we diagonalize a following kind of density matrix

$$\rho^{(n)}_{x'_a x'_b,\ x_a x_b} = \sum_{x''_a x''_b y_a y_b} M^{(n)}_{x_a x_b x''_a x''_b y_a y_b} M^{(n)}_{x'_a x'_b x''_a x''_b y_a y_b}, \tag{7.2}$$

which corresponds to $MM^\dagger$ appearing in (3.9).

At the fixed point, the link variables of the vertex weight W^* around different corners are disentangled, so W^* is decomposed into four CTM as shown in Fig.7.1:

$$W^*_{\mu\mu'\nu\nu'} = \kappa A_{\mu_1\nu_1} A_{\mu_2\nu_2} A_{\mu'_1\nu'_1} A_{\mu'_2\nu'_2}, \tag{7.3}$$

where κ is a normalization factor and $A_{\mu\nu}$ is normalized CTM ($\dim(\mu) = \sqrt{2^n}$). Here, W^* is assumed to be isotropic. CTM is defined as a transfer matrix that transfers an element on a semi-infinite horizontal line to an element on a semi-infinite vertical line (Fig.7.2).

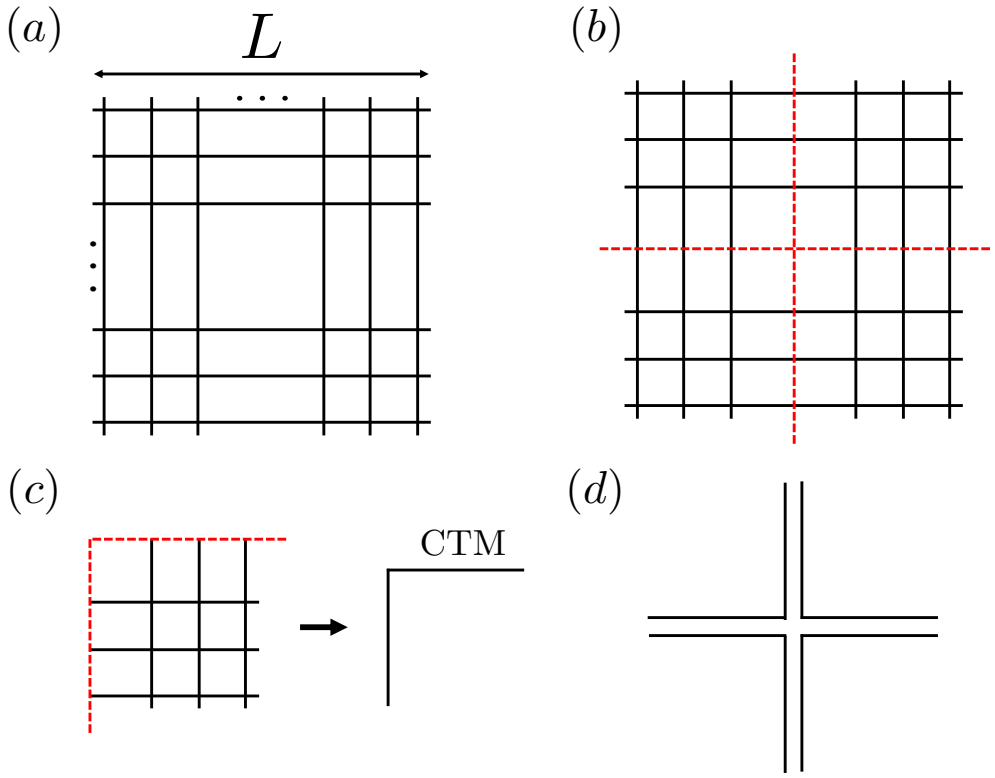

FIGURE 7.1: Decomposition of the vertex weight into CTMs (The figure refers to Ref.[88]). (a) Renormalized vertex weight with system size L. (b) When $L \gg \xi$, the link variables of the vertex weight around different corners are disentangled and the vertex weight decomposed into four patches. (c) Correspondence of each patch to CTM. (d) Diagram of vertex weights by CTM correspondence. This double line diagram is called corner double line (CDL) representation.

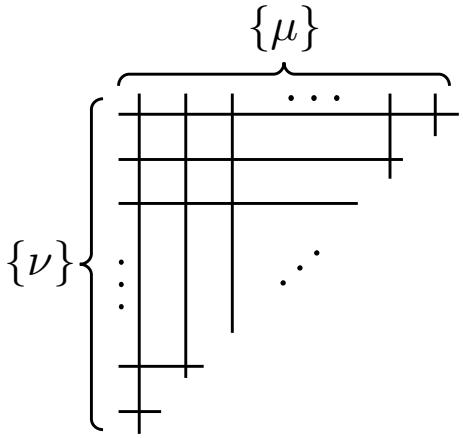

FIGURE 7.2: Graphical representation of corner transfer matrix (CTM): $A_{\mu\nu}$.

Substituting CDL representation of the vertex weight (7.3) into (7.2), ρ^* can be expressed using CTM:

$$\rho^*_{\mu'_a\mu'_b,\mu_z\mu_b} = \alpha(A^2)_{\mu_1\mu'_1}(A^2)_{\mu_2\mu_3}(A^2)_{\mu'_2\mu'_3}(A^2)_{\mu'_4\mu_4}, \tag{7.4}$$

where $\alpha = \kappa^4(\mathrm{Tr}[A^2])^2$, $\mu_a = \mu_1 \otimes \mu_2, \mu_b = \mu_3 \otimes \mu_4$, $\mu'_a = \mu'_1 \otimes \mu'_2$, and $\mu'_b = \mu'_3 \otimes \mu'_4$. Next, we diagonalize ρ^*. However, $(A^2)_{\mu_2\mu_3}$ and $(A^2)_{\mu'_2\mu'_3}$ in (7.4) are each represented as a tensor product of two vectors, with rank 1 and eigenvalues of 1. Therefore, each does not contribute the eigenvalues of ρ^* and only $\alpha A^2 \otimes A^2$ need to be considered. So, the eigenvalues of ρ^* (spectrum of $MM^\dagger$) is given as[67]

$$(\rho^*)_{\mathrm{diag}} = \alpha(A^2)_{\mathrm{diag}} \otimes (A^2)_{\mathrm{diag}}. \tag{7.5}$$

7.2 Asymptotic form of the $MM^\dagger$ spectrum

In this section, we introduce the asymptotic form of $MM^\dagger$ spectrum (eigenvalues of ρ^*) by using the asymptotic behavior of CTM and CDL representation of ρ^* in (7.5). In case of the integrable model at off-critical region, the diagonalized form of CTM in the thermodynamic limit is given as the form of infinite tensor product[89]:

$$(A(z))_{\mathrm{diag}} = \bigotimes_{n=1}^{\infty} \begin{pmatrix} 1 & 0 \\ 0 & z^{c_n} \end{pmatrix}, \tag{7.6}$$

where we have imposed normalization condition that the maximum eigenvalue is 1, and $z(0 < z < 1)$ is some parameter that characterizes the family of integrable models (we omitted this index in the last section). c_n is a model-dependent parameter and for example of the Ising model, the value of c_n is as follows:

$$c_n = \begin{cases} n & (T < T_c) \\ 2n-1 & (T > T_c). \end{cases} \tag{7.7}$$

From (7.6),

$$A^2(z) = A(z^2), \tag{7.8}$$

and substituting this relation into (7.5), $(\rho^*)_{\mathrm{diag}}$ can be represented as

$$\begin{aligned} (\rho^*)_{\mathrm{diag}}(z) &= (A^2(z))_{\mathrm{diag}} \otimes (A^2(z))_{\mathrm{diag}} && (7.9) \\ &= (A(z^2))_{\mathrm{diag}} \otimes (A(z^2))_{\mathrm{diag}} \\ &= \left[\bigotimes_{n=1}^{\infty} \begin{pmatrix} 1 & 0 \\ 0 & z^{2c_n} \end{pmatrix}\right] \otimes \left[\bigotimes_{n=1}^{\infty} \begin{pmatrix} 1 & 0 \\ 0 & z^{2c_n} \end{pmatrix}\right], && (7.10) \end{aligned}$$

where we impose the normalization that the maximum eigenvalue is 1 on both sides. Therefore, the eigenvalues of ρ^* is given as the power-law form of z. However, since each eigenvalue has a degeneracy, we need to calculate the degeneracy to associate the eigenvalue number with the eigenvalue.

First, we evaluate the degeneracy of the eigenvalue z^n. According to Ref.[90], the degeneracy of eigenvalue q^n of CTM $(A(q))$ is determined by a coefficient $r(n)$ of the

generating function $f(q)$:

$$\begin{aligned} f(q) :&= \mathrm{Tr} \bigotimes_{n=1}^{\infty} \begin{pmatrix} 1 & 0 \\ 0 & q^{c_n} \end{pmatrix} \\ &= \prod_{n=1}^{\infty} (1 + q^{c_n}) \\ &= \prod_{n=1}^{\infty} (1 - q^n)^{-a_n} \qquad (7.11) \\ &= 1 + \sum_{n=1}^{\infty} r(n) q^n, \qquad (7.12) \end{aligned}$$

where a_n is a sequence depending on c_n. According to Meinardus's theorem, the asymptotic form of $r(n)$ in the limit of $n \to \infty$ is given as[91]

$$r(n) \sim C n^k \exp\left[B n^{\alpha/(1+\alpha)}\right], \qquad (7.13)$$

$$k = \frac{D(0) - 1 - \frac{\alpha}{2}}{1 + \alpha}, \qquad (7.14)$$

$$B = \left(1 + \frac{1}{\alpha}\right) A^{1/(\alpha+1)} \times \tilde{B}(\alpha), \qquad (7.15)$$

where α is the pole of

$$D(s) = \sum_{n=1}^{\infty} \frac{a_n}{n^s}, \qquad (7.16)$$

and A is the fraction at pole α.

Similarly, the generating function for $A(q) \otimes A(q)$ can be constructed as follows:

$$\begin{aligned} \mathrm{Tr}\left[A(q) \otimes A(q)\right] &= (\mathrm{Tr} A(q))(\mathrm{Tr} A(q)) \\ &= [f(q)]^2 \\ &= \prod_{n=1}^{\infty} (1 - q^n)^{-2a_n}. \qquad (7.17) \end{aligned}$$

(7.17) is equivalent to (7.11) with a_n replaced by $2a_n$. Therefore, the corresponding series $D(s)$ is just doubled. As a result, the position of the poles, α, remains the same, and the residue doubles to the value 2A. Therefore, the exponential part of the asymptotic form of the degeneracy $r(n)$ is modified as follows:

$$\exp\left[B n^{\alpha/(1+\alpha)}\right] \to \exp\left[2^{1/(1+\alpha)} B n^{\alpha/(1+\alpha)}\right]. \qquad (7.18)$$

Here, we consider the case of $\alpha = 1$, which corresponds to the case where the value of c_n is given as (7.7). Then, (7.18) becomes

$$\exp\left[B\sqrt{n}\right] \to \exp\left[\sqrt{2} B \sqrt{n}\right]. \qquad (7.19)$$

The eigenvalue number m taking the degeneracy into consideration is

$$m = \sum_{l=1}^{n} r(l). \tag{7.20}$$

Changing the summation in (7.20) into the integration, we obtain

$$\begin{aligned} m &\sim \int_1^n x^k \exp\left[\sqrt{2}B\sqrt{x}\right] dx \\ &= 2\int_1^{\sqrt{n}} t^{2k+1} \exp\left[\sqrt{2}Bt\right] dt \quad (\sqrt{x} = t,\ dk = 2tdt) \\ &\sim n^{k+1/2} \exp\left[\sqrt{2}B\sqrt{n}\right]. \end{aligned} \tag{7.21}$$

Taking the log of both sides, we get

$$\begin{aligned} \log m &\sim \sqrt{2}B\sqrt{n} + \left(k + \frac{1}{2}\right)\log n \\ &\sim \sqrt{2}B\sqrt{n}, \end{aligned} \tag{7.22}$$

and from this,

$$n \sim \frac{B^2}{2}(\log m)^2. \tag{7.23}$$

This is the degeneracy of the eigenvalue q^n of $A(q) \otimes A(q)$.

Next, we derive the asymptotic form of the m-th eigenvalue of $A(q) \otimes A(q)$, denoted by $\Omega_m(q)$. By definition of $\Omega_m(q) (= q^n)$,

$$n = \frac{\log \Omega_m(q)}{\log q}. \tag{7.24}$$

Combining (7.23) and (7.24), we get

$$\Omega_m(q) \sim \exp\left[\frac{B^2 \log q}{2}(\log m)^2\right]. \tag{7.25}$$

According to (7.10), the asymptotic form of ρ^* is given as

$$\Omega_m(z^2) \sim \exp\left[(B^2 \log z)(\log m)^2\right]. \tag{7.26}$$

On the other hand, the asymptotic form of m-th eigenvalue of CTM ($A(z)$) is

$$\omega_m(z) \sim \exp\left[(B^2 \log z)(\log m)^2\right], \tag{7.27}$$

and this is equivalent to that of ρ^* (7.26):

$$\Omega_m(z^2) \sim \omega_m(z). \tag{7.28}$$

Finally, we relate the asymptotic behavior of the eigenvalues of ρ^* in HOTRG to the asymptotic behavior of the eigenvalues of the density matrix in DMRG defined as (3.32). Since the density matrix of DMRG is equivalent to four CTMs[92]:

$$\mathrm{DM} = A(z) \otimes A(z) \otimes A(z) \otimes A(z), \tag{7.29}$$

the eigenvalues of the density matrix in DMRG $\{\lambda_m(z)\}$ is related to the eigenvalues of CTM asypmtotically as follows:

$$\lambda_m(z) \sim [\omega_m(z)]^4. \tag{7.30}$$

Combining (7.28) and (7.30), we obtain the relation of the asymptotic spectrum for the integrable models between HOTRG and DMRG:

$$\Omega_m(z^2) \sim [\lambda_m(z)]^{1/4}. \tag{7.31}$$

7.3 Numerical result of asymptotic behavior of the $MM^\dagger$ spectrum

In this section, we confirm numerically establishment of the relation of the asymptotic spectrum between HOTRG and DMRG (7.31). We analyze the eigenvalue distribution of the specific models using both DMRG and HOTRG. For HOTRG, we use the parallel computation method which is introduced in Sec.3.2 to preform calculation at large number of retained basis $D_{\text{bond}} = 240$. For example, we analyze the 2D Ising model at high temperature phase as an integrable model, and 2D MDM and the 2D Ising model at the critical temperature with a magnetic field as non-integrable models.

7.3.1 Integrable models

From (7.26), asymptotic form of the spectrum of HOTRG is

$$\log \Omega_m(z^2) \sim \left[(B^2 \log z)(\log m)^2\right], \tag{7.32}$$

while from this relation and (7.31), that of DMRG is given as

$$\log \left(\lambda_m(z)^{\frac{1}{4}}\right) \sim \left[(B^2 \log z)(\log m)^2\right]. \tag{7.33}$$

Therefore, the dependence of the asymptotic form of the spectrum on the number of eigenvalues $(\log m)^2$ is the same for $\log\left(\Omega_m(z^2)\right)^4$ of HOTRG and $\log\left(\lambda_m(z)\right)$ of DMRG. The establishment of this relation is seen from Fig.7.3. We conclude that relation (7.31) is valid for integrable models.

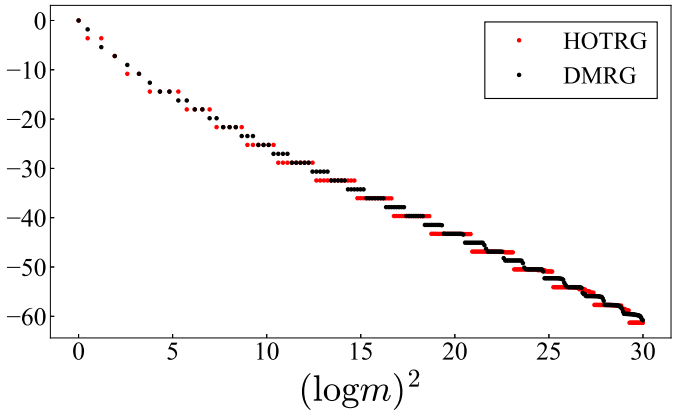

FIGURE 7.3: Eigenvalue distribution for $(\log m)^2$ of Ising model at high temperature phase. The value of the vertical axis is $\log\left(\Omega_m(z^2)\right)^4$ for HOTRG and $\log\left(\lambda_m(z)\right)$ for DMRG. This calculation is performed using high-temperature expansion. The number of retained basis is $m_{\text{base}} = 240$ for DMRG and $D_{\text{bond}} = 240$ for HOTRG.

7.3.2 Non-integrable models

In this section, we also calculate the asymptotic spectral for non-integrable models such as 2D MDM and 2D Ising model with a magnetic field. We show the eigenvalue distribution of 2D Ising model with a magnetic field in Fig.7.4 and 2D MDM in Fig.7.5, respectively. Both graphs show a difference in the behavior of the eigenvalues between HOTRG and DMRG. Consequently, relation (7.31) is not valid for the non-integrable models. Thus, we propose that an effective way to determine whether a system is integrable or not is to examine the difference between whether (7.31) holds or fails.

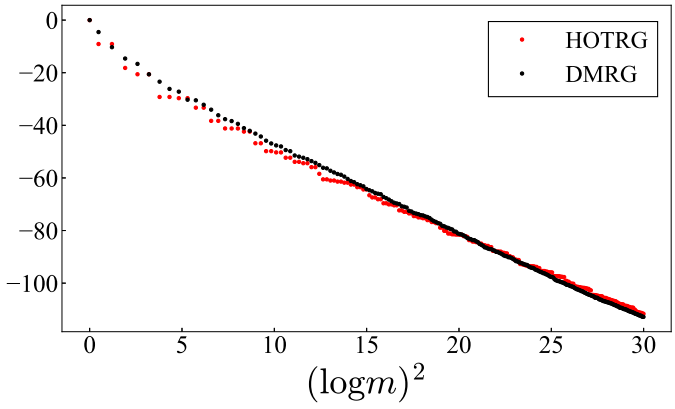

FIGURE 7.4: Eigenvalue distribution for $(\log m)^2$ of Ising model with a magnetic field at $T = T_c$, where the strength of magnetic filed is $\tanh(\beta h) = 0.01$. The value of the vertical axis is $\log\left(\Omega_m(z^2)\right)^4$ for HOTRG and $\log\left(\lambda_m(z)\right)$ for DMRG. The number of retained basis is $m_{\text{base}} = 240$ for DMRG and $D_{\text{bond}} = 240$ for HOTRG.

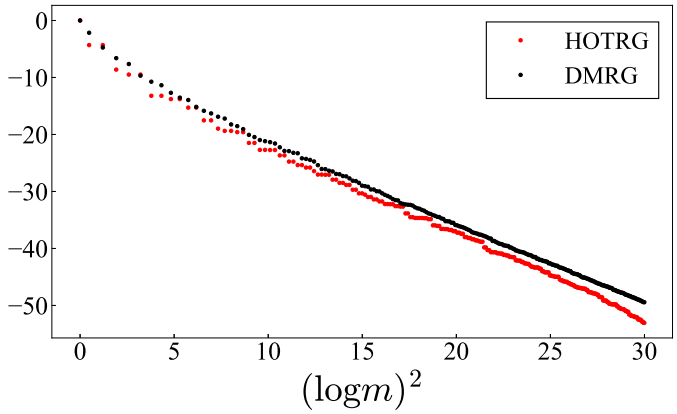

FIGURE 7.5: Eigenvalue distribution for $(\log m)^2$ of 2D MDM with monomer activity $z = 0.01$. The value of the vertical axis is $\log(\Omega_m(z^2))^4$ for HOTRG and $\log(\lambda_m(z))$ for DMRG. The number of retained basis is $m_{\text{base}} = 240$ for DMRG and $D_{\text{bond}} = 240$ for HOTRG.

Chapter 8

Summary and Outlook

In this thesis, we investigated the critical behavior of the monomer-dimer model (MDM) on the various lattices by HOTRG and DMRG calculations. In two-dimensions, the critical behavior of MDM was determined by HOTRG and DMRG, and it was found that the universality class of MDM is different from that of the Ising model with a magnetic field. In three dimensions, two major analyses were performed. One is a layer system with a finite number of layers, and the other is a cubic lattice, which is an infinite three-dimensional system. In MDM on the layer lattice, we showed that there is the critical behavior that is specific to the layer system. In analysis for MDM in the cubic lattice, first of all, we constructed the parallel computation-like algorithm of HOTRG to reduce the memory cost. Using our HOTRG algorithm, we calculated the residual entropy with higher accuracy than previous studies and analyzed the critical behavior. Thanks to the ability to perform HOTRG calculations with a large number of retained bases, we were able to analyze the asymptotic behavior of the HOTRG spectrum and derive relations that hold for integrable models.

In Chapter 3, we reduced a memory cost of HOTRG by focusing on the order of tensor contraction and the storage of each component of the tensor. The components of the tensor that are not contracted need to be stored in the computer's memory. Therefore, it is necessary to pay attention to the components that require memory storage not only before and after the contraction process, but also during the contraction process. First, by devising the order in which contractions are taken, we reduce the number of components that are not contracted during the contraction process. Next, by storing components in directions not related to the contraction operation in a separate memory, it is possible to handle tensors with the number of components exceeding the memory limit of one node.

In Chapter 4, we proposed a conjecture that the critical behavior of monomer density is $\rho(z) \sim z^{1+\frac{1}{\delta}}$. Using HOTRG and DMRG, we confirmed that this form is correct and determined that the critical exponent of the monomer density is $\delta = 7$ for bipartite 2D lattices such as square and honeycomb lattices. Our results showed that the value of δ is consistent with the Gaunt's expectation based on the asymptotic expansion[83]. On the other hand, 2D MDM is considered to be equivalent to the Ising model with a magnetic field by associating monomers with the magnetic field. However, since the critical exponent is $\delta = 7$ for 2D MDM and $\delta = 15$ for Ising model, we concluded that the universality classes of the 2D MDM and Ising model are different.

In Chapter 5, we studied MDM on the finite layer lattices for both the bipartite and non-bipartite constituent layer cases. Using DMRG, we analyzed two-layer triangular lattice as a non-bipartite lattice and two- and three- layer lattices of square and honeycomb geometry as bipartite lattices. From these analyses, it was found that the non-bipartite layer model is non-critical and the bipartite layer model varies in criticality with the number of layers. For the bipartite layer model, we showed

that the 2-layer model is non-critical and the 3-layer model is critical. This can be attributed to the fact that the two-layer PDM can be identified as a stacked system of two MDMs on a two-dimensional lattice, whereas the three-layer PDM has a three-dimensionality that allows the interlayer dimers to move in the z direction. In order to comprehensively understand systems with a large number of layers, we attempted to map MDM to a bosonic theory. According to this correspondence, the presence or absence of zero modes depends on the boundary conditions, and the confinement and criticality are determined accordingly. Only for two-layer systems, we studied the criticality of the PDM on the two-layer square lattice model when the interlayer dimer activity was varied. As a result, it was found that the model is non-critical at least in $x_v \geq 0.1$. On the other hand, in the region of $x_v \geq 0.6$, the model showed the same behavior as the two-layer model at $x_v = 1$, but in $x_v \leq 0.4$, a deviation from $\rho(z) \sim z^2$ appeared.

In Chapter 6, we analyzed the infinite 3D system by using the parallel computation algorithm of HOTRG introduced in Chap.3. We calculated the residual entropy of PDM on the cubic lattice and, obtained the behavior of convergence with respect to the increase in the number of reserved bases. The result was more accurate than the PEPS value of previous study. Furthermore, we analyzed the behavior of monomer density in the vicinity of critical point and tried to determine the critical exponent. However, the value of the exponent varied depending on the choice of the region that constituted the fitting function. At present, the accuracy of the HOTRG calculations performed in this paper was not sufficient to accurately determine the critical exponents.

In chapter 7, we analyzed the asymptotic behavior of the spectrum of HOTRG based on the CTM picture. Comparing the asymptotic behavior of spectrum of HOTRG and that of DMRG, we derived the relation that holds for the integrable models. We also numerically confirmed that the establishment of the relation by HOTRG and DMRG calculation with the large number of retained basis.

We mention about the future work and the outlook. In our studies about layer models and general 3D models, there are unfinished parts, so these issues are listed as future tasks. In Chapter 5, we showed that $\rho \sim z^2$ was valid in $x_v \geq$, but there was a deviation from $\rho \sim z^2$ in $x_v \leq 0.4$ in the range of the order of $z \sim 10^{-6}$. However, we conjecture that z^2-dependence is also valid for $x_v \leq 0.4$ very close to $z = 0$. So, we should analyze the region of the order less than $z \sim 10^{-6}$.

In Chapter 6, we could not determine the critical exponent of the cubic MDM, which is one of the infinite 3D model. Checking the distribution of the eigenvalues of the tensor degenerated by HOTRG, we can see that the number of bases D_{bond} retained may not be sufficient for accurate analysis. So, HOTRG calculation with high Dbond is required. On the other hand, the degeneracy of the eigenvalues also appears, which may reduce the accuracy of the HOTRG calculation. As the degeneracy appears even away from the vicinity of the critical point, this degeneracy may be specific to MDM. Therefore, it is necessary to specify the source of the degeneracy.

Finally, we propose the outlook.

- Understanding the finite temperature phase diagram of MDM
  MDM can be extended to include the interactions between dimers at finite temperature. In the case of the square lattice, PDM with interactions favoring dimer alignment exhibit the Berezinski-Kosterlitz-Thouless (BKT) transition[62, 93], and similar studies have been performed in two-layer[63] and three-dimensional systems[64–66]. Therefore, it would be interesting to study the phase diagram at finite temperature for general multilayer systems and investigate the characteristics depending on the number of layers.

- HOTRG calculations for various higher dimensional models
  It can be said that our parallel computation method of HOTRG has opened the door to the analysis of high dimensional models. Not only PDM and MDM, but also 3D classical models, 2D quantum models, and many other systems can be analyzed. In the future, it is necessary to understand the advantages and disadvantages of HOTRG and the limitations of its application through these analyses.

- New method of determining the criticality based on the spectrum distribution
  In this thesis, we showed that relation (7.31) is valid only for the integrable models. On the other hand, in the non-critical region where the CDL decoupling is established, (7.9) holds for both integrable and non-integrable models. Therefore, by analyzing whether or not (7.9) holds, we can determine the criticality of the model. Although this method requires a large amount of computation, it is expected to be more accurate in determining the criticality than the calculation of the correlation length by DMRG.

Appendix A

Numerical setup for various lattice models

A.1 Construction of the local tensors in HOTRG

This section describes the process of constructing the local tensor. Both honeycomb and triangular lattices are transformed into square lattices, which HOTRG can be applied to.

A.1.1 Honeycomb lattice

On the honeycomb lattice, the initial local tensor has three components:

$$T^{(h)}_{ijk} = \begin{cases} z & \text{if } i=j=k=0; \\ 1 & \text{if only one index is 1;} \\ 0 & \text{otherwise.} \end{cases} \tag{A.1}$$

By contracting adjacent local tensors, a honeycomb lattice is deformed into a square lattice as shown in Fig.A.1.

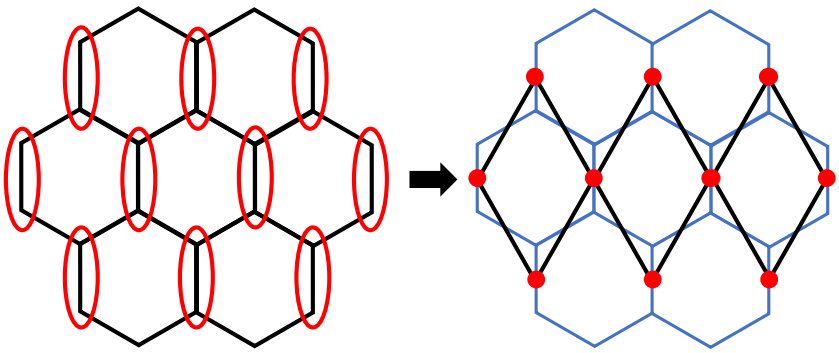

FIGURE A.1: Deformation of honeycomb lattice into square lattice.

A.1.2 Triangular lattice

On the honeycomb lattice, the initial local tensor has six components:

$$T^{(t)}_{ijklmn} = \begin{cases} z & \text{if } i=j=k=l=m=n=0; \\ 1 & \text{if only one index is 1;} \\ 0 & \text{otherwise.} \end{cases} \tag{A.2}$$

The triangular lattice can be deform into a honeycomb lattice[94]. At first, we decompose the initial local tensor into four tensors by SVD as shown in Fig.A.2(a):

$$T^{(t)}_{ijklmn} = \sum_{X,Y,Z} (T_a)_{XYZ}(S_a)_{ijX}(S_b)_{klY}(S_a)_{mnZ}. \tag{A.3}$$

Next, by crushing the triangle emerging through SVD into one point (Fig.A.2(c)), the triangular lattice is deformed into the honeycomb lattice (Fig.A.2(b)):

$$(T_b)_{XYZ} = \sum_{a,b,c} (S_a)_{caX}(S_b)_{abY}(S_a)_{bcZ} \tag{A.4}$$

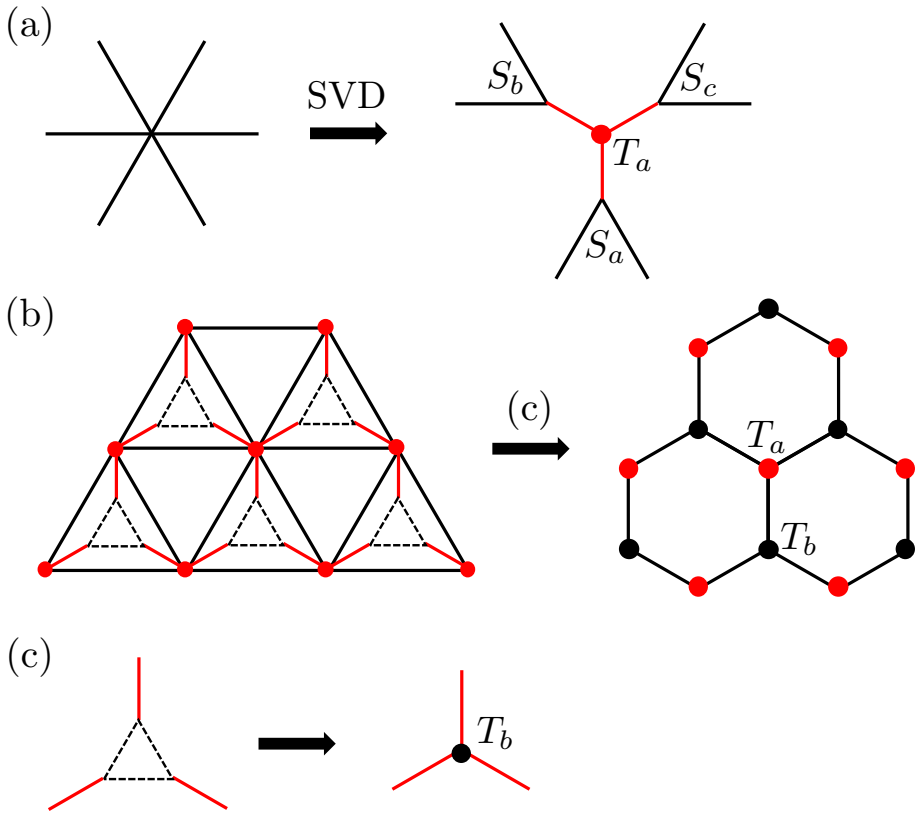

FIGURE A.2: Deformation of honeycomb lattice into square lattice.

Finally, contracting T_a and T_b as well as the honeycomb lattice case in Sec.A.1.1, the honeycomb lattice is deformed into the square lattice. Note that the number of components of the final local tensor in the deformed square lattice is 4 in the honeycomb lattice and 8 in the triangular lattice, and the effective number of retained bases is smaller than in the square lattice.

A.2 Calculation algorithm for the triangular lattice in DMRG

We show a procedure of DMRG calculation for the triangular lattice. First, we recognize the triangular lattice as the square lattice with a diagonal line as shown in Fig.A.3. Under this setup, we recognize a local tensor which has six components as a block shown in Fig.A.4.

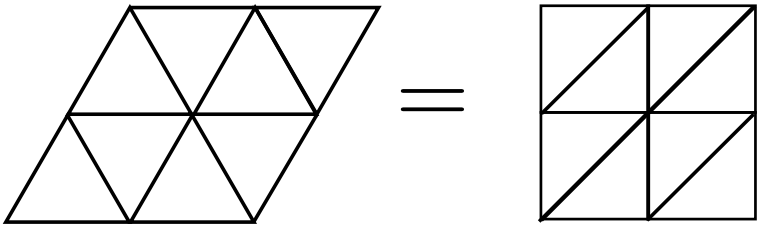

FIGURE A.3: Recognition the triangular lattice as the square lattice with a diagonal line.

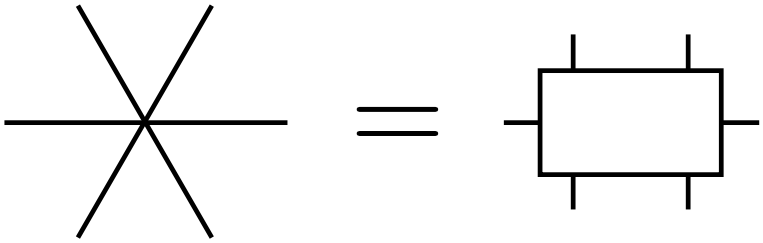

FIGURE A.4: Block of components.

From the construction of a constituent block, we need to operate two types of transfer matrices alternately (Fig.A.5).

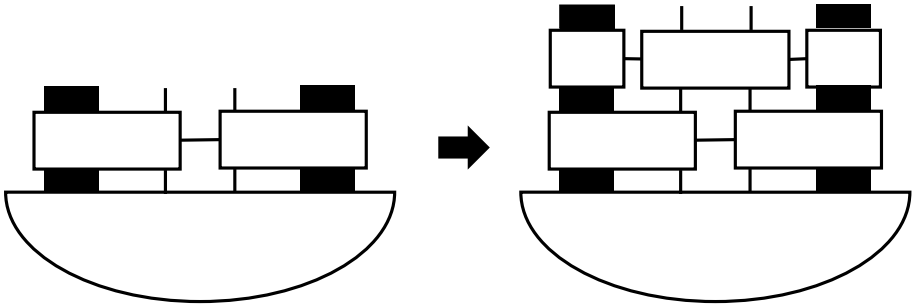

FIGURE A.5: Operation of block of components to a state.

Appendix B

Additional length scale that appears in calculations with finite bond dimensions

The accuracy of numerical results extracted from DMRG is affected by the finite bond dimension m. In Ref.[81], it is shown that a finite bond dimension introduces another length scale "*effective correlation length*". Comparing the effective correlation length and the characteristic length scale of a finite system, we can discuss the validity of the approximation. Furthermore, from the crossover that emerges from the combination of the two scales, we can also obtain information on the critical exponents. This two scaling problem has been developed in modern times, for example in quantum mechanics[95] and field theories[96]. In this chapter, we review the two scale problem according to Ref.[81].

In this chapter, we consider the corner transfer matrix renormalization group (CTMRG)[97]. CTMRG is a development of the DMRG based on CTM introduced in Eq.(7.3) and the approximation error is characterized by the eigenvalues of CTM.

The first length scale is the characteristic length of the finite size system ξ_N, which is defined as

$$\xi_N^{-1} = \log \frac{\Lambda_0(N,\infty)}{\Lambda_1(N,\infty)}, \tag{B.1}$$

where $\Lambda_0(N,m)$ and $\Lambda_1(N,m)$ are the largest and second-largest eigenvalue of CTM with system size N and bond dimension m, respectively. Finite bond dimension induces an additional length scale (effective length scale) $\xi(m)$:

$$\xi^{-1}(m) = \log \frac{\Lambda_0(\infty,m)}{\Lambda_1(\infty,m)}. \tag{B.2}$$

These two length scale determine the accuracy of the calculation. If $\xi_N \ll \xi(m)$, the calculation is good approximation. However, if $\xi_N \gg \xi(m)$, the approximated partition function will be much smaller than the exact value. The relationship between the size of these two length scales causes a crossover, and the critical exponent can be accessed from the discussion of the scaling.

Bibliography

[1] Hidetoshi Nishimori and Gerardo Ortiz. "Elements of Phase Transitions and Critical Phenomena". In: *Oxford University Press* (2011).

[2] Lars Onsager. "Crystal Statistics. I. A Two-Dimensional Model with an Order-Disorder Transition". In: *Phys. Rev.* 65 (3-4 1944), pp. 117–149. DOI: 10.1103/PhysRev.65.117. URL: https://link.aps.org/doi/10.1103/PhysRev.65.117.

[3] John Keith Roberts. "Composite films of oxygen and hydrogen on tungsten". In: *Proceedings of the Royal Society A: Mathematical, Physical and Engineering Sciences* 152.876 (1935), pp. 477–480. DOI: 10.1098/rspa.1935.0202. URL: https://royalsocietypublishing.org/doi/abs/10.1098/rspa.1935.0202.

[4] John Keith Roberts. "The kinetics of adsorption with interaction between the adsorbed particles". In: *Proceedings of the Royal Society A: Mathematical, Physical and Engineering Sciences* 161.876 (1937), pp. 141–153. DOI: https://doi.org/10.1098/rspa.1937.0138.

[5] J. K. Roberts. "The theory of adsorption when each particle occupies more than one site". In: *Mathematical Proceedings of the Cambridge Philosophical Society* 34.4 (1938), 577–586. DOI: 10.1017/S0305004100020594.

[6] J. K. Roberts and A. R. Miller. "The application of statistical methods to immobile adsorbed films". In: *Mathematical Proceedings of the Cambridge Philosophical Society* 35.2 (1939), 293–297. DOI: 10.1017/S0305004100020971.

[7] P. W. Kasteleyn. "The statistics of dimers on a lattice: I. The number of dimer arrangements on a quadratic lattice". In: *Physica* 27.12 (1961), pp. 1209–1225. ISSN: 0031-8914. DOI: https://doi.org/10.1016/0031-8914(61)90063-5. URL: https://www.sciencedirect.com/science/article/pii/0031891461900635.

[8] H. N. V. Temperley and Michael E. Fisher. "Dimer problem in statistical mechanics-an exact result". In: *The Philosophical Magazine: A Journal of Theoretical Experimental and Applied Physics* 6.68 (1961), pp. 1061–1063. DOI: 10.1080/14786436108243366. eprint: https://doi.org/10.1080/14786436108243366. URL: https://doi.org/10.1080/14786436108243366.

[9] Michael E. Fisher. "Statistical Mechanics of Dimers on a Plane Lattice". In: *Phys. Rev.* 124 (6 1961), pp. 1664–1672. DOI: 10.1103/PhysRev.124.1664. URL: https://link.aps.org/doi/10.1103/PhysRev.124.1664.

[10] R. H. Fowler and G. S. Rushbrooke. "An attempt to extend the statistical theory of perfect solutions". In: *Trans. Faraday Soc.* 33 (0 1937), pp. 1272–1294. DOI: 10.1039/TF9373301272. URL: http://dx.doi.org/10.1039/TF9373301272.

[11] F.Y. Tzeng W.-J. Wu. "Dimers on a Simple-Quartic Net with a Vacancy". In: *J. Stat. Phys.* 110 (2003), pp. 671–689.

[12] F. Y. Wu. "Pfaffian solution of a dimer-monomer problem: Single monomer on the boundary". In: *Phys. Rev. E* 74 (2 2006), p. 020104. DOI: 10.1103/PhysRevE.74.020104. URL: https://link.aps.org/doi/10.1103/PhysRevE.74.020104.

[13] T. S. Chang. "Statistical theory of the adsorption of double molecules". In: *Proceedings of the Royal Society A: Mathematical, Physical and Engineering Sciences* 169 (1939), p. 512. DOI: https://doi.org/10.1098/rspa.1939.0014.

[14] A. R. Miller. "The number of configurations of a cooperative assembly". In: *Mathematical Proceedings of the Cambridge Philosophical Society* 38.1 (1942), 109–124. DOI: 10.1017/S030500410002226X.

[15] W. J. C. Orr. "On the calculation of certain higher-order Bethe approximations". In: *Trans. Faraday Soc.* 40 (0 1944), pp. 306–320. DOI: 10.1039/TF9444000306. URL: http://dx.doi.org/10.1039/TF9444000306.

[16] M. L. McGlashan. "Entropies of mixing in athermal mixtures of molecules of single and double size". In: *Trans. Faraday Soc.* 47 (0 1951), pp. 1042–1049. DOI: 10.1039/TF9514701042. URL: http://dx.doi.org/10.1039/TF9514701042.

[17] R. J. Baxter. "Dimers on a Rectangular Lattice". In: *Journal of Mathematical Physics* 9.4 (1968), pp. 650–654. DOI: 10.1063/1.1664623. URL: https://doi.org/10.1063/1.1664623.

[18] C M Care and D J Cleaver. "Computer simulation of liquid crystals". In: *Reports on Progress in Physics* 68.11 (2005), pp. 2665–2700. DOI: 10.1088/0034-4885/68/11/r04. URL: https://doi.org/10.1088/0034-4885/68/11/r04.

[19] Lars Onsager. "The Effects of Shape on the Interaction of Colloidal Particles". In: *Ann. N.Y. Acad. Sci.* 51 (4 1949), pp. 627–659. DOI: 10.1111/j.1749-6632.1949.tb27296. URL: https://doi.org/10.1111/j.1749-6632.1949.tb27296.x.

[20] Ghosh, A. and Dhar, D. "On the orientational ordering of long rods on a lattice". In: *EPL* 78.2 (2007), p. 20003. DOI: 10.1209/0295-5075/78/20003. URL: https://doi.org/10.1209/0295-5075/78/20003.

[21] P. M. Pasinetti et al. "Entropy-driven phases at high coverage adsorption of straight rigid rods on two-dimensional square lattices". In: *Phys. Rev. E* 104 (5 2021), p. 054136. DOI: 10.1103/PhysRevE.104.054136. URL: https://link.aps.org/doi/10.1103/PhysRevE.104.054136.

[22] Stefanos Papanikolaou, Daniel Charrier, and Eduardo Fradkin. "Ising nematic fluid phase of hard-core dimers on the square lattice". In: *Phys. Rev. B* 89 (3 2014), p. 035128. DOI: 10.1103/PhysRevB.89.035128. URL: https://link.aps.org/doi/10.1103/PhysRevB.89.035128.

[23] H.T.Diep et al. "Frustrated spin systems". In: *World scientific* (2013).

[24] P. W. Kasteleyn. "Dimer Statistics and Phase Transitions". In: *Journal of Mathematical Physics* 4.2 (1963), pp. 287–293. DOI: 10.1063/1.1703953. URL: https://doi.org/10.1063/1.1703953.

[25] Michael E. Fisher and John Stephenson. "Statistical Mechanics of Dimers on a Plane Lattice. II. Dimer Correlations and Monomers". In: *Phys. Rev.* 132 (4 1963), pp. 1411–1431. DOI: 10.1103/PhysRev.132.1411. URL: https://link.aps.org/doi/10.1103/PhysRev.132.1411.

[26] Michael E. Fisher. "On the Dimer Solution of Planar Ising Models". In: *Journal of Mathematical Physics* 7.10 (1966), pp. 1776–1781. DOI: 10.1063/1.1704825. URL: https://doi.org/10.1063/1.1704825.

[27] P. Fendley, R. Moessner, and S. L. Sondhi. "Classical dimers on the triangular lattice". In: *Phys. Rev. B* 66 (21 2002), p. 214513. DOI: 10.1103/PhysRevB.66.214513. URL: https://link.aps.org/doi/10.1103/PhysRevB.66.214513.

[28] Werner Krauth and R. Moessner. "Pocket Monte Carlo algorithm for classical doped dimer models". In: *Phys. Rev. B* 67 (6 2003), p. 064503. DOI: 10.1103/PhysRevB.67.064503. URL: https://link.aps.org/doi/10.1103/PhysRevB.67.064503.

[29] Y. L. Loh, Dao-Xin Yao, and E. W. Carlson. "Dimers on the triangular kagome lattice". In: *Phys. Rev. B* 78 (22 2008), p. 224410. DOI: 10.1103/PhysRevB.78.224410. URL: https://link.aps.org/doi/10.1103/PhysRevB.78.224410.

[30] Chungpeng Fan and F. Y. Wu. "General Lattice Model of Phase Transitions". In: *Phys. Rev. B* 2 (3 1970), pp. 723–733. DOI: 10.1103/PhysRevB.2.723. URL: https://link.aps.org/doi/10.1103/PhysRevB.2.723.

[31] Ole J. Heilmann and Elliott H. Lieb. "Theory of monomer-dimer systems". In: *Communications in Mathematical Physics* 25.3 (1972), pp. 190 –232. DOI: cmp/1103857921. URL: https://doi.org/.

[32] Jorgen Rasmussen and Philippe Ruelle. "Refined conformal spectra in the dimer model". In: *Journal of Statistical Mechanics: Theory and Experiment* 2012.10 (2012), P10002. DOI: 10.1088/1742-5468/2012/10/p10002. URL: https://doi.org/10.1088/1742-5468/2012/10/p10002.

[33] Arthur E. Ferdinand. "Statistical Mechanics of Dimers on a Quadratic Lattice". In: *Journal of Mathematical Physics* 8.12 (1967), pp. 2332–2339. DOI: 10.1063/1.1705162. URL: https://doi.org/10.1063/1.1705162.

[34] N. Sh. Izmailian, K. B. Oganesyan, and Chin-Kun Hu. "Exact finite-size corrections of the free energy for the square lattice dimer model under different boundary conditions". In: *Phys. Rev. E* 67 (6 2003), p. 066114. DOI: 10.1103/PhysRevE.67.066114. URL: https://link.aps.org/doi/10.1103/PhysRevE.67.066114.

[35] N. Sh. Izmailian et al. "Logarithmic Conformal Field Theory and Boundary Effects in the Dimer Model". In: *Phys. Rev. Lett.* 95 (26 2005), p. 260602. DOI: 10.1103/PhysRevLett.95.260602. URL: https://link.aps.org/doi/10.1103/PhysRevLett.95.260602.

[36] N. Sh. Izmailian et al. "Finite-size corrections and scaling for the triangular lattice dimer model with periodic boundary conditions". In: *Phys. Rev. E* 73 (1 2006), p. 016128. DOI: 10.1103/PhysRevE.73.016128. URL: https://link.aps.org/doi/10.1103/PhysRevE.73.016128.

[37] Nickolay Izmailian et al. "Exact finite-size corrections and corner free energies for the $c = -2$ universality class". In: *Nuclear Physics B* 884 (2014), pp. 157–171. ISSN: 0550-3213. DOI: https://doi.org/10.1016/j.nuclphysb.2014.04.023. URL: https://www.sciencedirect.com/science/article/pii/S0550321314001394.

[38] Yong Kong. "Logarithmic corrections in the free energy of monomer-dimer model on plane lattices with free boundaries". In: *Phys. Rev. E* 74 (1 2006), p. 011102. DOI: 10.1103/PhysRevE.74.011102. URL: https://link.aps.org/doi/10.1103/PhysRevE.74.011102.

[39] Yong Kong. "Monomer-dimer model in two-dimensional rectangular lattices with fixed dimer density". In: *Phys. Rev. E* 74 (6 2006), p. 061102. DOI: 10.1103/PhysRevE.74.061102. URL: https://link.aps.org/doi/10.1103/PhysRevE.74.061102.

[40] Stéphane Mahieu and Philippe Ruelle. "Scaling fields in the two-dimensional Abelian sandpile model". In: *Phys. Rev. E* 64 (6 2001), p. 066130. DOI: 10.1103/PhysRevE.64.066130. URL: https://link.aps.org/doi/10.1103/PhysRevE.64.066130.

[41] Philippe Ruelle. "A c=2 boundary changing operator for the Abelian sandpile model". In: *Physics Letters B* 539.1 (2002), pp. 172–177. ISSN: 0370-2693. DOI: https://doi.org/10.1016/S0370-2693(02)02069-5. URL: https://www.sciencedirect.com/science/article/pii/S0370269302020695.

[42] Monwhea Jeng, Geoffroy Piroux, and Philippe Ruelle. "Height variables in the Abelian sandpile model: scaling fields and correlations". In: *Journal of Statistical Mechanics: Theory and Experiment* 2006.10 (2006), P10015–P10015. DOI: 10.1088/1742-5468/2006/10/p10015. URL: https://doi.org/10.1088/1742-5468/2006/10/p10015.

[43] Philippe Ruelle. "Wind on the boundary for the Abelian sandpile model". In: *Journal of Statistical Mechanics: Theory and Experiment* 2007.09 (2007), P09013–P09013. DOI: 10.1088/1742-5468/2007/09/p09013. URL: https://doi.org/10.1088/1742-5468/2007/09/p09013.

[44] V S Poghosyan et al. "Logarithmic two-point correlators in the Abelian sandpile model". In: *Journal of Statistical Mechanics: Theory and Experiment* 2010.07 (2010), P07025. DOI: 10.1088/1742-5468/2010/07/p07025. URL: https://doi.org/10.1088/1742-5468/2010/07/p07025.

[45] Vyatcheslav B. Priezzhev and Philippe Ruelle. "Boundary monomers in the dimer model". In: *Phys. Rev. E* 77 (6 2008), p. 061126. DOI: 10.1103/PhysRevE.77.061126. URL: https://link.aps.org/doi/10.1103/PhysRevE.77.061126.

[46] Richard Kenyon. "Dominos and the Gaussian Free Field". In: *The Annals of Probability* 29.3 (2001), pp. 1128 –1137. DOI: 10.1214/aop/1015345599. URL: https://doi.org/10.1214/aop/1015345599.

[47] Steven R. White. "Density matrix formulation for quantum renormalization groups". In: *Phys. Rev. Lett.* 69 (19 1992), pp. 2863–2866. DOI: 10.1103/PhysRevLett.69.2863. URL: https://link.aps.org/doi/10.1103/PhysRevLett.69.2863.

[48] Steven R. White. "Density-matrix algorithms for quantum renormalization groups". In: *Phys. Rev. B* 48 (14 1993), pp. 10345–10356. DOI: 10.1103/PhysRevB.48.10345. URL: https://link.aps.org/doi/10.1103/PhysRevB.48.10345.

[49] Stellan Östlund and Stefan Rommer. "Thermodynamic Limit of Density Matrix Renormalization". In: *Phys. Rev. Lett.* 75 (19 1995), pp. 3537–3540. DOI: 10.1103/PhysRevLett.75.3537. URL: https://link.aps.org/doi/10.1103/PhysRevLett.75.3537.

[50] Yasuhiro Hieida, Kouichi Okunishi, and Yasuhiro Akutsu. "Numerical renormalization approach to two-dimensional quantum antiferromagnets with valence-bond-solid type ground state". In: *New Journal of Physics* 1 (1999). DOI: 10.1088/1367-2630/1/1/007. URL: https://doi.org/10.1088/1367-2630/1/1/007.

[51] Tomotoshi Nishino et al. "Two-Dimensional Tensor Product Variational Formulation". In: *Progress of Theoretical Physics* 105.3 (Mar. 2001), pp. 409–417. ISSN: 0033-068X. DOI: 10.1143/PTP.105.409. URL: https://doi.org/10.1143/PTP.105.409.

[52] Andrej Gendiar, Nobuya Maeshima, and Tomotoshi Nishino. "Stable Optimization of a Tensor Product Variational State". In: *Progress of Theoretical Physics* 110.4 (Oct. 2003), pp. 691–699. ISSN: 0033-068X. DOI: 10.1143/PTP.110.691. URL: https://doi.org/10.1143/PTP.110.691.

[53] F. Verstraete and J. Cirac. "Renormalization algorithms for Quantum-Many Body Systems in two and higher dimensions : arXiv:cond-mat/0407066". In: (2004).

[54] G. Vidal. "Entanglement Renormalization". In: *Phys. Rev. Lett.* 99 (22 2007), p. 220405. DOI: 10.1103/PhysRevLett.99.220405. URL: https://link.aps.org/doi/10.1103/PhysRevLett.99.220405.

[55] G. Vidal. "Class of Quantum Many-Body States That Can Be Efficiently Simulated". In: *Phys. Rev. Lett.* 101 (11 2008), p. 110501. DOI: 10.1103/PhysRevLett.101.110501. URL: https://link.aps.org/doi/10.1103/PhysRevLett.101.110501.

[56] Michael Levin and Cody P. Nave. "Tensor Renormalization Group Approach to Two-Dimensional Classical Lattice Models". In: *Phys. Rev. Lett.* 99 (12 2007), p. 120601. DOI: 10.1103/PhysRevLett.99.120601. URL: https://link.aps.org/doi/10.1103/PhysRevLett.99.120601.

[57] Z. Y. Xie et al. "Coarse-graining renormalization by higher-order singular value decomposition". In: *Phys. Rev. B* 86 (4 2012), p. 045139. DOI: 10.1103/PhysRevB.86.045139. URL: https://link.aps.org/doi/10.1103/PhysRevB.86.045139.

[58] Yusuke Yoshimura et al. "Calculation of fermionic Green functions with Grassmann higher-order tensor renormalization group". In: *Phys. Rev. D* 97 (5 2018), p. 054511. DOI: 10.1103/PhysRevD.97.054511. URL: https://link.aps.org/doi/10.1103/PhysRevD.97.054511.

[59] Shinichiro Akiyama et al. "Phase transition of four-dimensional Ising model with higher-order tensor renormalization group". In: *Phys. Rev. D* 100 (5 2019), p. 054510. DOI: 10.1103/PhysRevD.100.054510. URL: https://link.aps.org/doi/10.1103/PhysRevD.100.054510.

[60] Shun Wang et al. "Phase Transitions of Ferromagnetic Potts Models on the Simple Cubic Lattice". In: *Chinese Physics Letters* 31.7 (2014), p. 070503. DOI: 10.1088/0256-307x/31/7/070503. URL: https://doi.org/10.1088/0256-307x/31/7/070503.

[61] David A. Huse et al. "Coulomb and Liquid Dimer Models in Three Dimensions". In: *Phys. Rev. Lett.* 91 (16 2003), p. 167004. DOI: 10.1103/PhysRevLett.91.167004. URL: https://link.aps.org/doi/10.1103/PhysRevLett.91.167004.

[62] Fabien Alet et al. "Interacting Classical Dimers on the Square Lattice". In: *Phys. Rev. Lett.* 94 (23 2005), p. 235702. DOI: 10.1103/PhysRevLett.94.235702. URL: https://link.aps.org/doi/10.1103/PhysRevLett.94.235702.

[63] Nisheeta Desai, Sumiran Pujari, and Kedar Damle. "Bilayer Coulomb phase of two-dimensional dimer models: Absence of power-law columnar order". In: *Phys. Rev. E* 103 (4 2021), p. 042136. DOI: 10.1103/PhysRevE.103.042136. URL: https://link.aps.org/doi/10.1103/PhysRevE.103.042136.

[64] Grégoire Misguich, Vincent Pasquier, and Fabien Alet. "Correlations and order parameter at a Coulomb-crystal phase transition in a three-dimensional dimer model". In: *Phys. Rev. B* 78 (10 2008), p. 100402. DOI: 10.1103/PhysRevB.78.100402. URL: https://link.aps.org/doi/10.1103/PhysRevB.78.100402.

[65] Stefanos Papanikolaou and Joseph J. Betouras. "First-Order versus Unconventional Phase Transitions in Three-Dimensional Dimer Models". In: *Phys. Rev. Lett.* 104 (4 2010), p. 045701. DOI: 10.1103/PhysRevLett.104.045701. URL: https://link.aps.org/doi/10.1103/PhysRevLett.104.045701.

[66] G. J. Sreejith and Stephen Powell. "Critical behavior in the cubic dimer model at nonzero monomer density". In: *Phys. Rev. B* 89 (1 2014), p. 014404. DOI: 10.1103/PhysRevB.89.014404. URL: https://link.aps.org/doi/10.1103/PhysRevB.89.014404.

[67] Hiroshi Ueda, Kouichi Okunishi, and Tomotoshi Nishino. "Doubling of entanglement spectrum in tensor renormalization group". In: *Phys. Rev. B* 89 (7 2014), p. 075116. DOI: 10.1103/PhysRevB.89.075116. URL: https://link.aps.org/doi/10.1103/PhysRevB.89.075116.

[68] F. Y. Wu. "Remarks on the Modified Potassium Dihydrogen Phosphate Model of a Ferroelectric". In: *Phys. Rev.* 168 (2 1968), pp. 539–543. DOI: 10.1103/PhysRev.168.539. URL: https://link.aps.org/doi/10.1103/PhysRev.168.539.

[69] P. Fendley, R. Moessner, and S. L. Sondhi. "Classical dimers on the triangular lattice". In: *Phys. Rev. B* 66 (21 2002), p. 214513. DOI: 10.1103/PhysRevB.66.214513. URL: https://link.aps.org/doi/10.1103/PhysRevB.66.214513.

[70] Fa Wang and F. Y. Wu. "Exact solution of close-packed dimers on the kagomé lattice". In: *Phys. Rev. E* 75 (4 2007), p. 040105. DOI: 10.1103/PhysRevE.75.040105. URL: https://link.aps.org/doi/10.1103/PhysRevE.75.040105.

[71] Robert E. Hartwig. "Monomer Pair Correlations". In: *Journal of Mathematical Physics* 7.2 (1966), pp. 286–299. DOI: 10.1063/1.1704931. URL: https://doi.org/10.1063/1.1704931.

[72] C. L. Henley. "Relaxation time for a dimer covering with height representation". In: *J. Stat. Phys.* 89 (3 1997), pp. 483–507. DOI: 10.1007/BF02765532. URL: https://doi.org/10.1007/BF02765532.

[73] Neil Wilkins and Stephen Powell. "Interacting double dimer model on the square lattice". In: *Phys. Rev. B* 102 (17 2020), p. 174431. DOI: 10.1103/PhysRevB.102.174431. URL: https://link.aps.org/doi/10.1103/PhysRevB.102.174431.

[74] R. Youngblood, J. D. Axe, and B. M. McCoy. "Correlations in ice-rule ferroelectrics". In: *Phys. Rev. B* 21 (11 1980), pp. 5212–5220. DOI: 10.1103/PhysRevB.21.5212. URL: https://link.aps.org/doi/10.1103/PhysRevB.21.5212.

[75] Fabien Alet et al. "Classical dimers with aligning interactions on the square lattice". In: *Phys. Rev. E* 74 (4 2006), p. 041124. DOI: 10.1103/PhysRevE.74.041124. URL: https://link.aps.org/doi/10.1103/PhysRevE.74.041124.

[76] A. C. Maggs and V. Rossetto. "Local Simulation Algorithms for Coulomb Interactions". In: *Phys. Rev. Lett.* 88 (19 2002), p. 196402. DOI: 10.1103/PhysRevLett.88.196402. URL: https://link.aps.org/doi/10.1103/PhysRevLett.88.196402.

[77] Lieven De Lathauwer, Bart De Moor, and Joos Vandewalle. "A Multilinear Singular Value Decomposition". In: *SIAM Journal on Matrix Analysis and Applications* 21.4 (2000), pp. 1253–1278. DOI: 10.1137/S0895479896305696. eprint: https://doi.org/10.1137/S0895479896305696. URL: https://doi.org/10.1137/S0895479896305696.

[78] Z. Y. Xie et al. "Second Renormalization of Tensor-Network States". In: *Phys. Rev. Lett.* 103 (16 2009), p. 160601. DOI: 10.1103/PhysRevLett.103.160601. URL: https://link.aps.org/doi/10.1103/PhysRevLett.103.160601.

[79] Hui-Hai Zhao et al. "Tensor network algorithm by coarse-graining tensor renormalization on finite periodic lattices". In: *Phys. Rev. B* 93 (12 2016), p. 125115. DOI: 10.1103/PhysRevB.93.125115. URL: https://link.aps.org/doi/10.1103/PhysRevB.93.125115.

[80] Tomotoshi Nishino. "Density Matrix Renormalization Group Method for 2D Classical Models". In: *Journal of the Physical Society of Japan* 64.10 (1995), pp. 3598–3601. DOI: 10.1143/JPSJ.64.3598. URL: https://doi.org/10.1143/JPSJ.64.3598.

[81] T. Nishino, K. Okunishi, and M. Kikuchi. "Numerical renormalization group at criticality". In: *Physics Letters A* 213.1 (1996), pp. 69–72. ISSN: 0375-9601. DOI: https://doi.org/10.1016/0375-9601(96)00128-4. URL: https://www.sciencedirect.com/science/article/pii/0375960196001284.

[82] Nicolas Allegra. "Exact solution of the 2d dimer model: Corner free energy, correlation functions and combinatorics". In: *Nuclear Physics B* 894 (2015), pp. 685–732. ISSN: 0550-3213. DOI: https://doi.org/10.1016/j.nuclphysb.2015.03.022. URL: https://www.sciencedirect.com/science/article/pii/S0550321315001042.

[83] David S. Gaunt. "Exact Series-Expansion Study of the Monomer-Dimer Problem". In: *Phys. Rev.* 179 (1 1969), pp. 174–186. DOI: 10.1103/PhysRev.179.174. URL: https://link.aps.org/doi/10.1103/PhysRev.179.174.

[84] John F. Nagle. "New Series-Expansion Method for the Dimer Problem". In: *Phys. Rev.* 152 (1 1966), pp. 190–197. DOI: 10.1103/PhysRev.152.190. URL: https://link.aps.org/doi/10.1103/PhysRev.152.190.

[85] Z B Li et al. "Critical exponents of the two-layer Ising model". In: *Journal of Physics A: Mathematical and General* 34.31 (2001), pp. 6069–6079. DOI: 10.1088/0305-4470/34/31/302. URL: https://doi.org/10.1088/0305-4470/34/31/302.

[86] Laurens Vanderstraeten, Bram Vanhecke, and Frank Verstraete. "Residual entropies for three-dimensional frustrated spin systems with tensor networks". In: *Phys. Rev. E* 98 (4 2018), p. 042145. DOI: 10.1103/PhysRevE.98.042145. URL: https://link.aps.org/doi/10.1103/PhysRevE.98.042145.

[87] Zheng-Cheng Gu and Xiao-Gang Wen. "Tensor-entanglement-filtering renormalization approach and symmetry-protected topological order". In: *Phys. Rev. B* 80 (15 2009), p. 155131. DOI: 10.1103/PhysRevB.80.155131. URL: https://link.aps.org/doi/10.1103/PhysRevB.80.155131.

[88] Kouichi Okunishi, Tomotoshi Nishino, and Hiroshi Ueda. "Developments in the Tensor Network – from Statistical Mechanics to Quantum Entanglement: arXiv:cond-mat/2111.12223". In: (2021).

[89] R. J. Baxter. "Exactly Solved Models in Statistical Mechanics". In: *Academic Press, London* (1982).

[90] Kouichi Okunishi, Yasuhiro Hieida, and Yasuhiro Akutsu. "Universal asymptotic eigenvalue distribution of density matrices and corner transfer matrices in the thermodynamic limit". In: *Phys. Rev. E* 59 (6 1999), R6227–R6230. DOI: 10.1103/PhysRevE.59.R6227. URL: https://link.aps.org/doi/10.1103/PhysRevE.59.R6227.

[91] G. E. Andrew. "The Theory of Partitions". In: *Cambridge University Press* (1984).

[92] Tomotoshi Nishino and Kouichi Okunishi. "Corner Transfer Matrix Algorithm for Classical Renormalization Group". In: *Journal of the Physical Society of Japan* 66.10 (1997), pp. 3040–3047. DOI: 10.1143/JPSJ.66.3040. URL: https://doi.org/10.1143/JPSJ.66.3040.

[93] Fabien Alet et al. "Classical dimers with aligning interactions on the square lattice". In: *Phys. Rev. E* 74 (4 2006), p. 041124. DOI: 10.1103/PhysRevE.74.041124. URL: https://link.aps.org/doi/10.1103/PhysRevE.74.041124.

[94] Krishanu Roychowdhury and Ching-Yu Huang. "Tensor renormalization group approach to classical dimer models". In: *Phys. Rev. B* 91 (20 2015), p. 205418. DOI: 10.1103/PhysRevB.91.205418. URL: https://link.aps.org/doi/10.1103/PhysRevB.91.205418.

[95] L. Tagliacozzo et al. "Scaling of entanglement support for matrix product states". In: *Phys. Rev. B* 78 (2 2008), p. 024410. DOI: 10.1103/PhysRevB.78.024410. URL: https://link.aps.org/doi/10.1103/PhysRevB.78.024410.

[96] Bram Vanhecke et al. "Scaling Hypothesis for Matrix Product States". In: *Phys. Rev. Lett.* 123 (25 2019), p. 250604. DOI: 10.1103/PhysRevLett.123.250604. URL: https://link.aps.org/doi/10.1103/PhysRevLett.123.250604.

[97] Tomotoshi Nishino and Kouichi Okunishi. "Corner Transfer Matrix Renormalization Group Method". In: *Journal of the Physical Society of Japan* 65.4 (1996), pp. 891–894. DOI: 10.1143/JPSJ.65.891. eprint: https://doi.org/10.1143/JPSJ.65.891. URL: https://doi.org/10.1143/JPSJ.65.891.